

2018-01-01

Electrocatalysts Based On Organic Macrocycles For Electrochemical Water Splitting

Yanyu Wu

University of Texas at El Paso, ywu4@miners.utep.edu

Follow this and additional works at: https://digitalcommons.utep.edu/open_etd



Part of the [Chemistry Commons](#)

Recommended Citation

Wu, Yanyu, "Electrocatalysts Based On Organic Macrocycles For Electrochemical Water Splitting" (2018). *Open Access Theses & Dissertations*. 21.

https://digitalcommons.utep.edu/open_etd/21

This is brought to you for free and open access by DigitalCommons@UTEP. It has been accepted for inclusion in Open Access Theses & Dissertations by an authorized administrator of DigitalCommons@UTEP. For more information, please contact lweber@utep.edu.

ELECTROCATALYSTS BASED ON ORGANIC MACROCYCLES FOR
ELECTROCHEMICAL WATER SPLITTING

YANYU WU

Doctoral Program in Chemistry

APPROVED:

Dino Villagrán, Ph.D., Chair

Keith Pannell, Ph.D.

Skye Fortier, Ph.D.

Yirong Lin, Ph.D.

Charles Ambler, Ph.D.
Dean of the Graduate School

Copyright ©

by

Yanyu Wu

2018

Dedication

To my family

ELECTROCATALYSTS BASED ON ORGANIC MACROCYCLES FOR
ELECTROCHEMICAL WATER SPLITTING

by

YANYU WU, B.S.

DISSERTATION

Presented to the Faculty of the Graduate School of

The University of Texas at El Paso

in Partial Fulfillment

of the Requirements

for the Degree of

DOCTOR OF PHILOSOPHY

Department of Chemistry and Biochemistry

THE UNIVERSITY OF TEXAS AT EL PASO

December 2018

Acknowledgements

I would firstly like to thank my graduate advisor, Dr. Villagrán, for all of the support, assistance, knowledge and opportunities he provided me during my graduate career. He was the one who introduced me into the field of electrocatalysis and sparked my interest in inorganic chemistry and physical chemistry. I joined his laboratory knowing very little about what I wanted to do and, under his guidance, have become very enthusiastic in what I have studied.

Secondly, I would like to thank my committee members, Dr. Pannell, Dr. Fortier and Dr. Lin, for giving me constructive suggestions and for always motivating me to reinforce my knowledge. I thank them for their patience and precious time.

I am also very grateful for having the chance to work with all of the talented graduate students from the Villagrán lab. I want to thank Nancy for the help with the DFT calculations in support of my research, Karen and Jose for giving me scientific inspirations and for helping me review my manuscripts and prepare my research talks, and finally Nathalie, Yulu, Mariana, and Ivan who shared so many valuable research ideas and would always offer me help. I enjoy the chemistry, laboratory and professional skills and everything else that I learned from every one of them.

I also had the chance to collaborate with many great undergraduate research assistants from UTEP, Isabel, Mario, Maria, Luis, and visiting students from Beijing Normal University, Weilu, Diya, Chu and Yuan. They all worked very hard and are very passionate about the research that we pursued together. A lot of the results shown in this dissertation are from their contributions.

Many of the research projects I worked on are in collaboration with students and professors from UTEP and other universities. These are very valuable opportunities and I learned from everyone that I worked with. I want to thank Dr. Chianelli, Dr. Zarei, Dr. Torres, Dr. Saupe and Tahmina for their help with instruments, materials, research discussions and preparing manuscripts. I also want to express my sincere appreciation for Dr. Thomas Jaramillo and Joel Sanchez from Stanford University, and Dr. Jorge Colón and Mario Ramos from University of

Puerto Rico Rio Piedras, with whom I truly enjoy collaborating under the work sponsored by the Center for Chemical Innovation in Solar Fuels (CCI Solar).

I am very lucky to have a very supportive family who encourage me to pursue my dream, even though I could not visit them often and be there when they needed me during the past five years. It was their unconditional love that made me get through my toughest moments. They are always the first ones I share my accomplishments with and are always the biggest motivation for me to fulfill my dreams.

Lastly, I want to thank my beloved fiancé, CJ, for his love and care. I cannot remember how many times he encouraged me when I doubted myself and hesitated. And I can never express enough how much I appreciate all of the sacrifices he made for me and that he would always put me first before everything else. It is a blessing to know that you have someone that you can always rely on. I am beyond excited about the new journey we are about to start together.

Abstract

Water splitting, which is the dissociation of water into hydrogen and oxygen gases, can be separated into two half reactions corresponding to the hydrogen evolution reaction and oxygen evolution reaction (HER and OER, respectively). Both reactions offer a promising way for storing energy into the form of chemical bonds, which is an important strategy for the development of clean-energy technologies. A main area of interest while studying HER and OER is to design effective and robust electrocatalysts made from earth-abundant materials. This dissertation describes several homogeneous and heterogeneous systems for the electrocatalytic generation of hydrogen and oxygen gases.

In Chapter 2, we present a metal-free (free-base) perfluorinated porphyrin as an electrocatalyst for HER, namely meso-tetra(pentafluorophenyl)porphyrin (**1**). Compound **1** is electrocatalytically active for hydrogen gas generation in the presence of p-toluenesulfonic acid. The electrochemical potential of hydrogen evolution (-1.31 V vs Fc/Fc^+ in THF) is comparable to those metal containing electrocatalysts such as metallated porphyrins or other metallated macrocycles. In combination of experimental data and DFT computations, we propose the most favorable hydrogen generation mechanism to be a (1) reduction, (2) protonation, (3) reduction, (4) protonation (*E-P-E-P*) pathway. Kinetic studies from foot-of-the-wave analysis (FOWA) show a linear relationship between the observed rate constants (k_{obs}) and acid concentrations.

Based upon these results, we have pursued several porphyrin-based polymeric systems as heterogeneous electrocatalysts, which are described in Chapters 3 and 4. We have synthesized a crystalline CoTcPP-based [TcPP = the dianion of meso-tetra(4-carboxyphenyl)porphyrin] polymeric system, **2**, as a HER electrocatalyst in acidic aqueous media. Polymer **2** shows a surface area of $441.74\text{ m}^2/\text{g}$, while the discrete CoTcPP molecule (**3**) has a surface area of $3.44\text{ m}^2/\text{g}$. The HER catalytic performance of **2** and **3** was evaluated by means of linear sweep voltammetry in the presence of $0.5\text{ M H}_2\text{SO}_4$ aqueous solution. To achieve $10\text{ mA}/\text{cm}^2$ cathodic current density, **2** and **3** respectively require an overpotential of 0.475 V and 0.666 V , providing strong evidence that the

extended network of cobalt porphyrin leads to enhanced HER efficiency. The polymer also shows great tolerance for HER electrolysis in the presence of acid remaining active over 10 h. Similarly, we constructed several amorphous cobalt porphyrin and iron porphyrin based organic polymers as electrocatalysts to heterogeneously generate oxygen gas in basic aqueous solution (0.1 M KOH). The porphyrin organic polymer [(Por)OP] and its fluorinated version [F(Por)OP] were synthesized from an one-step condensation reaction without further cross-coupling reactions, followed by direct metallation to form the metalloporphyrin polymers Co(Por)OP, CoF(Por)OP, Fe(Por)OP and FeF(Por)OP using Co^{2+} and Fe^{2+} accordingly. All metalloporphyrin polymers are active for the electrocatalytic oxygen evolution with modest overpotentials. The cobalt fluorinated porphyrin polymer, [CoF(Por)OP], shows the best catalytic efficiency ($\eta = 0.456$ at 10 mA/cm^2), while both the metal-free polymers, Por(OP) and FPor(OP), show negligible catalytic activity.

In Chapter 5, we extend the study of the heterogenization of porphyrin-based electrocatalysts by the immobilization of metalloporphyrin molecules using a supporting platform. We report the use of zirconium phosphate (ZrP) layered nanomaterials as a catalyst support for the intercalation of molecular electrocatalysts. Two cobalt porphyrins, namely CoTsPP [TsPP = the dianion of meso-tetra(4-sulfonatophenyl)porphyrin] and CoTcPP [TcPP = the dianion of meso-tetra(4-carboxyphenyl)porphyrin], were intercalated into ZrP layers and evaluated as heterogeneous OER electrocatalysts. Standard spectroscopic techniques including Fourier-transform infrared (FT-IR) spectroscopy, x-ray powder diffraction (XRPD) measurements, elemental mapping, energy dispersive x-ray (EDX) analysis and x-ray photoelectron spectroscopy (XPS) were utilized to determine the successful intercalation of cobalt porphyrin molecules into ZrP. The OER electrocatalytic performance of both intercalated species and the pristine α -ZrP are assessed by means of cyclic voltammetry in 0.1 M KOH aqueous solution. To reach 10 mA/cm^2 current density, CoTsPP/ZrP and CoTcPP/ZrP require an overpotential of 0.462 and 0.467 V, respectively. To compare, α -ZrP shows negligible electrocatalytic activity for OER.

Another molecular HER electrocatalyst is discussed in Chapter 6, $\text{Co}(\text{DippF})_2$ (where DippF is the anion of N,N'-bis[2,6-diisopropylphenyl]-formamidine), (**4**), which is able to

electrochemically produce hydrogen gas from the reduction of organic acids in homogeneous solutions. Compound **4** has a distorted square planar structure as evidenced through single crystal x-ray crystallography, and an effective magnetic moment of 4.13 that corresponds to three unpaired electrons. Catalyst **4** shows an irreversible cathodic peak at -1.59 V vs Fc/Fc^+ which is assigned to the reduction of Co^{II} to Co^{I} . In the presence of organic acids the onset of catalytic current is observed at -1.2 V, -1.45 V and -1.89 V vs. Fc/Fc^+ with p-toluenesulfonic acid, benzoic acid and phenol as the proton sources, respectively, in MeCN as the solvent. Detection of hydrogen gas was obtained by GC-MS with Faradaic efficiencies ranging from 85% to 100%. Kinetic studies using foot-of-the-wave analysis (FOWA) reveal a linear dependence of the observed rate constant against acid concentration in the range of 0.065 to 10.02 s^{-1} .

Chapter 7 describes several cobalt molybdenum disulfide (CoMoS_2) catalysts which are active electrocatalysts for the production of hydrogen gas. These highly-active catalysts are obtained from pretreatment of ammonium tetrathiomolybdate (ATM) with different amines precursors. Electrochemical studies indicate that these CoMoS_2 materials exhibit improved catalytic performance for hydrogen gas production with overpotentials ranging from 0.127 to 0.144 V, which are significantly less than CoMoS_2 synthesized directly from ATM under the same synthetic techniques (0.173 V). These CoMoS_2 catalysts are also stable in the presence of strong acidic media after 10 h while maintaining their efficiencies for hydrogen gas evolution.

Table of Contents

Acknowledgements	v
Abstract	vii
Table of Contents	x
List of Tables	xii
List of Figures	xiii
List of Illustrations	xix
Chapter 1: Introduction	1
Chapter 2: Hydrogen Gas Generation by a Metal-Free Fluorinated Porphyrin	6
2.1 Introduction.....	6
2.2 Experimental section	7
2.3 Computation details.....	10
2.4 Results and discussions	13
2.5 Conclusion	24
Chapter 3: Efficient Electrocatalytic Hydrogen Gas Evolution by a Cobalt-Porphyrin-based Crystalline Polymer	25
3.1 Introduction.....	25
3.2 Experimental section	26
3.3 Results and discussion.....	29
3.4 Conclusion	36
Chapter 4. Metalloporphyrin Organic Polymers as Effective and Stable Electrocatalysts for the Oxygen Evolution Reaction.....	37
4.1 Introduction.....	37
4.2 Experimental section	37
4.3 Results and discussion	42
4.4 Conclusions.....	47

Chapter 5: Cobalt Porphyrins Intercalated Zirconium Phosphate Layers as Electrocatalysts for the Oxygen Evolution Reaction	48
5.1 Introduction.....	48
5.2 Experimental section	49
5.3 Results and discussion.....	52
5.4 Conclusion	58
Chapter 6: Electrocatalytic Production of Hydrogen Gas by a Cobalt Formamidinate Complex	59
6.1 Introduction.....	59
6.2 Experimental section	60
6.3 Results and discussion.....	64
6.4 Conclusion	71
Chapter 7: Electrocatalytic Hydrogen Gas Generation by Cobalt Molybdenum Disulfide (CoMoS ₂) Synthesized using Alkyl-containing Thiomolybdate Precursors	72
7.1 Introduction.....	72
7.2 Experimental section	73
7.3 Results and discussion.....	77
7.4 Conclusion	84
Chapter 8: Conclusion.....	85
References	88
Appendix	111
Vita.....	121

List of Tables

Table 2.1. Hammett constants for substituents.	11
Table 2.2. Summary of m , and k_{obs} at different acid concentration.	18
Table 2.3. Calculated redox potentials and pKas in THF, values in parentheses correspond to the experimental values obtained in this work.	24
Table 6.1. Data collection and structure refinement for 4	61
Table 6.2. Sample and crystal data for 4	65
Table 6.4. Selected bond angles (°) for 4	65
Table 6.5. Summary of the results of FOWA slope (m), k_{obs} and k_{cat} at different acid concentration.	70
Table 7.1. Summary of the parameters of the CoMoS ₂ catalysts reported in this study.	75

List of Figures

Figure 2.1. Cyclic voltammograms of 0.1 mM 1 in a solution containing 0.1 M TBAPF ₆ with and without tosic acid: (from bottom to top): 0 equiv acid, 4 equiv acid, 9 equiv acid, and 12 equiv acid. Scan rate: 100 mV/s; glassy carbon working electrode.	14
Figure 2.2. Cyclic voltammograms of meso-tetraphenylporphyrin with 0.1 M TBAPF ₆ in THF and titrating with tosic acid: 100 mV/s; glassy carbon working electrode.	15
Figure 2.3. Controlled-potential electrolysis experiments containing 1 mM of 1 , 0.1M TBAPF ₆ and 10 mM tosic acid on a carbon rod electrode: 10 mM tosic acid with 1 mM of 1 (top), and 10 mM tosic acid without 1 (bottom). Potential: -1.7 V vs Fc/Fc ⁺ ;	15
Figure 2.4. Cyclic voltammograms recorded using the rinsed glassy carbon electrode after performing bulk electrolysis in the presence of 0.1 mM 1 at -1.7 V vs. Fc/Fc ⁺ for an hour. Scan rate: 100 mV/s; glassy carbon working electrode.	16
Figure 2.5. Cyclic voltammograms recorded using the rinsed glassy carbon electrode after performing bulk electrolysis in the presence of 0.1 mM 1 and 10 equiv tosic acid at -1.7 V vs. Fc/Fc ⁺ for 1 h. Scan rate: 100 mV/s; glassy carbon working electrode.	17
Figure 2.6. FOWA linear fit of 1 for hydrogen generation: 1.2 mM acid: slope = 2.144, R ² = 0.9874; 0.9 mM acid: slope = 1.956, R ² = 0.9876; 0.4 mM acid: 1.651, R ² = 0.9901.	17
Figure 2.7. Plot of observed rate constant versus acid concentration. (R ² = 0.9967)	18
Figure 2.8. UV-Vis spectrum of 1 in THF containing 0.1 M TBAPF ₆ before and after titrating with tosic acid.	19
Figure 2.9. Uv-vis spectroelectrochemistry of 1 in the absence and in the presence of tosic acid containing 0.1 M TBAPF ₆ in THF: (a) 1 at -1.35 V; (b) 1 containing tosic acid at -1.35 V; (c) 1 at -1.7 V; (d) 1 containing tosic acid at -1.7 V. (Potentials are referred to Fc/Fc ⁺ couple)	20
Figure 2.10. Change of absorption of 1 at 408 nm over time during electrolysis containing 1 M TBAPF ₆ in THF. (From bottom to top) (▼) -1.7 V without acid; (■) -1.35V without acid; (●) -1.35 V with tosic acid; (▲) -1.7 V with tosic acid (Potentials referred to Fc/Fc ⁺).	21

Figure 2.11. Free energy diagram of H ₂ evolution catalyzed by 1 in THF with tosic acid, as calculated by the Born-Haber cycles shown in Scheme 2.2 and Scheme 2.3. The free energies are plotted relative to the tosic acid/dihydrogen (TsOH/H ₂) couple.	22
Figure 3.1. p-XRD pattern of 2	29
Figure 3.2. (a, b) TEM images of 2 ; (c, d) SEM graphs of 2 ; (e, g) the corresponding elemental maps of C, O and Co respectively based on d and (h) overlay elemental mapping image of Co, C and O.	30
Figure 3.3. EDX spectrum of 2	31
Figure 3.4. N ₂ sorption isotherms at 77 K of 2 and 3	32
Figure 3.5. Cyclic voltammograms of 2 and 3 modified silver/FTO working electrodes in the presence of pH = 4.56 buffer solution. Scan rate: 50 mV/s.	32
Figure 3.6. (a) Polarization curves of Pt (black); 2 (blue); 3 (purple); and catalyst-free FTO/Silver (burgundy) in 0.5 M H ₂ SO ₄ electrolyte solution; Scan rate: 2mV/s; (b) Bulk electrolysis measurement of 2 (blue) and catalyst-free FTO/Silver (burgundy) in 0.5 M H ₂ SO ₄ electrolyte solution.	33
Figure 3.7. (a) Nyquist plots of the as-prepared 2 / Silver/FTO electrode at (from top to bottom): $\eta = 0.25, 0.30, 0.35$ and 0.40 V; (b) Chronoamperometric responses ($j \sim t$) of 1 in 0.5 M H ₂ SO ₄ aqueous solution for 10 h. (Applied potential: -0.4 vs. RHE)	34
Figure 3.8. Polarization curves of 2 before (solid line) and after (dotted line) 10 h' constant chronoamperometry analysis at -0.4 V vs. RHE.....	35
Figure 3.9. Tafel plots of 2 and 3	36
Figure 4.1. FT-IR spectra of (Por)OP, F(Por)OP, Co(Por)OP, CoF(Por)OP, Fe(Por)OP and FeF(Por)OP.....	42
Figure 4.2. XRPD patterns of (Por)OP, F(Por)OP, Co(Por)OP, CoF(Por)OP, Fe(Por)OP and FeF(Por)OP.....	43
Figure 4.3. SEM images of (a) (Por)OP, (b) Co(Por)OP, (c) Fe(Por)OP, (d) F(Por)OP, (e) CoF(Por)OP and (f) FeF(Por)OP.....	43

Figure 4.4. EDX spectra of (Por)OP, F(Por)OP, Co(Por)OP, CoF(Por)OP, Fe(Por)OP and FeF(Por)OP.....	45
Figure 4.5. Cyclic voltammograms of (Por)OP, F(Por)OP, Co(Por)OP, CoF(Por)OP, Fe(Por)OP, FeF(Por)OP and carbon black with <i>i</i> R compensation in the presence of 0.1 M KOH electrolyte solutions saturated with oxygen gas; Scan rate: 10 mV/s.	46
Figure 4.6. Tafel plots of Co(Por)OP, CoF(Por)OP, Fe(Por)OP and FeF(Por)OP in 0.1 M KOH.	47
Figure 5.1. FT-IR spectra of (from top to bottom): CoTsPP/ZrP; CoTsPP; CoTcPP/ZrP; CoTcPP and α -ZrP.....	52
Figure 5.2. Powder x-ray diffraction patterns of CoTsPP/ZrP, CoTcPP/ZrP and α -ZrP (from top to bottom).	53
Figure 5.4. EDX spectrum of CoTcPP/ZrP.	54
Figure 5.3. EDX spectrum of CoTsPP/ZrP.	54
Figure 5.5. EDX spectrum of α -ZrP.....	55
Figure 5.6. SEM image and the according elemental mapping graphs of pristine ZrP.	55
Figure 5.7. SEM image and the according elemental mapping graphs of CoTsPP/ZrP.	56
Figure 5.9. XPS survey of CoTsPP/ZrP, CoTcPP/ZrP and α -ZrP.....	57
Figure 5.8. Cyclic voltammograms of CoTsPP/ZrP, CoTcPP/ZrP, α -ZrP and carbon black on a rotating disk electrode. Scan rate: 10 mV/s.....	58
Figure 6.1. Solid-state crystal structure of 4 with thermal ellipsoid shown to be 50%. Hydrogen atoms were omitted for clarity. R(int) = 8.58% , R(sigma) = 2.95%.....	64
Figure 6.2. NMR spectrum of 4 from Evan's method experiment.	66
Figure 6.3. Cyclic voltammograms of 1 mM 4 without acid (black line) and with tosic acid (colored lines) in MeCN solution containing 0.1 M TBAPF ₆ . Scan rate: 100 mV/s; glassy carbon electrode (4 mm diameter).....	67

Figure 6.4. Cyclic voltammograms of 1 mM 4 without acid (black line) and with benzoic acid (colored lines) in MeCN solution containing 0.1 M TBAPF ₆ . Scan rate: 100 mV/s; glassy carbon electrode (4 mm diameter).....	68
Figure 6.5. Cyclic voltammograms of 1 mM 4 without acid (black line) and with phenol (colored lines) in MeCN solution containing 0.1 M TBAPF ₆ . Scan rate: 100 mV/s; glassy carbon electrode (4 mm diameter).....	68
Figure 6.6. Bulk electrolysis experiments of 1 mM 4 containing 10 mM of <i>tosic</i> acid, benzoic acid and phenol, respectively. Applied potential: -2.0 V vs. Fc/Fc ⁺	69
Figure 6.7. (a) FOWA plots of 1 mM of 4 at different concentration of <i>tosic</i> acid. Scan rate: 100 mV/s; (b) Linear sweep voltammograms of 4 in MeCN with 0.1 M TBAPF ₆ titration with <i>tosic</i> acid.	69
Figure 6.8. Plots of observed rate constant (k_{obs}) versus acid concentration ([H ⁺]).....	70
Figure 7.1. Calibration curve for evolved H ₂ quantification.	76
Figure 7.2. (a-d): Scanning electron micrographs of 5-8 , a-d respectively; e: SEM and the corresponding elemental mapping of 5	78
Figure 7.3. XRD patterns of CoMoS ₂ catalysts: 5 (red); 6 (purple); 7 (blue); 8 (green).	79
Figure 7.4. XPS survey of (a) 5 ; (b) 6 ; (c) 7 ; (d) 8	80
Figure 7.5. (a) Polarization data of Pt (black); 5 (red); 6 (purple); 7 (blue); 8 (green) and blank silver-coated FTO glass (burgundy) in 0.5 M H ₂ SO ₄ aqueous solution. Scan rate: 2 mV/s; (b) Nyquist plots of the as-prepared catalyst-deposited FTO/silver.....	81
Figure 7.6. Tafel plot [overpotential vs log (current density)] for (from bottom to top): Pt (black); 5 (red); 6 (purple); 7 (blue); 8 (green) derived from Figure 7.5a.	82
Figure 7.7. Bulk electrolysis experiments of (from top to bottom) 5-8 and blank silver-coated FTO glass in 0.5 M H ₂ SO ₄ aqueous solution. Applied potential: -0.5 V vs. RHE.	83
Figure 7.8. (a) Chronoamperometric responses ($j-t$) using 5-8 /silver/FTO working electrodes in 0.5 M H ₂ SO ₄ for 10 h at -0.2 V vs. RHE. Sample 5 (red); 6 (purple); 7 (blue); 8 (green) and	

blank silver-coated FTO glass (burgundy); (b) Polarization data of 5-8 in 0.5 M H ₂ SO ₄ aqueous solution before and after 500 cycles of scans . Scan rate: 2 mV/s.....	84
Figure A.1. Cyclic voltammogram of tosic acid in THF (no catalyst added); Scan rate: 100 mV/s; glassy carbon working electrode.	111
Figure A.2. Linear sweep voltammograms of 0.1 mM 1 (black) and 1 with 12 equivalent deuterated tosic acid (red).	111
Figure A.3. FOWA linear fit of 1 for hydrogen generation using 1.2 mM deuterated <i>tosic</i> acid.	112
Figure A.4. Uv-vis spectrum of [1] ²⁻ (black) and the spectrum recorded upon addition of tosic acid to [1] ²⁻ (red).	112
Figure A.5. UV-vis spectrum of H ₂ TcPP in EtOH.	113
Figure A.6. UV-vis spectrum of 3 in EtOH.....	114
Figure A.7. UV-vis spectrum of 2 dissolved in pH = 8 phosphate buffer solution.	114
Figure A.8. UV-vis spectrum of 2 dissolved in pH = 14 KOH aqueous solution. Precipitation of Co(OH) ₂ was observed.	115
Figure A.9. ¹ HNMR spectrum of 2 dissolved in pH = 8 phosphate buffer deuterium oxide solution. The spectrum shows broad signals besides the solvent peak, resulting from the d ⁷ Co ²⁺ center.	115
Figure A.10. Infrared spectra of 2 and 3	116
Figure A.11. Uv-vis spectrum of 4	116
Figure A.12. SEM and the corresponding elemental mapping images of 6	117
Figure A.13. SEM and the corresponding elemental mapping images of 7	117
Figure A.14. SEM and the corresponding elemental mapping images of 8	118
Figure A.15. SEM and the corresponding elemental mapping images of 5 after 10 h's eletrocatalysis in 0.5 M H ₂ SO ₄ at -0.2 V vs. RHE.	118
Figure A.16. SEM and the corresponding elemental mapping images of 6 after 10 h' eletrocatalysis in 0.5 M H ₂ SO ₄ at -0.2 V vs. RHE.	119

Figure A.17. SEM and the corresponding elemental mapping images of 7 after 10 h' eletrocatalysis in 0.5 M H ₂ SO ₄ at −0.2 V vs. RHE.	119
Figure A.18. SEM and the corresponding elemental mapping images of 8 after 10 h' eletrocatalysis in 0.5 M H ₂ SO ₄ at −0.2 V vs. RHE.	120

List of Illustrations

Scheme 1.1. Overall water splitting reaction, oxygen evolution reaction (OER) and hydrogen evolution reaction (HER).	3
Scheme 1.2. General structures of porphyrins and metalloporphyrins.	4
Scheme 2.1. Porphyrin derivatives involved in the proposed mechanistic pathways for hydrogen generation.	11
Scheme 2.2. Born-Haber thermodynamic cycle for the calculation of the free energy of reduction.	12
Scheme 2.3. Born-Haber thermodynamic cycle for the calculation of the free energy of proton transfer.	13
Scheme 2.4. Mechanistic pathways proposed for hydrogen generation in THF, with tosic acid as proton source.	21
Scheme 2.5. Proposed catalytic cycle for H ₂ evolution, following an <i>E-P-E-P</i> mechanism, with THF as solvent.	23
Scheme 4.1. Synthetic scheme of porphyrin organic polymers.	40
Scheme 4.2. Synthetic scheme of metalloporphyrin organic polymers.	41

Chapter 1: Introduction

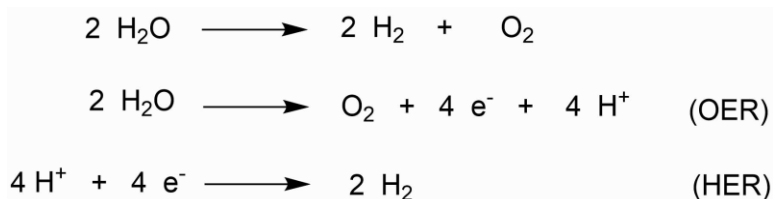
Current global energy consumption is obtained by the use of over 80% fossil fuel resources, namely coal, oil and natural gas.¹⁻³ Global energy demand is projected to reach 30 TW in 2050 and 46 TW by the end of this century, while the total energy consumption was ~13.5 TW in 2001.⁴ With the rapidly increasing energy demand due to fast economic and population growth as well as expanding industrialization, there is a rising concern for the use of fossil fuels because of their unsustainability and environmental constraints.^{5,6} Global warming and climate change have emerged as major concerns human beings face in nowadays society, which are attributed to the increasing emission of greenhouse gases (GHGs) closely associated with the combustion of fossil fuels.^{7,8} In addition, the heavy dependence of nation development on fossil fuels is one of the obstacles of world peace and security.⁶ Therefore, in response to the ever-growing worldwide energy demand and the environmental and safety crisis accompany the use of fossil fuels, substantial current research efforts have been devoted to identify other alternative sustainable and environmentally benign energy systems.⁹⁻¹⁴

Hydrogen gas (H_2) is considered to be an ideal fuel since its combustion generates carbon-free emissions and it has high gravimetric energy density.^{15,16} In addition to be used directly as an efficient fuel, H_2 can also be used as a feedstock to derive other gas or liquid energy products such as ammonia, methane and liquid hydrocarbons.¹⁷⁻¹⁹ Conventionally, H_2 is produced through the steam reforming of methane, which is a fossil-based process and requires high energy input.²⁰ Thus, it is highly desirable to design other clean, fossil-free pathways for hydrogen gas production.^{21,22} Water electrolysis is a process that electrically dissociates water molecules to form H_2 and O_2 , which is a promising approach for clean hydrogen production especially if the energy is renewable energy.^{23,24} Combining H_2 and O_2 can also regenerate electricity power along with the release of water via fuel cells, making this process zero-emission. Additionally, water is an attractive medium as both energy absorber and converter since splitting two molecules of water to yield H_2 and O_2 facilitates up to 4.92 eV of energy being stored into chemical bonds.¹⁰ Water

electrolysis consists of two separate half reactions, which is the hydrogen evolution reaction (HER) and the oxygen evolution reactions (OER) (Scheme 1). Splitting water is a thermodynamically unfavorable and kinetically challenging process with Gibbs free energy change of $+237 \text{ kJ mol}^{-1}$ and high overpotential because it generates high energy intermediates.^{10,25,26} In addition, both OER and HER encompass multi-electron transfer processes.¹⁰ OER proceeds via the abstraction of four electrons, which is the kinetic bottleneck of water splitting, while HER involves two electron-proton coupled reactions.^{27,28} Green plants have been effectively converting water into hydrogen and oxygen gases using solar energy via photosynthesis,²⁹ and significant progress has been made by researchers to lower the kinetic barrier and overpotential loss of water electrolysis by the application of electrocatalysts.³⁰ Discovering and designing new catalytic systems for HER and OER has become a prominent and active field of research.^{31–33}

Electrocatalysts can be categorized into homogeneous and heterogeneous systems.^{34,35} In homogeneous catalysis, catalysts molecules are dissolved in the solution containing the reactant substrates. Alternatively, in heterogeneous catalysis, catalysts materials are typically immobilized on the electrode surfaces and are in different phase as the substrates.^{4,34,35} Homogeneous catalysts must diffuse to the conductive electrode surfaces to enable electrocatalysis while heterogeneous systems provide more active catalytic sites contacting both the electrodes and reactants.³⁶ Thus, heterogeneous catalytic systems typically exhibit superior catalytic performance comparing to homogeneous ones.³⁵ However, studies of homogeneous catalysts are necessary for the elucidation of fundamental mechanism of the catalytic processes.^{37,38} Platinum metal is well known for being the most promising HER electrocatalyst which operates at practical zero overpotential and generates large current density, while iridium and ruthenium based oxides are the most efficient OER electrocatalysts.^{10,39–41} However, their practical implementation in scalable water electrolysis technology has been constrained by the high-cost and scarcity of these precious metals. Thus, numerous researches have been stimulated to explore HER and OER electrocatalysts derived from earth-abundant elements.^{4,22,26} Frequently studied heterogeneous electrocatalysts for HER and OER mainly base on transition metal (Co, Fe, Ni, Mn,) materials, including transition metal

alloys,^{42,43} chalcogenides,^{44–48} phosphides,^{49–53} oxides,^{54–57} among others.^{31,58–60} Several novel metal-free heterogeneous electrocatalytic systems have also emerged and shown comparable catalytic activities to metal-based catalysts such as heteroatoms (B, N, P) doped graphene materials and organic polymers.^{61–67} The pursuit of understanding the mechanistic insights of HER and OER at a molecular level also led to extensive studies conducted on molecular electrocatalysts through both computational and experimental approaches, which include transition-metal macrocycles,^{68–74} cobaloximes^{75–77} and bio-inspired hydrogenase organometallic complexes,^{78,79} among other compounds.⁸⁰ In general, these catalytic systems aim to overcome the following three fundamental restraints: (1) high activation energy and slow kinetics of HER and OER; (2) short lifetime of the catalysts during long-time catalysis; (3) lack of noble-metal free alternatives.

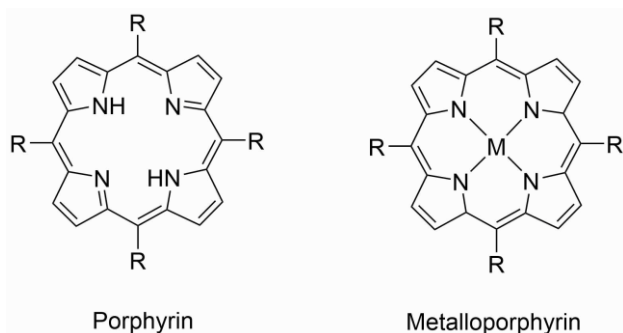


Scheme 1.1. Overall water splitting reaction, oxygen evolution reaction (OER) and hydrogen evolution reaction (HER).

Porphyrins are a group of organic macrocycles composed of four pyrroles linked by methine bridges at their α -carbons (Scheme 1.2), which are conjugated aromatic rings.⁸¹ The four pyrrolic nitrogens in the porphyrin cavity are suited for binding metals to form stable metalloporphyrins.⁸² Metalloporphyrins exist widely in nature and play an important role in many critical biological processes. As an example, the active site in hemoglobin contains an iron porphyrin complex, which is the key component for oxygen binding, activation, storage and transportation in human bodies.⁷¹ Other natural sources containing porphyrin-based molecules include chlorophylls, cytochromes and petroleum, etc.^{83–86} Recent decades have also witnessed significant development of chemical and physical strategies for the synthesis and characterization of porphyrins of diverse types.^{87–89} Due to their interesting electrochemical and photochemical properties, porphyrins and metalloporphyrins are among one of the most studied groups of

complexes in a variety of applications such as molecular sensor, photonic devices, catalysis, among others.^{90–95} Of particular interest, porphyrin-based materials have been well documented as versatile electrocatalysts for HER and OER, while several porphyrin-based catalytic systems have been found to be dual-functional electrocatalysts.^{68,93,96–99}

Transition metal-based metalloporphyrin molecules are intensively evaluated as homogeneous electrocatalysts for HER and OER.^{68,96,100} In metalloporphyrins, the electron-deficient and redox-active porphyrins perform as electron reservoir to stabilize the electron-rich metal cores during catalysis.¹⁰¹ The catalytic efficiency and selectivity of metalloporphyrins can be conveniently tuned by modulating the electronic properties of the central metals through flexible ligand designs.¹⁰² Molecular metalloporphyrins are also suitable models for experimental and theoretical studies of fundamental electrocatalytic properties. The single metal atom inside the porphyrin core is generally the redox and catalytic center, while a few studies suggesting that the electron and proton transfers were induced by the redox active porphyrins to mediate hydrogen production under certain conditions.^{37,69,103} Interestingly, recent reports in the literature have described successful electrocatalytic HER by several metal-free catalytic systems which exploit porphyrin units as the catalytically active sites.^{61,104} However, very little research has been focused on elucidating how metal-free electrocatalysts operate electrocatalysis at a fundamental molecular level. One of the objectives in this dissertation is to illustrate the HER electrocatalytic activity using a free-base molecular porphyrin by electrochemical measurements and study the HER mechanistic pathways.



Scheme 1.2. General structures of porphyrins and metalloporphyrins.

Despite of the fact that molecular porphyrin-based electrocatalysts are well suited for electrochemical tuning and mechanistic analysis, homogeneous catalytic systems are constrained from widespread practical application due to their intrinsic disadvantages:¹⁰² (1) metalloporphyrin complexes may suffer from low stability for constant electrolysis especially under severe acidic or basic conditions, which are commonly used for the investigation of water electrolysis. Both metal dissolution and ligand degradation may occur during long-term electrocatalytic operation resulting in quenching of catalytic activity; (2) Homogeneous catalysts also suffer from low efficiency due to mass transport issues and relatively low density of exposed active sites. Thus, the construction of efficient and feasible devices for water electrolysis has provoked different strategies for the heterogenization of HER and OER electrocatalysts, which include, but not limited to, (1) direct adsorption of molecular electrocatalysts on the surfaces of electrode materials such as glassy carbon and fluorine-dope tin oxide electrodes,^{105–107} (2) immobilization of electrocatalysts by covalently attaching or π - π stacking to a catalyst support including graphene, carbon nanotubes and boron nitride nanosheets, among others,^{108–113} (3) coordination of molecular complexes to form covalent organic polymers (COFs) or metal-organic frameworks (MOFs).^{98,114,115} Later sections of this dissertation will focus on different strategies of fabricating heterogeneous OER electrocatalysts based upon electrocatalytic active metalloporphyrin molecules. We have used metalloporphyrins as building blocks to construct amorphous and crystalline polymer systems which were evaluated as heterogeneous electrocatalysts. Another approach shown in this dissertation to heterogenize porphyrin-derived molecular electrocatalysts involve the intercalation of metalloporphyrin molecules in zirconium phosphate (ZrP) materials, which function as a layered supporting platform. We aim to enhance the catalytic performance by increasing the number of catalytic active site exposed to the electrolyte and electrode while maintaining the inherent properties of the molecular catalyst units. The strong attachment of the catalysts through polymeric network and catalyst support is also expected to provide stronger stability.

Chapter 2: Hydrogen Gas Generation by a Metal-Free Fluorinated Porphyrinⁱ

2.1 INTRODUCTION

In this chapter we describe a metal-free system for the electrocatalytic generation of hydrogen gas from acidic organic solutions using a free-base perfluorinated porphyrin and the mechanistic studies through both spectroscopic and computational approaches.

Metalloporphyrins have been well investigated for their ability to generate H₂ both electrochemically and photochemically.^{37,68,93,96,116,117} In metallated HER electrocatalysts, the metal center is the active site in the hydrogen production process by participating in the formation of metal-hydrogen bonds and as the redox center in the multi-electron reduction process.^{72,96,118,119} In comparison, free-base porphyrins are known to exhibit rich multi-electron redox chemistry.^{120,121} The two basic imine nitrogen atoms in the porphyrin core can produce a diprotonated porphyrin species.^{122,123} Thus, free-base porphyrins have the ability to form covalent nitrogen-hydrogen bonds and can also be electrochemically active. In addition, the four-nitrogen porphyrin core is perfectly suited for bringing protons in close proximity to lower the activation energy of dihydrogen production by prearranging the transition state of hydrogen-hydrogen bond formation. However, whether a molecular metal-free porphyrin has the ability to perform similar and comparable electrocatalytic HER activity to the existing well-studied metallated macrocyclic complexes has not yet been studied or reported. Organic-based hydrogen generation catalysts may provide superior synthetic flexibility, lower manufacturing costs, and greater chemical stability.

In this work we show that free-base meso-tetra(pentafluorophenyl)porphyrin, **1**, is a HER electrocatalyst in the presence of p-toluenesulfonic (tosic) acid as the proton source with THF as the solvent. The electrocatalytic activity of **1** was estimated by electrochemical studies and H₂ gas analysis in acidic solutions. Spectroscopic measurements including UV-vis spectra and spectroelectrochemical studies reveal the spectral signatures of the intermediates during the catalysis giving insight into the mechanism of H₂ generation. In addition, density functional theory

ⁱ This chapter is excerpted with permission from a published article: Yanyu Wu, Nancy Rodríguez-López, Dino Villagrán; Hydrogen Gas Generation by a Metal-Free Fluorinated Porphyrin. *Chemical Science*, **2018**, 9, 4689-4695.

(DFT) calculations were performed to provide further support to the mechanistic HER behavior of **1**.

2.2 EXPERIMENTAL SECTION

2.2.1 Materials.

All reagents used for synthesis were purchased from Sigma Aldrich. Pyrrole was freshly distilled prior to use. Solvent used for electrochemical studies were dried and degassed through a Pure Process Technology solvent purification system. Tetrabutylammonium hexafluorophosphate (TBAPF₆) and tosic acid were purchased from Acros Organic. Meso-tetra(pentafluorophenyl)porphyrin and meso-tetraphenylporphyrin were synthesized according to Lindsey's method.⁸⁷

2.2.2 Synthesis of meso-tetra(pentafluorophenyl)porphyrin, **1.**

Pentafluorobenzaldehyde (3.00 g, 0.0153 mol) was dissolved in 500 mL of DCM, followed by addition of pyrrole (1.04 g, 0.0153 mol) dropwise. The mixture was stirred and bubbled with N₂ for 15 minutes. Next, 0.500 mL of BF₃·Et₂O was added with a glass syringe without exposing to air. After 2 h, the resulting porphyrinogen was oxidized by adding 2,3-dichloro-5,6-dicyanobenzoquinone (DDQ) (5.00 g, 0.0220 mol) and letting it react for 30 minutes. Compound **1** (1.80 g, 24.3% yield) was obtained after recrystallization and column chromatography purification on silica gel eluted with a mixture of hexane and dichloromethane (2:1). ¹H NMR (C₆D₆): 8.71 ppm (s, 8H), -2.10 ppm (s, 2H); ¹⁹F NMR (C₆D₆): -161.3 ppm (t, 2F), -150.5 ppm (t, 1F), -137.2 ppm (d, 2F); ESI-MS: m/z: 975.5; UV-vis (THF): λ max 408, 503, 543, 584, 634 nm.

2.2.3 Cyclic voltammetry.

All electrochemical measurements were obtained by using a CHI760D potentiostat, with 0.1 M TBAPF₆ as the supporting electrolyte. The electrolyte and tosic acid were placed under vacuum and oven dried prior to use. All cyclic voltammograms were obtained in a dry N₂-filled

glovebox, using a 4 mm diameter glassy carbon working electrode, Pt mesh auxiliary counter electrode and an Ag/Ag⁺ reference electrode. Ferrocene (Fc) was added after each measurement as an internal standard.

2.2.4 Controlled-potential electrolysis and H₂ detection.

Controlled-potential electrolysis was done in a custom-built two-compartment gas-tight electrochemical cell under argon atmosphere. One part of the cell contains: (I) a carbon rod working electrode (3 mm diameter, 0.95 mm length); (II) Ag/Ag⁺ reference electrode; (III) gas inlet and gas outlet. The other part of the cell contains a Pt auxiliary wire counter electrode and gas outlet. The working and counter electrodes are separated through a glass frit. Electrolysis was carried out at -1.7 V vs Fc/Fc⁺ in THF, containing 0.1 M TBAPF₆, 10 mM tosic acid with and without adding the catalyst.

2.2.5 Spectroelectrochemistry.

Spectroelectrochemistry was performed using an optical transparent 1 mm thin-layer spectroelectrochemical cell containing an Au gauze working electrode, non-aqueous Ag/Ag⁺ reference electrode and Pt wire counter electrode. The absorption spectra were recorded in a UV-vis spectrophotometer while the bulk electrolysis was performed by the CHI760D potentiostat. Solutions of **1** containing 0.1 M TBAPF₆ with and without acid were prepared and degassed with N₂ before each measurement. The changes of the UV-vis spectra were recorded at one second interval for 10 minutes at different applied potentials.

2.2.6 Calculation of overpotential.

Overpotential is calculated through $|E_{H^+} - E_{cat/2}|$, where E_{H^+} is the equilibrium potential of H⁺/H₂ of tosic acid in THF and $E_{cat/2}$ is the potential at $i_{cat/2}$. E_{H^+} is equal to the open circuit potential of tosic acid in THF solution using a platinum electrode at 1 atm hydrogen gas atmosphere.

2.2.7 Calculation of k_{obs} from foot-of-the-wave analysis (FOWA).

Foot-of-the-wave analysis (FOWA) was used to determine the observed rate constant (k_{obs}) of hydrogen generation of **1**. For an ECEC mechanistic process:¹²⁴

$$i = \frac{2FAC_p^0 \sqrt{Dk_{obs}}}{1 + e^{\left[\frac{F}{RT}(E - E_{cat}/2)\right]}} \quad \text{Eq 2.1}$$

Where i is the catalytic current density (A/cm²), F is the Faraday constant (96485 C/mol), A is the surface area of the working electrode (cm²), C_p^0 is the concentration of the catalyst (mol/L), T is the temperature (298 K), D is the diffusion coefficient (cm²/s) and k_{obs} is the observed rate constant, according to the Randles-Sevcik equation, the peak current i_p of a reversible catalytic wave can be described as:¹²⁵

$$i_p = 0.4463 FAC_p^0 \sqrt{\frac{FvD}{RT}} \quad \text{Eq 2.2}$$

From Eq 2.1 and Eq 2.2, we can obtain:

$$\frac{i}{i_p} = \frac{2\sqrt{\frac{RT}{Fv}}\sqrt{k_{obs}}}{0.4463} * \frac{1}{1 + e^{\left[\frac{F}{RT}(E - E_{cat}/2)\right]}} \quad \text{Eq 2.3}$$

Then $\frac{i}{i_p}$ is plotted versus $\frac{1}{1 + e^{\left[\frac{F}{RT}(E - E_{cat}/2)\right]}}$ and the linear portion was selected to yield a

line with a slope of m , which can be represented by:

$$m = \frac{2\sqrt{\frac{RT}{Fv}}\sqrt{k_{obs}}}{0.4463} \quad \text{Eq 2.4}$$

Thus k_{obs} can be calculated through:

$$k_{obs} = \frac{(m)^2 (0.4463)^2 Fv}{4RT} \quad \text{Eq 2.5}$$

The catalytic rate constant (k_{cat}) is expressed as:

$$k_{cat} = \frac{k_{obs}}{[H^+]} \quad \text{Eq 2.6}$$

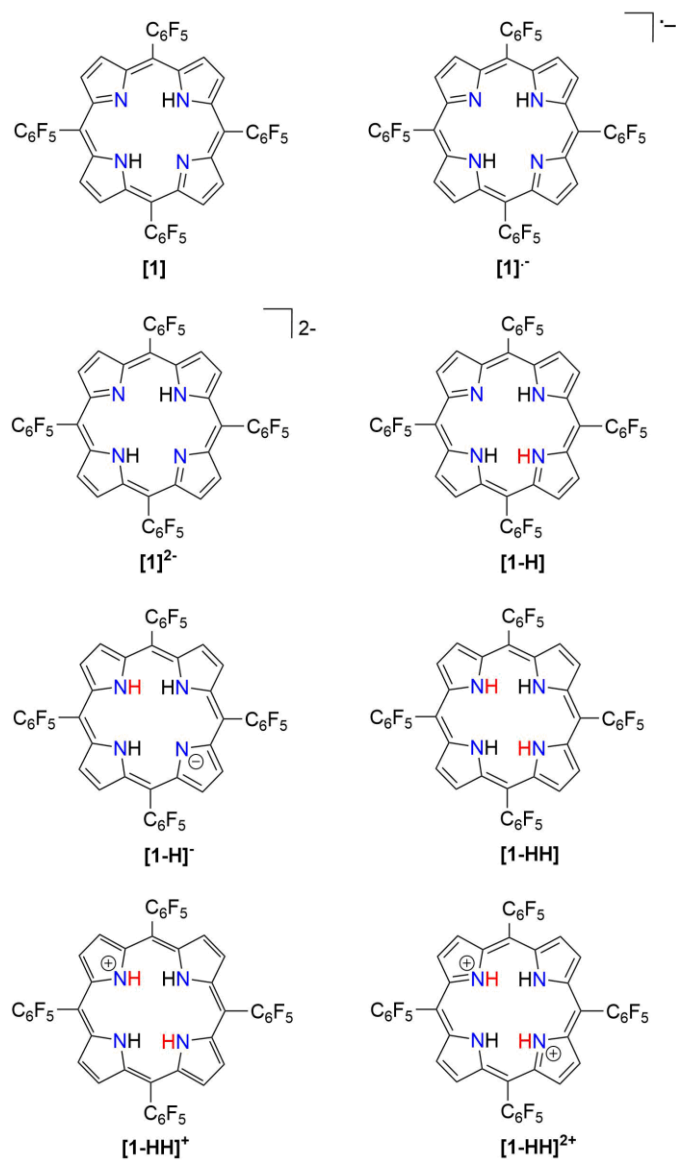
2.2.8 Other physical methods.

^1H NMR and ^{19}F NMR spectra were recorded on a JEOL 600 MHz NMR spectrometer. Proton NMR spectrum was referenced to the residual deuterated solvent signal as an internal calibration ($\text{C}_6\text{D}_6 = 7.16$ ppm). The UV-vis spectra were recorded on a SEC2000 spectra system equipped with a VISUAL SPECTRA 2.1 software.

2.3 COMPUTATION DETAILS

The molecular geometries of all free base porphyrins were optimized using density functional theory (DFT). The DFT method employed was Becke's¹²⁶ three parameter hybrid exchange functional, coupled with the Lee-Yang-Parr¹²⁷ nonlocal correlational functional (B3LYP) for all calculations. The 6-31+G^{128,129} Pople basis set, as implemented in Gaussian 09, was used for all atoms.¹³⁰ Zero point energies and thermodynamic data were calculated at 298.15 K and 1 atm by performing frequency calculations. Calculations were performed on the optimized gas-phase geometries using the solvation model based on density (SMD) as implemented in the Gaussian 09 suite.^{131–133}

In order to ease the computational expense a model in which the pentafluorophenyl groups are replaced with chlorine atoms was employed. This substitution is reasonable due to the similar electron-withdrawing ability of Cl compared to $-\text{C}_6\text{F}_5$ as supported by their Hammett substitution constants (Table 2.1). We followed several theoretical models^{37,38,69,117,134–139} for the determination of thermodynamic quantities such as reduction potentials and $\text{p}K_{\text{a}}$ s so as to give insight on the hydrogen evolution mechanism



Scheme 2.1. Porphyrin derivatives involved in the proposed mechanistic pathways for hydrogen generation.

Table 2.1. Hammett constants for substituents.¹⁴⁰

<i>Substituent</i>	σ_m	σ_p
C_6F_5	0.26	0.27
Cl	0.37	0.23
F	0.34	0.06

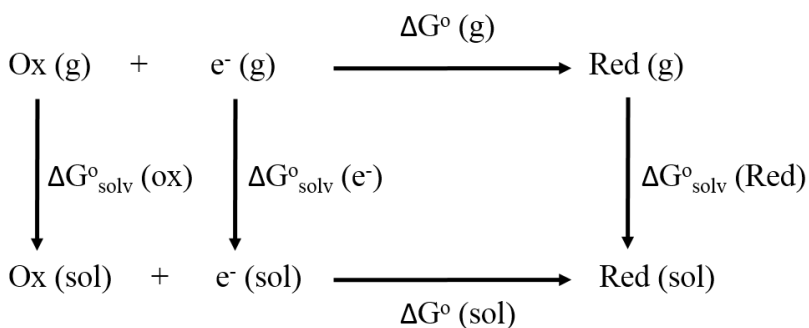
Calculation of reduction free energies. From a Born-Haber thermodynamic cycle (Scheme 2.2), we can associate the reaction free energies with the gas-phase and solvation energies using equation 2.7:

$$\Delta G^{\circ}_{\text{(sol)}} = \Delta G^{\circ}_{\text{(g)}} + \Delta G^{\circ}_{\text{solv}}(\text{Red}) - \Delta G^{\circ}_{\text{solv}}(\text{Ox}) - \Delta G^{\circ}_{\text{solv}}(\text{e}^{-}) \quad \text{Eq 2.7}$$

where $\Delta G^{\circ}_{\text{solv}}(\text{Red})$ and $\Delta G^{\circ}_{\text{solv}}(\text{Ox})$ represent the free energies upon solvation for both the reduced and oxidized species, $\Delta G^{\circ}_{\text{solv}}(\text{e}^{-})$ the contribution of the electron to the solvation free energy, and $\Delta G^{\circ}_{\text{(g)}}$ the free energy of the reaction in the gas phase. We can calculate the last value with the expression $\Delta G^{\circ}_{\text{(g)}} = \Delta H^{\circ}_{\text{(g)}} - T\Delta S^{\circ}_{\text{(g)}}$. Calculation of $\Delta G^{\circ}_{\text{(sol)}}$, allows the determination of redox potentials using equation 2.8:

$$E^{\circ} = (-\Delta G^{\circ}_{\text{sol}} / nF) + E^{\circ}_{\text{ref}} \quad \text{Eq 2.8}$$

where E° is the standard reduction potential, F is the Faraday constant and n is the number of electrons involved in the redox reaction. In order to allow a direct comparison of calculated vs experimental data, the redox potentials are reported referenced to the Ferrocene/Ferrocenium (Fc/Fc^{+}) couple.



Scheme 2.2. Born-Haber thermodynamic cycle for the calculation of the free energy of reduction.

Calculation of proton dissociation free energies. The direct calculation of reaction free energies in solution cannot be performed because the free energy of the solvated proton is difficult to calculate with accuracy. In order to calculate the thermodynamic value, we need to consider a proton-exchange reaction between a reference compound (AH) and the free base porphyrin (1):



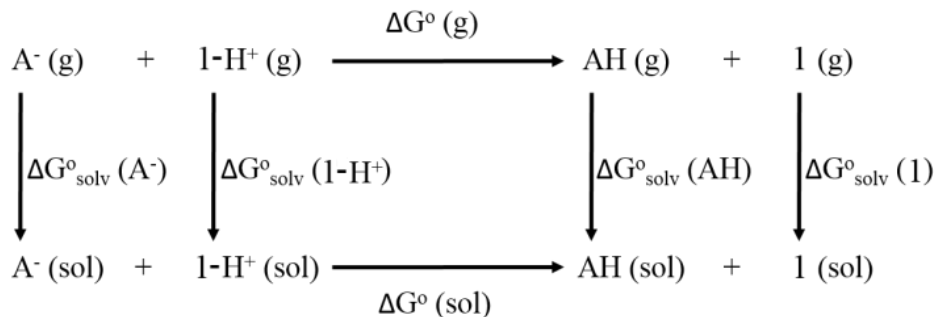
Herein, we define the free energy change of reaction (2.9) as $\Delta G^\circ_{(sol)}$. To calculate $\Delta G^\circ_{(sol)}$, we must relate it to the free energy in the gas phase using the thermodynamic cycle depicted in Scheme 2.3, obtaining the following equation:

$$\Delta G^\circ_{(sol)} = \Delta G^\circ_{(g)} + \Delta G^\circ_{solv}(AH) + \Delta G^\circ_{solv}(1) - \Delta G^\circ_{solv}(A^-) - \Delta G^\circ_{solv}(1-H^+) \quad \text{Eq 2.10}$$

where $\Delta G^\circ_{solv}(A^-)$, $\Delta G^\circ_{solv}(1-H^+)$, $\Delta G^\circ_{solv}(AH)$ and $\Delta G^\circ_{solv}(1)$ are the free energies upon solvation of the referenced conjugated base, the protonated porphyrin, the referenced acid and the porphyrin, respectively. We can calculate $\Delta G^\circ_{(g)}$ by the expression $\Delta G^\circ_{(g)} = \Delta H^\circ_{(g)} - T\Delta S^\circ_{(g)}$. The pK_a can be calculated from $\Delta G^\circ_{(sol)}$ by:

$$pK_a = (\Delta G^\circ_{sol} / 2.303 RT) + pK_{a(ref)} \quad \text{Eq 2.11}$$

where R is the gas constant, T is the temperature (298.15 K), and $pK_{a(ref)}$ is the experimentally reported pK_a of the reference reaction. Since the deprotonation of acetic acid has been studied in THF and the pK_a value is available, we chose this reaction as our reference.¹⁴¹



Scheme 2.3. Born-Haber thermodynamic cycle for the calculation of the free energy of proton transfer.

2.4 RESULTS AND DISCUSSIONS

Cyclic voltammetry experiments were conducted in THF in order to assess the electrocatalytic activity of **1**. In the absence of acid, **1** features two reversible one-electron reductions at $E_{1/2} = -1.14$ V and $E_{1/2} = -1.54$ V vs Fc/Fc^+ that yield the porphyrin radical anion $[1]^\cdot$ and the dianion species $[1]^{2-}$, respectively (Figure 2.1). Upon successive addition of tosic

acid, the first reduction wave of **1** remains unchanged while a catalytic wave appears at a potential near -1.31 V vs Fc/Fc^+ , which occurs before the second reduction wave of **1** at -1.54 V. This indicates that protonation of this porphyrin is not possible under these conditions prior to the one-electron reduction. The reduction potential of H^+/H_2 (E_{H^+}) with tosic acid in THF is -0.605 V vs Fc/Fc^+ , which corresponds to an overpotential of 1.02 V.^{141,142} Notably, addition of acid without the presence of **1** shows negligible current increase (Figure A.1). As a control, a second metal-free porphyrin, meso-tetraphenylporphyrin was also evaluated as HER electrocatalyst using tosic acid as the proton source. The electrocatalytic current achieved by this porphyrin was very low (Onset potential: -1.89 V vs. Fc/Fc^+ ; Peak current: 18 μA . See Figure 2.2).

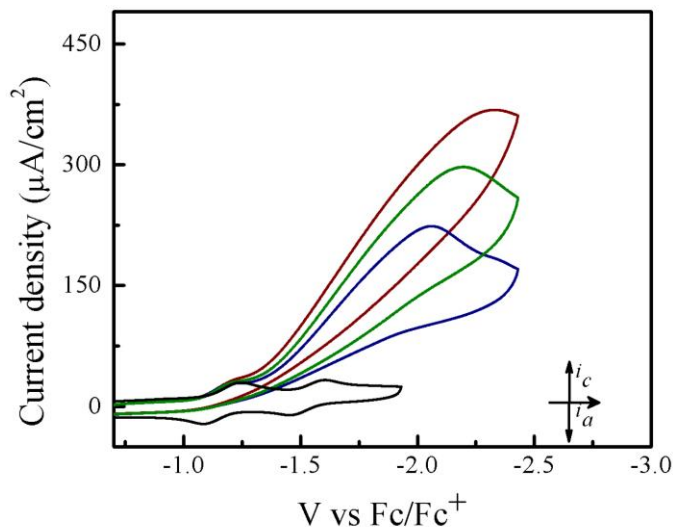


Figure 2.1. Cyclic voltammograms of 0.1 mM **1** in a solution containing 0.1 M TBAPF₆ with and without tosic acid: (from bottom to top): 0 equiv acid, 4 equiv acid, 9 equiv acid, and 12 equiv acid. Scan rate: 100 mV/s; glassy carbon working electrode.

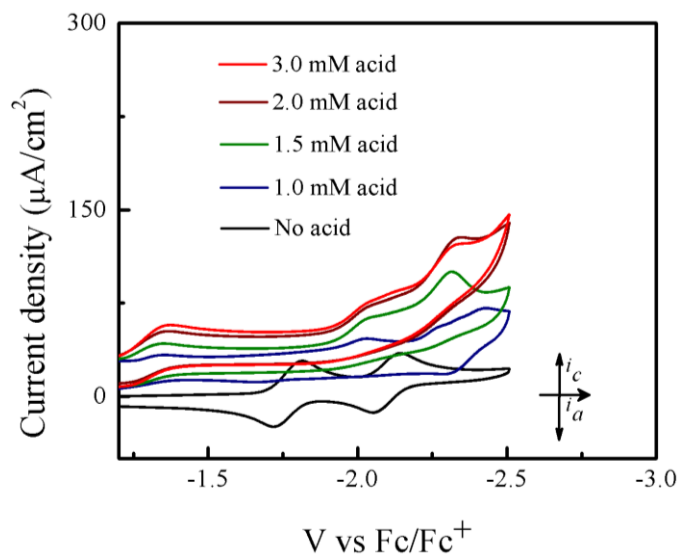


Figure 2.2. Cyclic voltammograms of meso-tetraphenylporphyrin with 0.1 M TBAPF₆ in THF and titrating with tosic acid: 100 mV/s; glassy carbon working electrode.

Hydrogen gas production was confirmed by Gas Chromatography through the evaluation of the gas product obtained from controlled potential electrolysis. Figure 2.3 depicts the dependence of accumulated charge over 40 minutes, resulting in 3.2 C of charge corresponding to 90% Faradaic efficiency. (See experimental section for full experimental details)

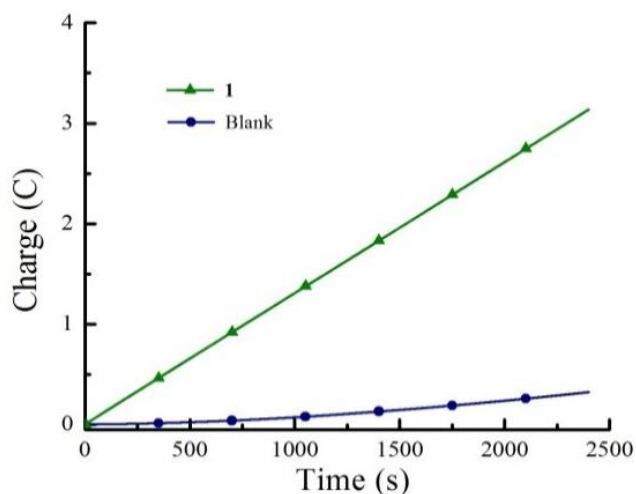


Figure 2.3. Controlled-potential electrolysis experiments containing 1 mM of **1**, 0.1M TBAPF₆ and 10 mM tosic acid on a carbon rod electrode: 10 mM tosic acid with 1 mM of **1** (top), and 10 mM tosic acid without **1** (bottom). Potential: -1.7 V vs Fc/Fc⁺;

In order to investigate whether there is a formation of a heterogeneous metal-free porphyrin thin film on the working electrode, which can be responsible for HER activity, cyclic voltammograms were obtained using a glassy carbon electrode after performing controlled-potential electrolysis. Two glassy carbon electrodes were subjected to 1 h of electrolysis in the presence of **1** with and without tosic acid, respectively. After the experiment, the electrodes were rinsed with THF and dried in air. Then they were exposed to fresh acidic solutions (1.5 mM) without the addition of **1**. In neither case the working electrode shows any increase of catalytic current (Figures 2.4-2.5), implying that **1** does not adsorb on the working electrode surface during our electrochemical studies.

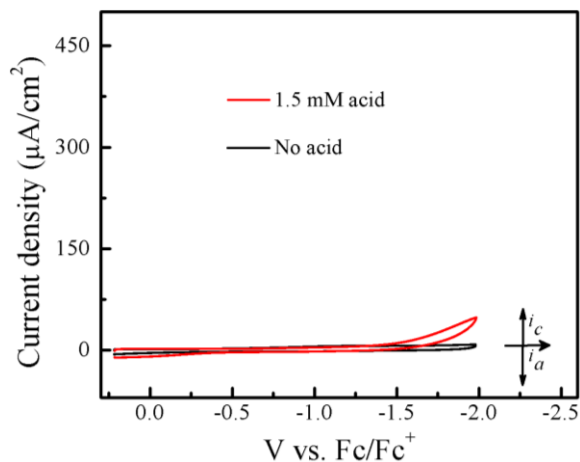


Figure 2.4. Cyclic voltammograms recorded using the rinsed glassy carbon electrode after performing bulk electrolysis in the presence of 0.1 mM **1** at -1.7 V vs. Fc/Fc^+ for an hour. Scan rate: 100 mV/s; glassy carbon working electrode.

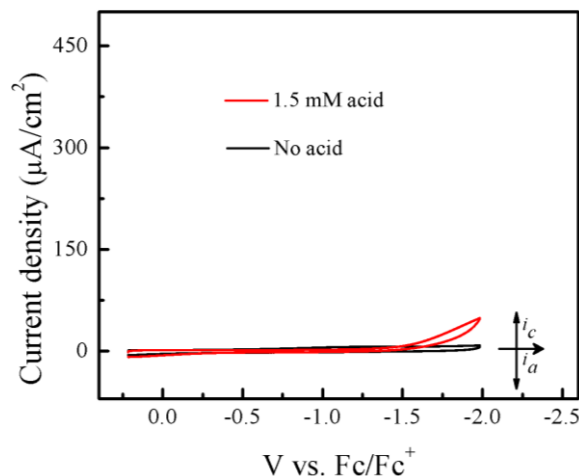


Figure 2.5. Cyclic voltammograms recorded using the rinsed glassy carbon electrode after performing bulk electrolysis in the presence of 0.1 mM **1** and 10 equiv tosic acid at -1.7 V vs. Fc/Fc^+ for 1 h. Scan rate: 100 mV/s; glassy carbon working electrode.

HER kinetics were measured by foot-of-the-wave analysis (FOWA). The observed rate constant (k_{obs}) was calculated from the slope of the linear region near the foot of the wave (Figure 2.6.). The calculated k_{obs} are displayed in Table 2.2, showing values of 0.528, 0.742 and 0.891 S^{-1} at acid concentration ($[\text{H}^+]$) of 0.4, 0.9 and 1.2 mM respectively. Plotting k_{obs} versus $[\text{H}^+]$ gives a linear relationship (Figure 2.7), suggesting a first order dependence of $[\text{H}^+]$. A kinetic isotope effect (KIE) of 1.16 was observed when using deuterated tosic acid ($\text{C}_7\text{H}_7\text{SO}_3\text{D}$).

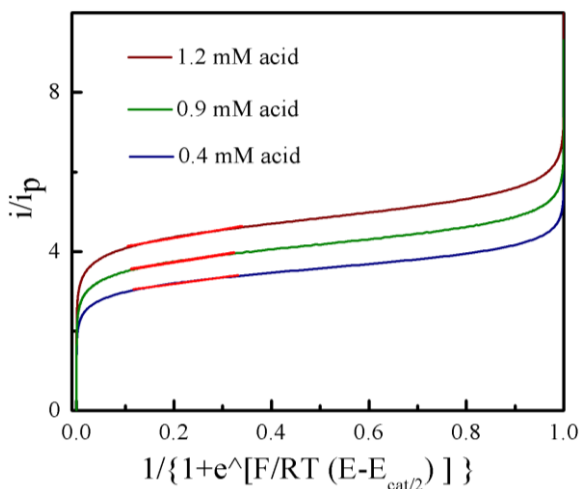


Figure 2.6. FOWA linear fit of **1** for hydrogen generation: 1.2 mM acid: slope = 2.144, $R^2 = 0.9874$; 0.9 mM acid: slope = 1.956, $R^2 = 0.9876$; 0.4 mM acid: 1.651, $R^2 = 0.9901$.

Table 2.2. Summary of m , and k_{obs} at different acid concentration.

$[H^+]$ (mM)	m	k_{obs} (s^{-1})
0.4	1.651	0.528
0.9	1.956	0.742
1.2	2.144	0.891

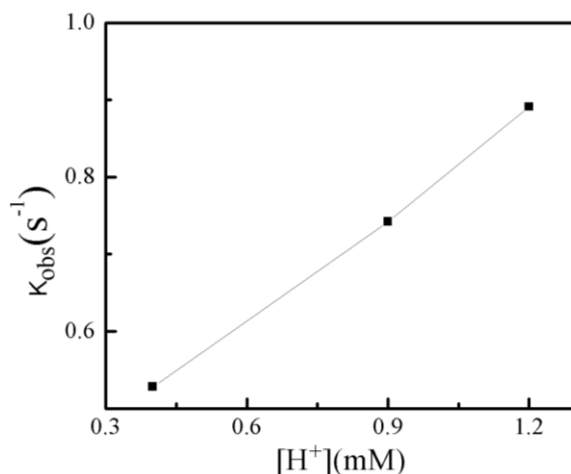


Figure 2.7. Plot of observed rate constant versus acid concentration. ($R^2 = 0.9967$)

The HER mechanism of **1** was probed through spectroscopic techniques. When two protons and two electrons are involved, several different pathways can be followed in order to generate hydrogen. The following possible sequential mechanistic steps were considered: *E-E-P-P*, *E-P-E-P*, *E-P-P-E*, *P-E-E-P*, *P-E-P-E*, and *P-P-E-E*, where *E* stands for reduction and *P* stands for protonation. In THF, **1** exhibits a narrow and intense absorbance in the typical Soret (375-425 nm) region and four small Q-bands between 470 and 650 nm. Upon titration of tosic acid, the electronic spectrum remains constant (Figure 2.8). This indicates that in THF, tosic acid is not strong enough

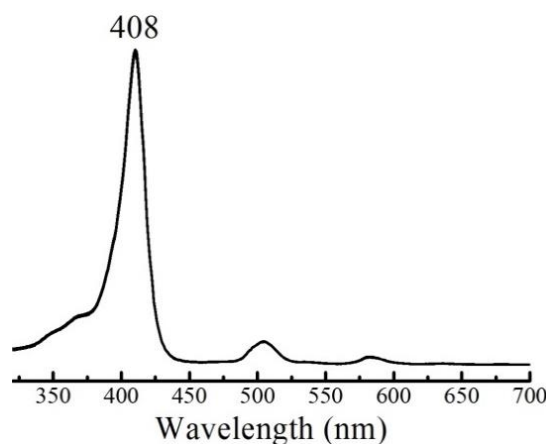


Figure 2.8. UV-Vis spectrum of **1** in THF containing 0.1 M TBAPF₆ before and after titrating with tosic acid.

to protonate **1**, suggesting that the first step of hydrogen generation is a reduction.

Figure 2.6 shows the spectral changes of **1** under different electrolysis conditions. The UV-vis spectrum of **1** upon controlled-potential bulk electrolysis at the potential of the first one-electron reduction of the porphyrin (-1.35 V vs Fc/Fc⁺), shows a decrease of the Soret (408 nm) and Q-bands (503, 530, 584, 634 nm); and the appearance of an absorption band at 436 nm along with an isosbestic point at 428 nm. This new band can be attributed to the generation of the radical anion [**1**]^{•−} (Figure 2.9a). Under the same controlled potential of -1.35 V vs Fc/Fc⁺ but in the presence of tosic acid, the band at 436 nm corresponding to the radical anion [**1**]^{•−} is also seen but the isosbestic point at 428 nm disappears as a function of time (Figure 2.9b). This implies that in addition to the generation of the radical anion [**1**]^{•−}, other chemical species are also produced. Since the only condition changed between Figure 2.9a and Figure 2.9b is the addition of acid, the second step of the catalytic cycle should be assigned to a protonation after the one-electron reduction.

When performing bulk electrolysis at the potential above the second electron reduction wave (-1.7 V vs Fc/Fc⁺) without the presence of acid, the recorded spectrum (Figure 2.9c) shows an immediate decay of the Soret absorbance coupled to an increase of a broad absorbance at 454 nm, a new band at 369 nm and another new band in the ultraviolet region (300 nm), along with an isosbestic point at 425 nm. This features the transformation from the free-base porphyrin [**1**] to the

dianion species $[1]^{2-}$. When bulk electrolysis was conducted at the same potential (-1.7 V vs Fc/Fc^+) in the presence of tosic acid, the absorbance belonging to the dianion $[1]^{2-}$ is

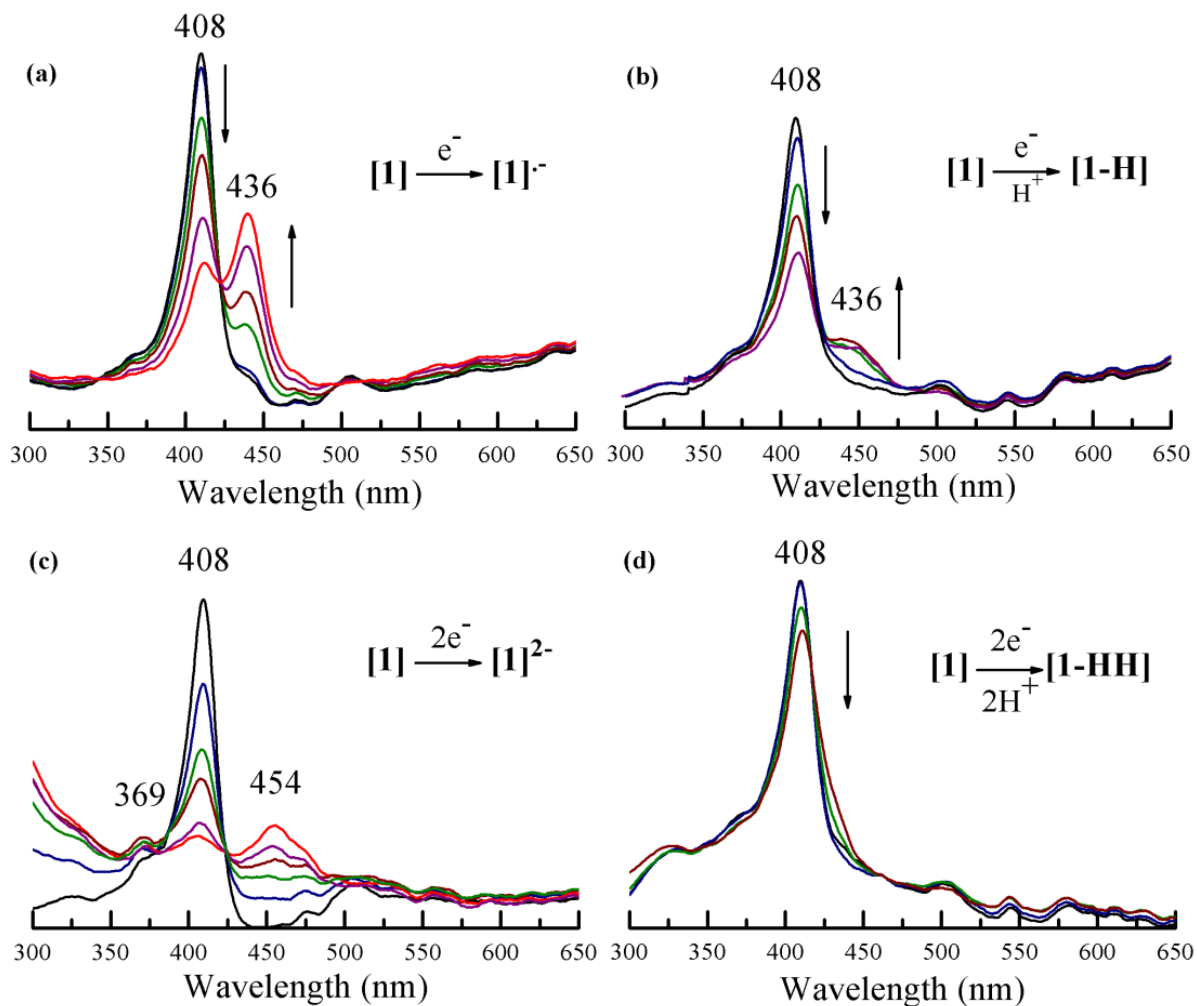


Figure 2.9. Uv-vis spectroelectrochemistry of **1** in the absence and in the presence of tosic acid containing 0.1 M TBAPF₆ in THF: (a) **1** at -1.35 V; (b) **1** containing tosic acid at -1.35 V; (c) **1** at -1.7 V; (d) **1** containing tosic acid at -1.7 V. (Potentials are referred to Fc/Fc^+ couple)

not observed and only a decrease of the Soret absorbance occurs (Figure 2.9d). However, the rate of decay of the Soret band in the presence of acid is slower compared to that without acid (Figure 2.10). This suggests that **1** is regenerated upon H₂ production. Overall these spectroscopy studies show that the first and second events of the mechanism of hydrogen generation with **1** in the presence of tosic acid are reduction and protonation, respectively.

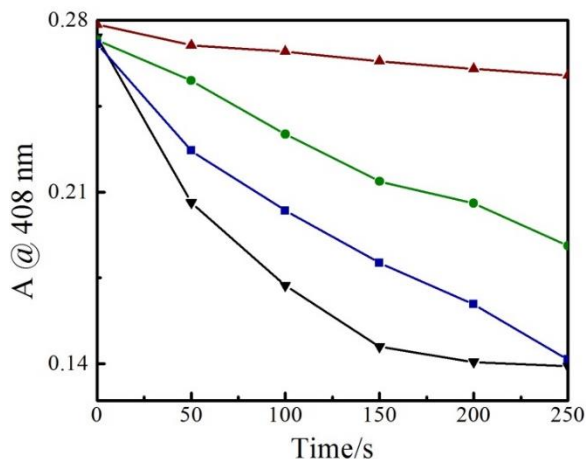
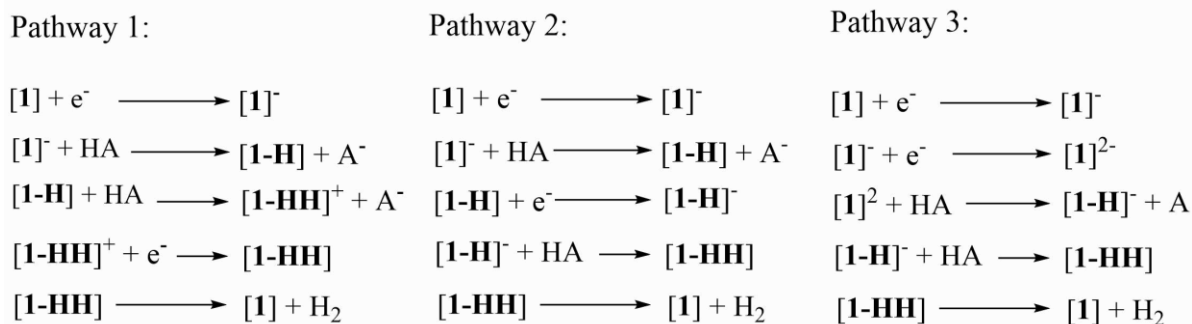


Figure 2.10. Change of absorption of **1** at 408 nm over time during electrolysis containing 1 M TBAPF₆ in THF. (From bottom to top) (▼) -1.7 V without acid; (■) -1.35 V without acid; (●) -1.35 V with tosic acid; (▲) -1.7 V with tosic acid (Potentials referred to Fc/Fc⁺).



Scheme 2.4. Mechanistic pathways proposed for hydrogen generation in THF, with tosic acid as proton source.

Thermodynamic theoretical calculations were also performed to provide further insight of the next steps of hydrogen generation. Scheme 2.4 shows the three different pathways for hydrogen

generation in THF after the first reduction, and Figure 2.11 shows the calculated relative free energies corresponding to each of these pathways. The calculated relative free energies in Figure 5 are plotted relative to the tosic acid/dihydrogen (TsOH/H₂) couple.

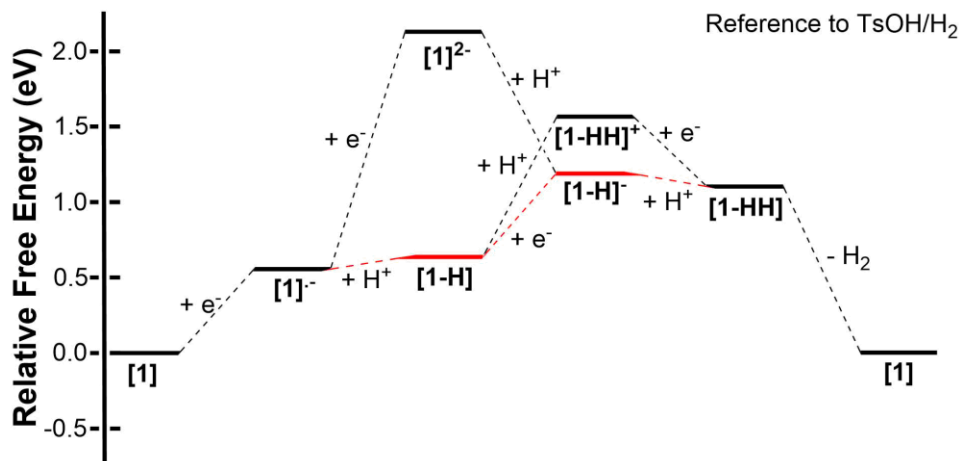
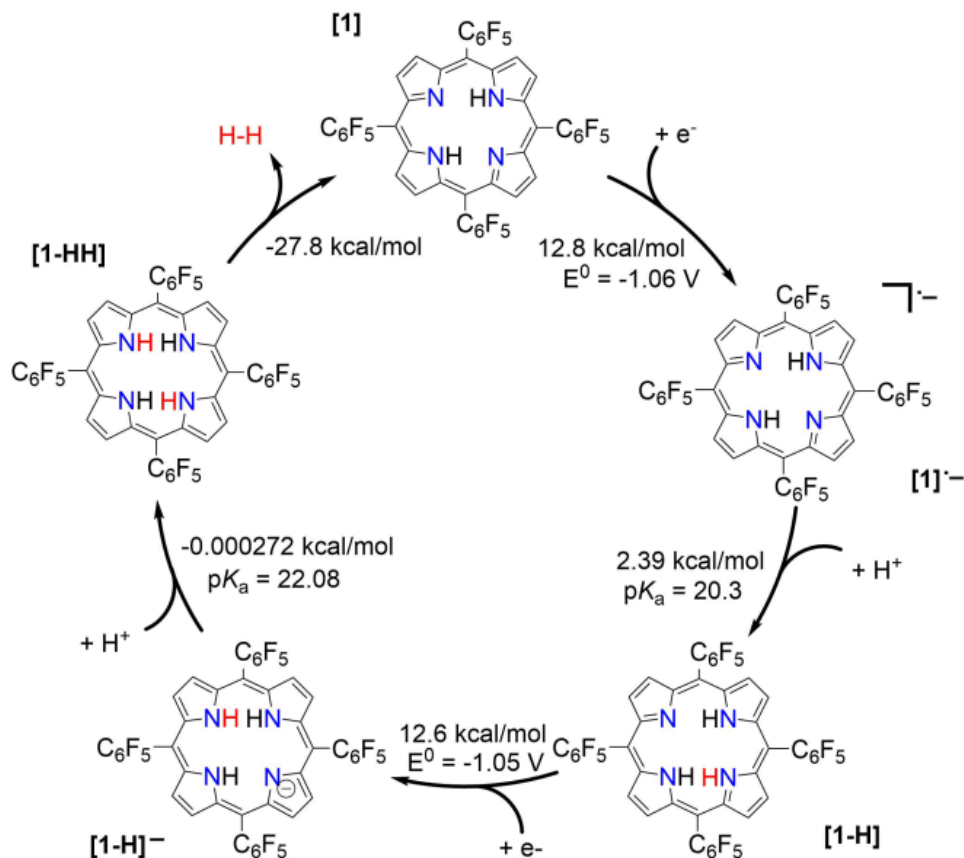


Figure 2.11. Free energy diagram of H₂ evolution catalyzed by **1** in THF with tosic acid, as calculated by the Born-Haber cycles shown in Scheme 2.2 and Scheme 2.3. The free energies are plotted relative to the tosic acid/dihydrogen (TsOH/H₂) couple.

The relative free energy difference from **[1]** to **[1]•-** is calculated to be 12.8 kcal/mol (+0.556 eV) which corresponds to a potential of -1.06 V vs Fc/Fc⁺. Upon the first reduction, **[1]•-** can follow two possible paths: it can be either further reduced to **[1]2•-** or protonated at the N core by tosic acid to yield **[1-H]**. Protonation to generate **[1-H]** is thermodynamically favored with a relative free energy of +2.39 kcal/mol (+0.104 eV), compared to going uphill +36.3 kcal/mol (+1.57 eV) to form **[1]2•-**.

The calculated relative pK_a for the deprotonation of **[1-H]** is 20.3. Since the pK_a of tosic acid in THF is predicted to be 11.8, the reduced porphyrin is likely to get protonated. The first two steps of the proposed mechanism (*E-P*) are in agreement with our experimental observations. The next step can either be electron transfer or protonation, to yield **[1-H]•-** or **[1-HH]•+**, respectively. While we cannot experimentally discern between these two pathways, **[1-H]•-** is calculated to be thermodynamically favored by 8.91 kcal/mol when compared to generating **[1-HH]•+**. The

following step yields **[1-HH]**, which putatively produces H₂, and closes the cycle. The overall proposed mechanism is described by Scheme 2.5. Calculated relative pK_as and redox potentials for all possible mechanistic pathways for H₂ generation are presented in Table 2.3.



Scheme 2.5. Proposed catalytic cycle for H₂ evolution, following an *E-P-E-P* mechanism, with THF as solvent.

Table 2.3. Calculated redox potentials and pK_a s in THF, values in parentheses correspond to the experimental values obtained in this work.

<i>Reaction</i>	<i>B3LYP</i>	<i>B3P86</i>	<i>B3LYP</i>	<i>B3P86</i>
	<i>E[•] (V vs Fc/Fc⁺)</i>		<i>pK_a</i>	
TsOH + AcO ⁻ → TsO ⁻ + AcOH			11.8	10.8
[1] + e ⁻ → [1] ^{•-}	-1.10 (-1.14) ^a	-0.95		
[1] ^{•-} + e ⁻ → [1] ²⁻	-2.12 (-1.54) ^a	-1.99		
[1-H] ⁻ + AcO ⁻ → [1] ²⁻ + AcOH			37.7	35.3
[1-HH] + AcO ⁻ → [1-H] ⁻ + AcOH			22.1	21.6
[1-H] ⁺ + AcO ⁻ → [1] + AcOH			5.9	3.5
[1-HH] ²⁺ + AcO ⁻ → [1-H] ⁺ + AcOH			-9.5	-11.1
[1-H] ⁺ + e ⁻ → [1-H]	-0.25	-0.08		
[1-HH] ²⁺ + e ⁻ → [1-HH] ⁺	0.69	0.85		
[1-HH] ⁺ + e ⁻ → [1-HH]	-0.16	0.02		
[1-H] + e ⁻ → [1-H] ⁻	-1.09	-0.99		
[1-H] + AcO ⁻ → [1] ^{•-} + AcOH			20.3	18.3
[1-HH] ⁺ + AcO ⁻ → [1-H] + AcOH			6.3	4.6

^aExperimental value

2.5 CONCLUSION

In conclusion, we have studied the electrocatalytic generation of H₂ using a metal-free perfluorinated porphyrin. The catalytic activity was studied through cyclic voltammetry and controlled-potential electrolysis. Hydrogen is produced electrochemically at -1.31 V vs Fc/Fc⁺ in THF using tosic acid at 90% Faradaic yield. Electronic spectra and spectroelectrochemical experiments combined with thermodynamic calculations using density functional theory computations suggest that the most favorable mechanistic process is an *E-P-E-P* sequence. This promising finding may contribute to open a new area for replacing noble metals by much more abundant organic compounds for the catalytic generation of hydrogen gas. It should be noted that this observed activity is limited to the meso-tetrapentafluorophenyl porphyrin with tosic acid and in THF as the solvent. We are currently working on the catalytic study of other substitution patterns (and other organic macrocycles) for the electrocatalytic production of hydrogen.

Chapter 3: Efficient Electrocatalytic Hydrogen Gas Evolution by a Cobalt-Porphyrin-based Crystalline Polymerⁱⁱ

3.1 INTRODUCTION

This chapter describes the synthesis of a crystalline extended network using cobalt porphyrin as the building unit. This polymeric network was evaluated as a heterogeneous electrocatalyst for the production of hydrogen gas in an electrochemical manner.

Metalloporphyrins as HER electrocatalysts have been widely studied and have shown promising results.^{68,73,96,143} However, they have been mainly studied as homogeneous catalysts, where there is difficulty in separating the electrocatalysts from the substrate. In addition, homogeneous metalloporphyrin electrocatalysts show poor catalytic performance owing to mass transfer issues and to the limited number of active catalytic sites exposed to the substrate and electrode.¹⁴⁴ Therefore, in order to enhance the catalytic performance of these materials, metalloporphyrin-derived heterogeneous HER electrocatalysts have been pursued by increasing the number of exposed catalytic active centers.^{97,98,144} Porphyrin-based conjugated extended networks have shown to be promising alternatives to molecular systems to yield more active and tolerant heterogeneous catalysts in many important chemical processes such as HER, carbon dioxide and oxygen reduction,^{97,98,115,144–146} among others.^{147–149} The enhanced efficiency of these systems is attributed to higher surface areas that allow for more readily available catalytically active metal sites.^{97,145}

Herein we report a crystalline polymer based on the CoTcPP unit [TcPP = the dianion of meso-tetra(4-carboxyphenyl)porphyrin)], **2**, as an effective HER electrocatalyst. We present the synthesis and characterization of **2** using standard spectroscopy and microscopy techniques. The polymer was evaluated as a heterogeneous electrocatalyst for hydrogen gas production in a standard acidic aqueous solution (0.5 M H₂SO₄ in water), using electrochemical techniques including linear sweep voltammetry, electrical impedance spectroscopy, bulk electrolysis and

ⁱⁱ This chapter is excerpted with permission from a published article: Yanyu Wu, José M. Veleta, Diya Tang, Alex D. Price, Cristian E. Botez, Dino Villagrán; Efficient Electrocatalytic Hydrogen Gas Evolution by a Cobalt-Porphyrin-based Crystalline Polymer, *Dalton Transactions*, **2018**, 47,8801-8806.

chronoamperometry. The discrete molecule CoTcPP (**3**) was also assessed heterogeneously for HER under the same conditions for comparison.

3.2 EXPERIMENTAL SECTION

Materials. All reagents were used without further purification unless otherwise stated. 4-carboxybenzaldehyde was purchased from Sigma Aldrich. $\text{Co}(\text{NO}_3)_2 \cdot 6\text{H}_2\text{O}$ and $\text{Co}(\text{OAC})_2 \cdot 4\text{H}_2\text{O}$ were purchased from Strem Chemicals. H_2SO_4 , HCl, MeOH, EtOH, and DMF were obtained from Fisher Scientific. Pyrrole was purchased from Acros Organic and was freshly distilled from calcium hydride.

Characterization. ^1H NMR spectroscopy was performed on a Bruker 400 MHz NMR spectrometer, using deuterated DMSO as the solvent and internal calibration. The UV-vis spectra were obtained using a SEC2000 spectra system equipped with a VISUAL SPECTRA 2.1 software. Fourier transform infrared (FT-IR) spectroscopy was recorded on an Agilent Cary 630 FT-IR spectrometer. X-ray diffraction (XRD) was obtained using a PANalytical Empyrean system using Cu-K α radiation ($\lambda = 1.5418 \text{ \AA}$) equipped with a PIXcel [3D] detector. Scanning electron microscope (SEM) images, elemental mapping, and energy dispersive x-ray (EDX) analysis were recorded on a Hitachi S-4800 instrument equipped with an EDX microanalysis system. Transmission electron microscopy was measured on a Hitachi H-7650 instrument.

Synthesis of meso-tetra(4-carboxyphenyl)porphyrin (H_2TcPP). Synthesis was done following a modified literature procedure.¹⁵⁰ In a 1 L round bottom flask, 4-carboxybenzaldehyde (5.00g, 33.30 mmol) was dissolved in propionic acid (500 mL) and heated at 140 °C until the mixture was completely dissolved, Then pyrrole (2.23 g, 33.30 mmol) was added dropwise and the mixture was vigorously stirred under reflux for 2 h. Afterwards, MeOH (100 mL) was added to the reaction and cooled down using an ice bath. The crude product was filtered under reduced pressure using a medium coarse filter frit. The solid residue was washed with deionized water and then dried under reduced pressure to obtain a dark purple powder. Yield: 1.65 g (25.1%). ^1H NMR

(d₆-DMSO) δ : 13.28 (s, 4H), 8.86 (s, 8H), 8.36 (m, 16H), -2.95 (s, 2H); UV-vis (EtOH): λ max: 419, 519, 552, 592, 648 nm (Figure A.5.).

Synthesis of crystalline cobalt meso-tetra(4-carboxyphenyl)porphyrin polymer (2). H₂TcPP (0.0100g, 0.0126 mmol), Co(NO₃)₂·6H₂O (0.0320g, 0.110 mmol) and 5 drops of concentrated HCl were dissolved in 3 mL DMF and 1 mL MeOH in a Pyrex vial. The mixture was sonicated for 30 minutes and then heated at 60 °C in a programmable oven for 72 h. After cooling down to room temperature, the shiny purple crystals were filtered and cleaned with copious amounts of DMF and MeOH and then dried at 50 °C. Yield: 0.0144 g. UV-vis (pH = 8 buffer in water): λ max: 427, 551 nm (Figure A.5). FT-IR (ATR, cm⁻¹) ν = 1654 (w), 1604 (sh, $\nu^s\text{COO}^-$), 1399 (s, $\nu^{\text{as}}\text{COO}^-$), 1339 (w), 1278 (w), 1174 (w), 1144 (w), 1000 (sh, Co-N), 838 (s, sh, C-H), 799 (s, sh, aromatic C-H), 771 (s, sh, C-H), 711 (s, sh, C-H). Elemental analysis: C 58.51%; H 3.69%; N 6.76%. Calcd: C 63.87%; H 2.68%; N 6.21%; O 14.18%; Co 13.06%.

Synthesis of Cobalt meso-tetra(4-carboxyphenyl)porphyrin (3). Synthesis was done following a modified literature procedure.¹⁵⁰ H₂TcPP (0.100 g, 0.126 mmol) and Co(OAc)₂·4H₂O (0.0315 g, 0.126 mmol) were dissolved in DMF (20 mL) and the solution was stirred under reflux for 1 h. The reaction mixture was then filtered and the residue was washed with deionized water. Yield: 0.0830 g (80.7%). UV-vis (EtOH): λ max: 429, 546 nm (Figure A.6). FT-IR (ATR, cm⁻¹) ν = 1720 (s, sh, C=O), 1684 (s), 1604 (sh, $\nu^s\text{COO}^-$), 1459 (w), 1406 (w, $\nu^{\text{as}}\text{COO}^-$), 1263 (s), 1244 (s), 1174 (sh), 1099 (s, sh), 1017 (sh), 1000 (sh, Co-N), 886 (w, C-H), 795 (s, sh, aromatic C-H), 765 (sh, C-H), 728 (s, sh, C-H).

Gas adsorption measurement. Nitrogen adsorption isotherms were obtained using a Micromeritics ASAP 2020 Surface Area and Porosity Analyzer. Samples were weighed and activated for 12 h at 423 K with an outgas pressure less than 100 mTorr. N₂ isotherms were measured volumetrically at 77 K, the obtained data and pressure range ($0.0001 \leq P/P_0 \leq 0.1$) were fitted into the Brunauer-Emmett-Teller (BET) equation.

Modification of FTO (fluorine-doped tin oxide)/silver working electrodes with 2 and 3. Working electrodes for electrochemical measurements were made by deposition of 2 and 3 using

silver glue on FTO glass slides. Prior to the deposition, FTO glass slides were cleaned by sonication in acetone, isopropanol and deionized water for 10 minutes separately and dried in air. Then 0.5 by 0.5 cm silver paste was coated on top of the active side of the FTO substrate. 2 mg of each catalyst was dispersed in 1 mL ethanol and sonicated for 10 minutes to generate a homogeneous ink. Then 10 μ L of the ink was dropcast on top of the silver paste and it was dried in ambient condition (loading mass: 0.08 mg/cm²).

Electrochemical measurements. Electrochemical data were obtained using a CHI760D potentiostat with a platinum mesh as the counter electrode and saturated calomel electrode (SCE) as the reference electrode in 0.5 M H₂SO₄ aqueous solutions at room temperature. Before each measurement, the solutions were purged with ultra-pure argon gas for 15 minutes to remove the dissolved oxygen. Linear sweep voltammetry experiments were conducted without stirring the solutions. All potentials displayed in the electrochemical experiments are referred to reversible hydrogen electrode (RHE) by adding a value of (0.245 + 0.059 pH) to the data obtained using a SCE reference electrode. Electrical impedance spectroscopy (EIS) was obtained at different overpotentials of 0.25, 0.30, 0.35 and 0.40 V from 100 KHz to 0.1 Hz with AC voltage of 5 mV.

Bulk electrolysis and long-term chronoamperometric measurements were performed in a custom-built two-compartment gas-tight electrochemical cell under an argon atmosphere. The two compartments are separated with a glass frit, where one part of the cell contains the Pt mesh counter electrode and the other compartment contains the working and reference electrodes. The solutions were stirred during the experiment to remove the generated hydrogen gas from the working electrode and the solvent.

Hydrogen gas determination. Hydrogen gas was determined and quantified by a gas chromatograph (GC) after performing bulk electrolysis. The instrument was calibrated by injecting 10%, 20%, 30% and 40% of ultra-pure hydrogen gas in the GC instrument separately and the concentrations of hydrogen gas are assumed to be proportional to the peak areas. A calibration curve with the correlation of hydrogen gas concentration and peak areas was constructed. Using a gas tight syringe, 50 μ L of the gas in the headspace (90 mL) from the cathode side in the two-

compartment electrochemical cell was injected to the GC. The percentage of hydrogen gas in the headspace was determined according to the peak area. The theoretical amount of H₂ was determined by dividing the passed charge (Q) by 2F (F = 96485). The Faradaic efficiency is calculated according to the following equation:¹⁵¹

$$\text{Faradaic efficiency (\%)} = [96485 * 2 * \text{mol H}_2(\text{GC}) * 100\%] / Q$$

3.3 RESULTS AND DISCUSSION

Figure 3.1 shows the p-XRD pattern of **2**, revealing its crystallinity by showing a strong and well-defined diffraction peak at $2\theta = 7.47^\circ$ and several other weaker diffraction peaks at $2\theta = 12.80^\circ$, 15.78° , 18.32° and 20.54° , 23.14° and 30.31° respectively. While the diffraction quality of this polymer is not comparable to that of analogous metal-organic frameworks (MOFs),^{143,152,153} clear and well-defined peaks can be observed.

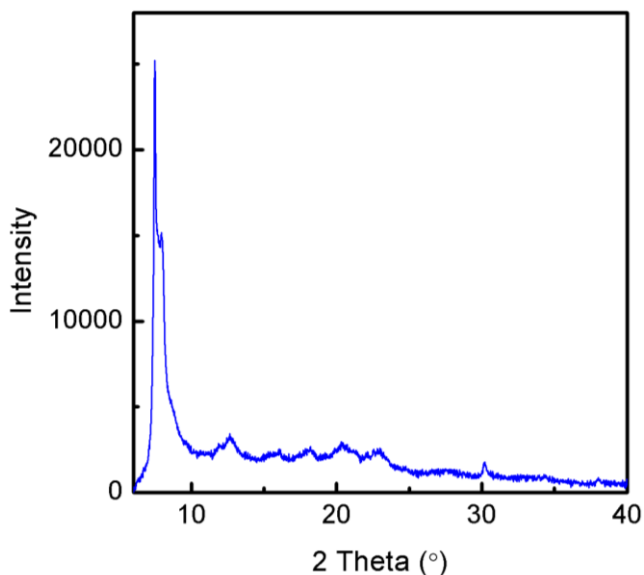


Figure 3.1. p-XRD pattern of **2**.

Transmission electron microscope (TEM) images (Figures 3.2a-b) of **2** indicate that this material is composed of thin films. Scanning electron microscope (SEM) images of **2** (Figure 3.2c-d) shows its irregular cube-like morphology at lower amplifications. The respective elemental mapping images (Figures 3.2e-g), show the elemental composition of Co, C and O in **2**, which indicate the presence of cobalt centers into the porphyrin crystalline polymer. The presence of Co, C and O in the sample is also confirmed by EDX spectra (Figure 3.3).

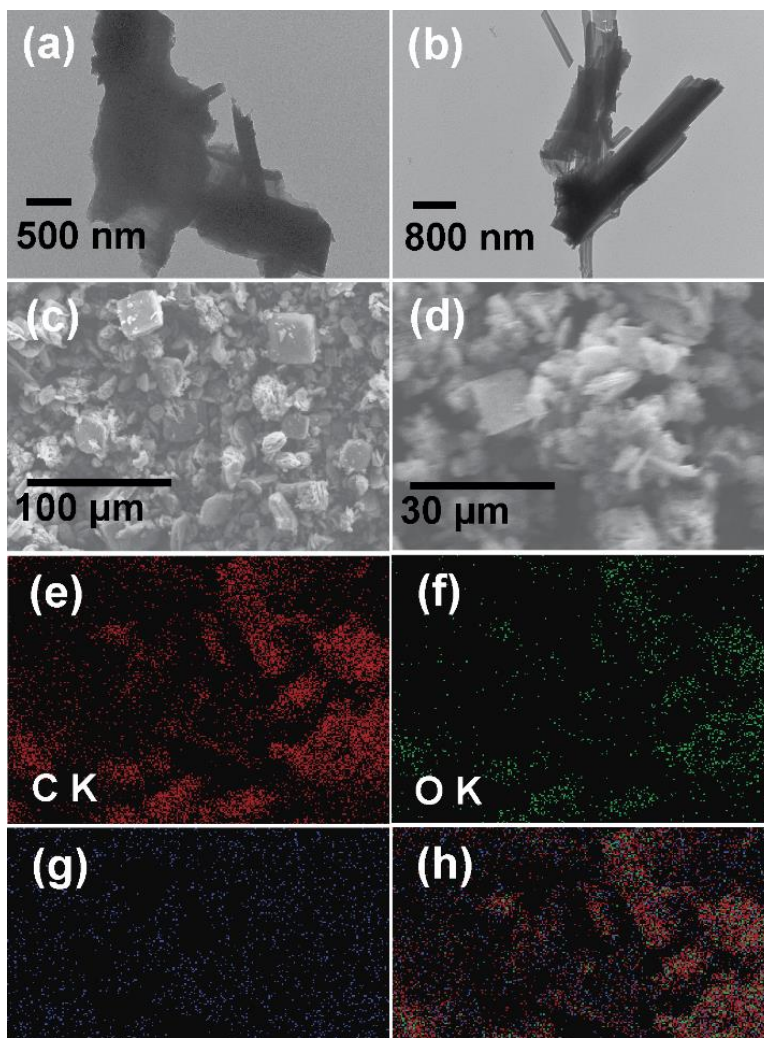


Figure 3.2. (a, b) TEM images of **2**; (c, d) SEM graphs of **2**; (e, g) the corresponding elemental maps of C, O and Co respectively based on d and (h) overlay elemental mapping image of Co, C and O.

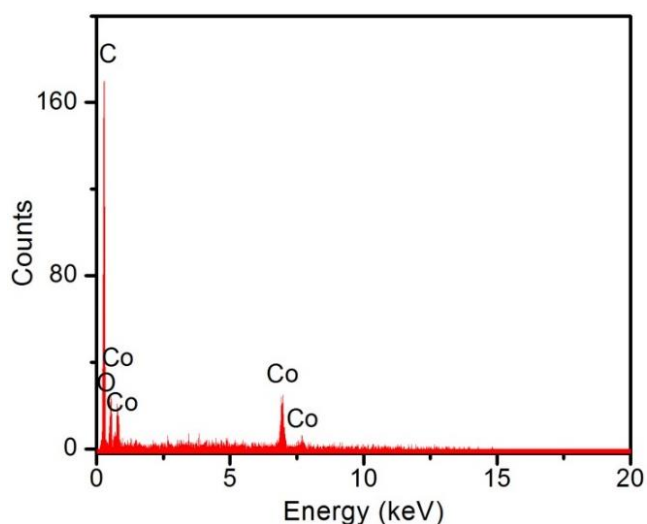


Figure 3.3. EDX spectrum of **2**.

Quantification of the elemental composition of **2** from EDX analysis shows Co, C, N and O contents of 12.38%, 64.97%, 6.84% and 15.81%, respectively. These results deviate from the theoretical values by around 1%, which are small with respect to polymeric systems which typically present much larger deviations.^{154–156} Elemental analysis results also show reasonable agreements with respect to theoretical values albeit with larger errors compared to EDX. This is due to the difficulty of the complete combustion of polymers systems and presence of unidentified absorbed gases and solvent in the pores, which have been observed in similar systems.^{155,156}

N₂ sorption measurement through Brunauer-Emmett-Teller (BET) measurements shows a surface area of **2** of 441.74 m²/g (see Figure 3.4). In comparison, the CoTcPP monomer, **3**, shows a significantly smaller surface area of 3.44 m²/g. Thus, the extended network of the crystalline porphyrin polymer, **2**, effectively increases the porosity and surface area of the material, which presumably allows for more exposed active catalytic sites.

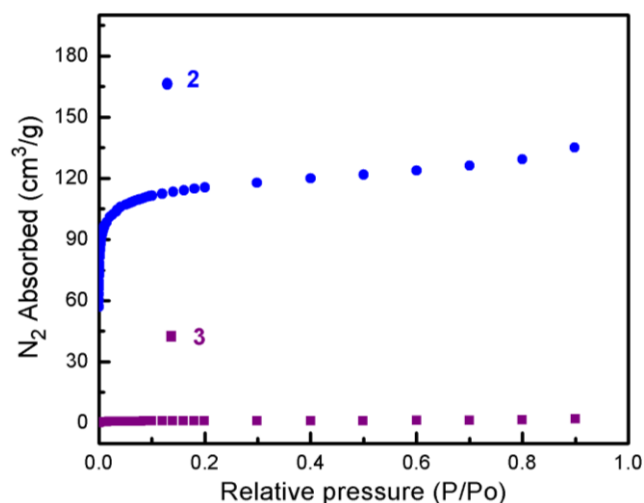


Figure 3.4. N₂ sorption isotherms at 77 K of **2** and **3**.

The redox activity of the crystalline Co porphyrin-based polymer (**2**) and Co porphyrin monomer (**3**) was studied by cyclic voltammetry in the presence of a pH = 4.56 buffer solution, which can be seen in Figure 3.5. Polymer **2** and monomer **3** exhibit a reduction event starting at the potential of -0.096 and -0.181 V vs. SCE, respectively. And **2** shows a larger peak current compared to **3**. This result shows that addition of Co to the CoTcPP system help to tune the reduction potential to more anodic value.

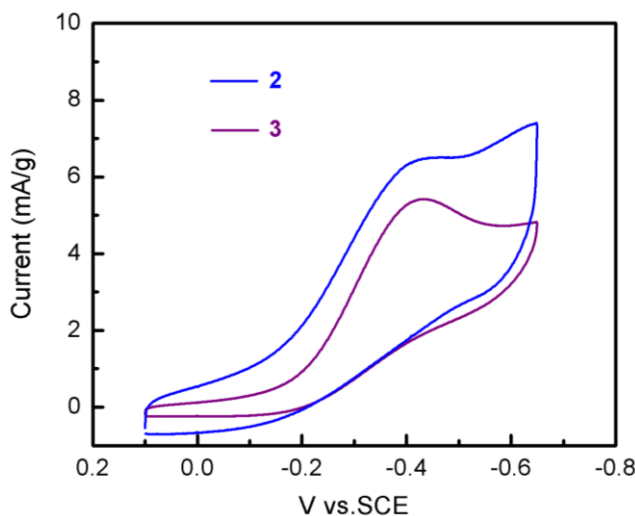


Figure 3.5. Cyclic voltammograms of **2** and **3** modified silver/FTO working electrodes in the presence of pH = 4.56 buffer solution. Scan rate: 50 mV/s.

Linear sweep voltammetry was used to assess the HER electrocatalytic properties of **2** and **3**. Both catalysts were evaluated heterogeneously in 0.5 M H₂SO₄ aqueous solution with a scan rate of 2 mV/s. Figure 3.6a depicts the polarization curves which display the cathodic current as a function of applied potential. As reference, a Pt working electrode (2 mm diameter) and a catalyst-free FTO/silver substrate working electrode were also tested under the same condition. The Pt working electrode exhibits a large cathodic current increase at zero onset overpotential (η) while the FTO/silver working electrode generates a negligible current increase at the potential range displayed (0 ~ -0.7 V vs. RHE). To study the HER electrocatalytic efficiency, the overpotential (η) was measured at the chosen current density, j , of 10 mA/cm². Electrocatalysts **2** and **3** require an η of 0.475 and 0.666 V, respectively, indicating that the polymeric system exhibits enhanced HER catalytic efficiency by requiring less overpotential when compared to the discrete molecule. This can be explained by the larger surface area that allows more available exposed active sites of the polymer compared to the molecule.

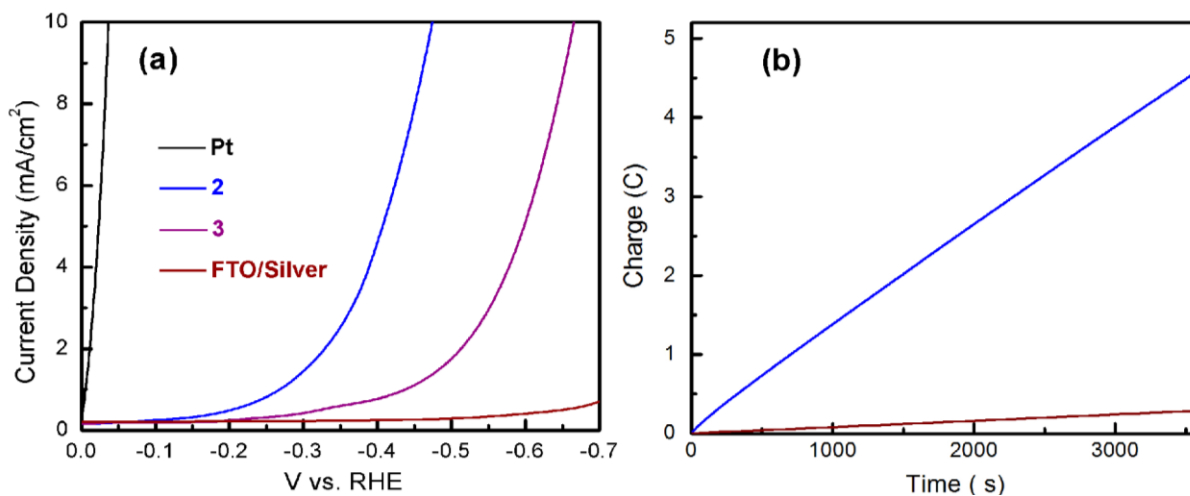


Figure 3.6. (a) Polarization curves of Pt (black); **2** (blue); **3** (purple); and catalyst-free FTO/Silver (burgundy) in 0.5 M H₂SO₄ electrolyte solution; Scan rate: 2mV/s; (b) Bulk electrolysis measurement of **2** (blue) and catalyst-free FTO/Silver (burgundy) in 0.5 M H₂SO₄ electrolyte solution.

The amount of H₂ gas evolved was quantified using a gas chromatograph (GC) after performing bulk electrolysis for 1 h. Figure 3.6b presents the passed charge after 1 h's constant electrolysis. The amount of generated H₂ is consistent with the theoretical production based on Faraday's law, assuming all the charges were accounted for the 2 e⁻ reduction of proton to generate H₂, implying a quantitative faradaic yield.

Electrical impedance spectroscopy (EIS) was conducted to understand the conductivity of the polymeric network. The Nyquist plots of **2** at different η of 0.25, 0.30, 0.35 and 0.40 V, with frequencies ranging from 100 KHz to 0.1 Hz are presented in Figure 3.7a. The plots show that **2** exhibits good conductivity with relatively small diameters of semicycles. As η increases, the diameters decrease gradually, implying faster HER kinetics at higher η .

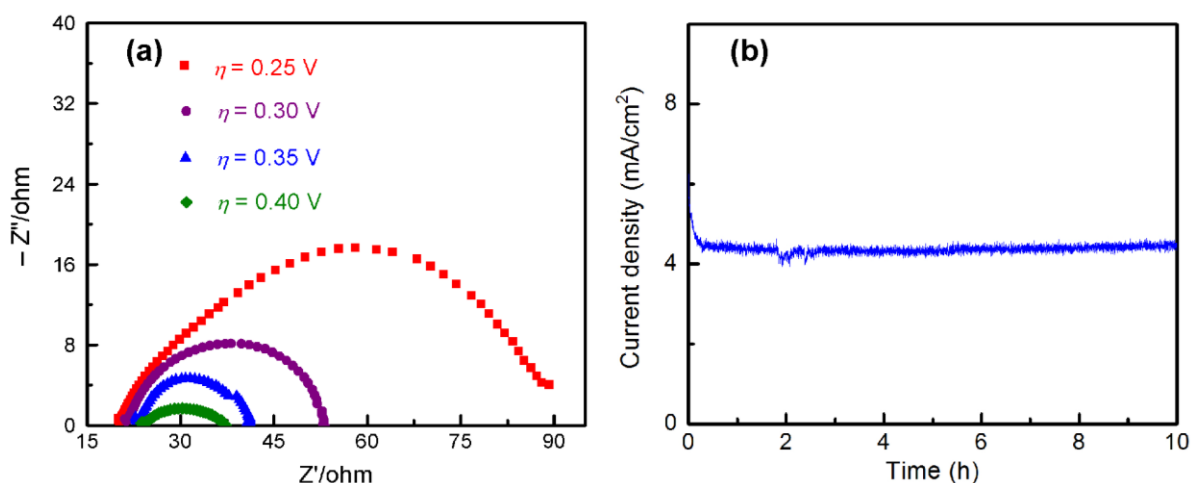


Figure 3.7. (a) Nyquist plots of the as-prepared **2**/ Silver/FTO electrode at (from top to bottom): $\eta = 0.25, 0.30, 0.35$ and 0.40 V; (b) Chronoamperometric responses ($j \sim t$) of **1** in 0.5 M H₂SO₄ aqueous solution for 10 h. (Applied potential: -0.4 vs. RHE)

To evaluate the durability of the polymer as HER electrocatalyst, long-term chronoamperometric measurement was conducted using the **2**-modified FTO/silver working electrode. Figure 3.7b exhibits the corresponding current density at a controlled potential of -0.4 V vs. RHE in 0.5 M H₂SO₄ aqueous solution for 10 h. It can be seen that the catalyst presents excellent catalytic stability under 10 h electrocatalysis with almost no current density decrease.

Linear sweep voltammetry using the rinsed catalyst-modified working electrode with the attached catalyst used after 10 h electrolysis in an acid solution of 0.5 M H₂SO₄ (Figure 3.8) shows an overpotential increase of ca. 5 mV at 10 mA/cm² which implies minimum catalyst leeching over

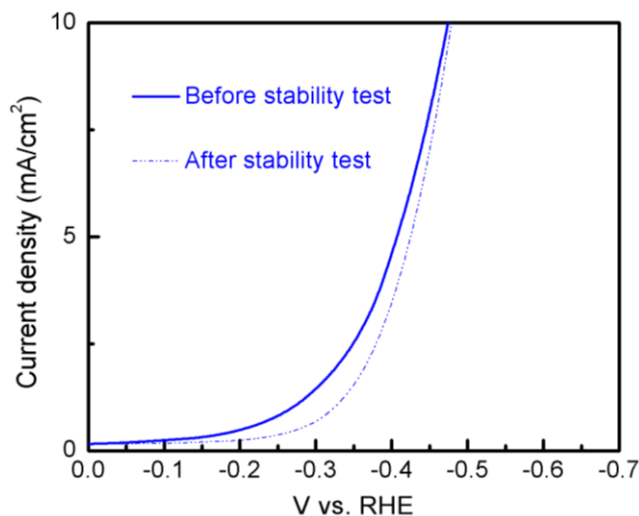


Figure 3.8. Polarization curves of **2** before (solid line) and after (dotted line) 10 h' constant chronoamperometry analysis at -0.4 V vs. RHE.

long term electrolysis.

The reaction kinetics of both **2** and **3** as HER electrocatalysts were probed through Tafel plot analysis, where the relationship between η and $\log(j)$ is depicted. The Tafel plots of **2** and **3** are presented in Figure 3.9. By fitting the plots into the Tafel equation: $\eta = b * \log(j) + a$ (where b is the Tafel slope and a is a constant), Tafel slopes for **2** and **3** are obtained, which are 197 and 264 mV/dec, respectively. Since slower Tafel slopes correspond to faster kinetics, this result indicates that **2** is a better electrocatalyst than **3**.

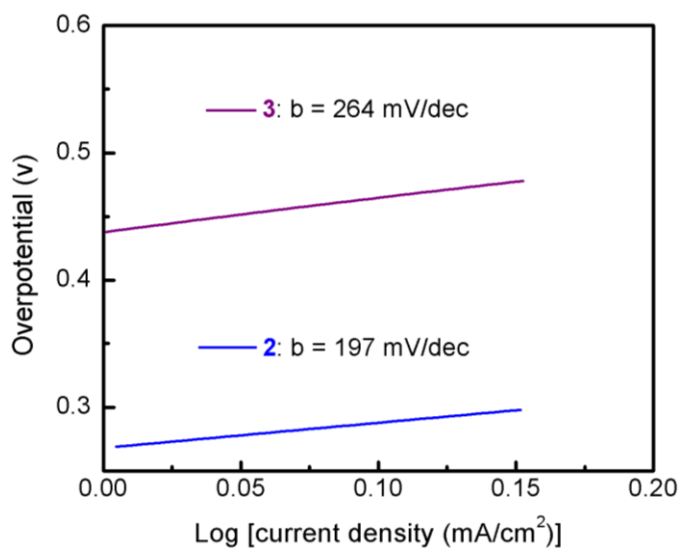


Figure 3.9. Tafel plots of **2** and **3**.

3.4 CONCLUSION

In this chapter we have compared a crystalline cobalt porphyrin-based polymer and a cobalt porphyrin monomer for electrocatalytic hydrogen gas generation in strong acidic media. The polymer shows significantly larger surface area and enhanced catalytic performance compared to the discrete molecule. This gives strong evidence that the construction of a polymeric system based on HER electrocatalytic active molecular catalysts can enhance the catalytic efficiency.

Chapter 4. Metalloporphyrin organic polymers as effective and stable electrocatalysts for the oxygen evolution reaction

4.1 INTRODUCTION

We describe in this chapter the fabrication of several polymeric networks based on metalloporphyrin building units as heterogeneous electrocatalysts for the oxygen evolution reaction in basic solution.

Metalloporphyrin conjugated polymers are a novel group of π -conjugated extended networks. This type of materials have shown potential in a wide range of catalysis applications owing to their advantageous properties, including, but not limited to, facile catalysts/reactants separation, rational architectural design of the molecular units, enhanced thermal and chemical stabilities.^{97,115,145,147,148,157} Of particular interest are metalloporphyrins based polymeric systems that have shown to be promising alternatives as effective and stable heterogeneous electrocatalysts for HER and OER.^{98,115} Most reported metalloporphyrin polymers are obtained from cross coupling reactions based upon the respective metalloporphyrin monomer units. This work reports the synthesis and characterizations of an easily synthesized porphyrin organic polymer from one-step polymerization, and its metallated versions based on cobalt and iron as OER electrocatalysts. All materials were characterized using standard spectroscopic and microscopic techniques. Inductively coupled plasma mass spectrometry (ICP-MS) was utilized to determine the metal loading of the cobalt and iron porphyrin polymers. We also report herein the evaluation of the electrocatalytic OER performances of all polymer materials through electrochemical studies.

4.2 EXPERIMENTAL SECTION

Materials. All chemicals used were purchased from commercially available sources. Pyrrole (C_4H_5N), terephthalaldehyde ($C_8H_6O_2$), 2,3,5,6-tetrafluoroterephthalaldehyde, $FeCl_2 \cdot 4H_2O$, and Nafion[®]117 (5%) were purchased from Sigma Aldrich. $Co(OAC)_2 \cdot 4H_2O$ was purchased from TCI chemicals. Carbon black (Vulcan XC-72) was obtained from Fuel Cell Store. All solvents used and potassium hydroxide (KOH) pellets were from Fisher Scientific. Pyrrole was freshly distilled prior to use while other chemicals were used as received.

Physical and Chemical characterization. Fourier-transform infrared (FT-IR) spectra were recorded using an Agilent Cary 630 FT-IR spectrometer equipped with an attenuated total reflectance (ATR) accessory. X-ray diffraction powder (XRPD) patterns were obtained using a Bruker D8 Discovery x-ray diffractometer. Scanning electron microscope (SEM) measurement along with elemental mapping and energy dispersive x-ray analysis (EDX) were recorded on a Hitachi S-4800 instrument equipped with an EDX microanalysis system. X-ray photoelectron spectroscopy (XPS) spectra were obtained by a Physical Electronics PHI 5000 VersaProbe with an Al K α source. All spectra were calibrated to the adventitious carbon 1s peak at 284.8 eV and fitted using a Shirley background. ICP-MS measurements were performed by a Thermoscientific Thermo XSeries II by firstly digesting the samples in an aqua regia matrix overnight and then filtered and diluted to 5% acid (v/v%).

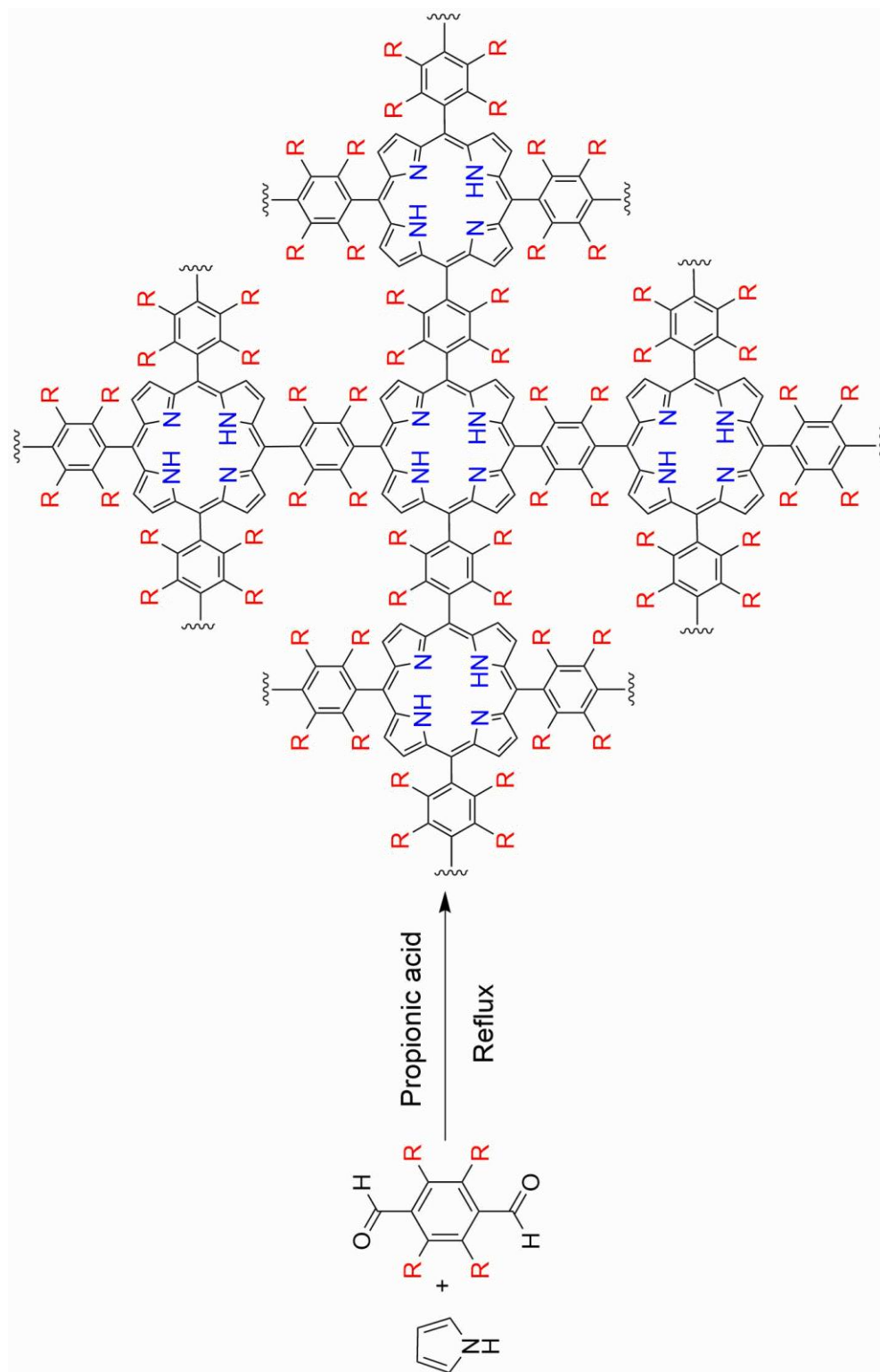
Working electrode preparation. A catalyst ink was prepared by dispersing 2.5 mg of carbon black and 5 mg of each sample in 1.02 mL isopropanol and 4.08 μ L Nafion solution. The resulting solution was sonicated for 30 minutes to form a homogeneous ink. A glassy carbon disk was cleaned by sonication in isopropyl alcohol, acetone, and deionized water separately, and polished to a mirror finish prior to be mounted on a rotating disk electrode (RDE) apparatus. The working electrode consisted of 10 μ L of the prepared catalyst dropcasted on a glassy carbon disk which was rotated at 600 RPM for 5 minutes until the ink was dry. The glassy carbon disk electrode (0.196 cm²) had a final catalyst loading of 0.25 mg/cm².

Electrochemical measurements. Electrochemical measurements were conducted in a three-electrode RDE configuration using an Ag/AgCl reference electrode, a Pt wire counter electrode and the modified glassy carbon disk as the working electrode. All studies were carried out in a 0.1 M KOH aqueous solution saturated with ultra-high purity O₂ with the working electrode constantly rotated at 1600 RPM at a scan rate of 10 mV/s. Ohmic correction was performed after each electrochemical measurement and the resistance of the electrolyte solution in the cell was determined at 100 kHz. The RHE (reversible hydrogen electrode) potential was

determined by measuring the open-circuit potential of a clean Pt electrode in the electrolyte solution after testing the electrodes.

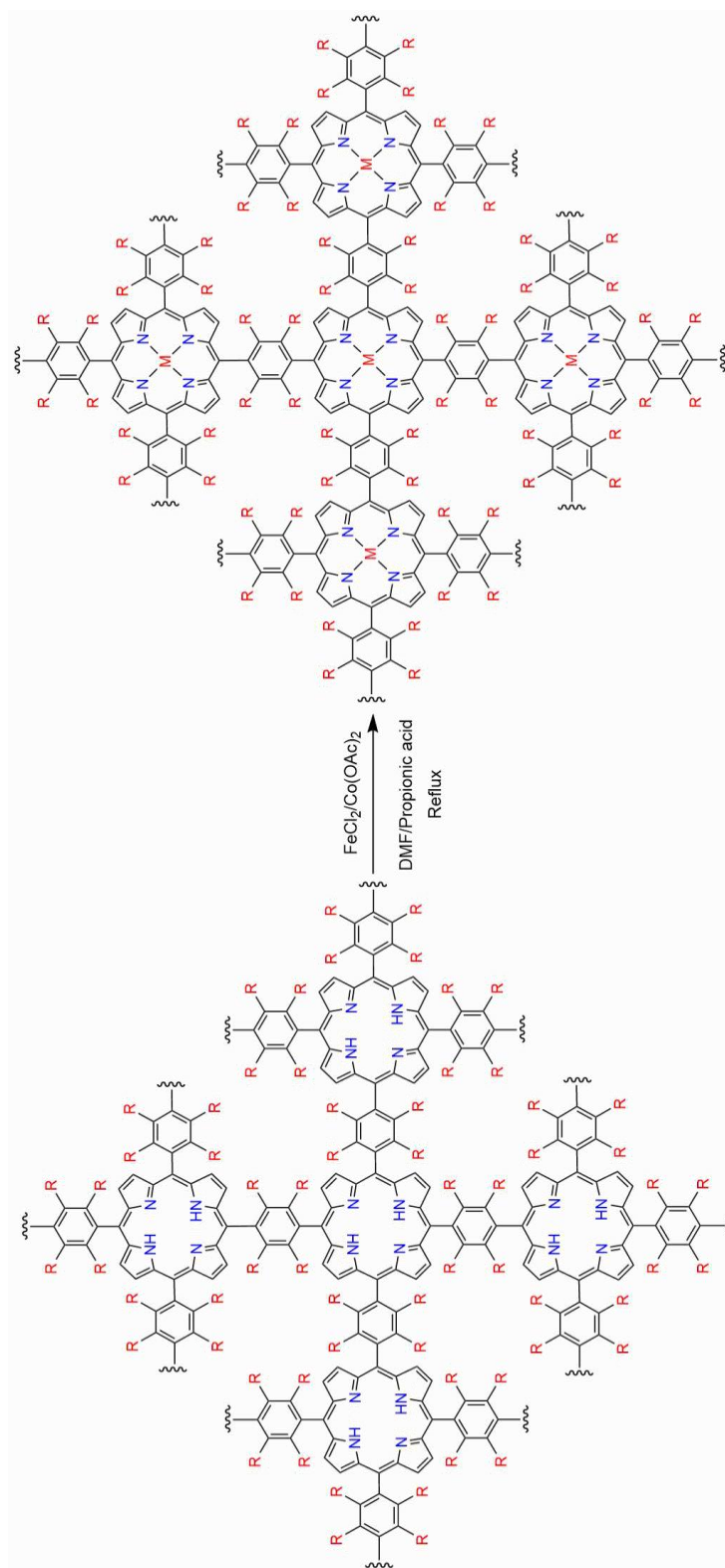
Synthesis of porphyrin organic polymer [(Por)OP] and F(Por)OP:¹⁴⁸ The general synthetic scheme is shown in Scheme 4.1. Terephthalaldehyde (0.500 g, 3.73 mmol) or 2,3,5,6-tetrafluoroterephthalaldehyde (0.768 g, 3.73 mmol) was dissolved in propionic acid (400 mL) while freshly distilled pyrrole (0.250 g, 3.73 mmol) was dissolved in propionic acid (40 mL). The pyrrole solution was slowly added to the terephthalaldehyde solution with constant stirring. The reaction mixture was allowed to react under reflux conditions for 12 h. The resultant product was cooled down and filtered using a medium coarse filter frit and was washed thoroughly with (1) deionized water, (2) methanol, (3) tetrahydrofuran and finally (4) dichloromethane. The filtered and washed product was vacuum dried at 80 °C to remove any residual solvents to obtain the final products as black powder. [Yield: F(Por)OP: 0.705 g, 79.40%; (Por)OP: 0.459 g, 74.10%]

Synthesis of cobalt porphyrin organic polymers [Co(Por)OP and CoF(Por)OP] and iron porphyrin organic polymers [Fe(Por)OP and FeF(Por)OP] :¹⁴⁸ The general synthetic scheme is shown in Scheme 4.2. In separate syntheses, (Por)OP or F(Por)OP (0.325 g) and the corresponding metal salts [Co(OAc)₂·4H₂O and FeCl₂·4H₂O] (1.10 g) were dissolved in a mixture solvent of propionic acid and DMF (400 mL, v/v = 2:1). The reaction mixtures were heated under reflux with constant stirring for 3 days. The solutions were subsequently cooled down and filtered using a medium coarse filter frit. The black filter cake was washed with deionized water, methanol and dimethylformamide and vacuum dried at 80 °C to remove any residual solvents.



Scheme 4.1. Synthetic scheme of porphyrin organic polymers.ⁱⁱⁱ

ⁱⁱⁱ $R = H$ or F



Scheme 4.2. Synthetic scheme of metalloporphyrin organic polymers.^{iv}

^{iv} R = H or F, M = Co or Fe

4.3 RESULTS AND DISCUSSION

FT-IR spectra and XRPD of all the synthesized samples are shown in Figure 4.1 and Figure 4.2, respectively. Notably, all FT-IR spectra do not show the characteristic C=O vibration band of the aldehyde between 1720 and 1740 cm^{-1} , which is expected to diminish after successful polymerization; therefore, indicating that all samples are polymeric systems. The band observed at around 1001 cm^{-1} in Co(Por)OP and Fe(Por)OP is assigned to the characteristic metal-nitrogen vibration suggesting successful metallation. The peaks observed at around 1298 cm^{-1} in the fluorinated samples are attributed to the C-F stretch. XRPD diffractograms of all the samples show no strong diffraction peaks (Figure 4.2), which reveal the amorphous nature of the synthesized materials and are consistent with previous reported studies.¹⁴⁸

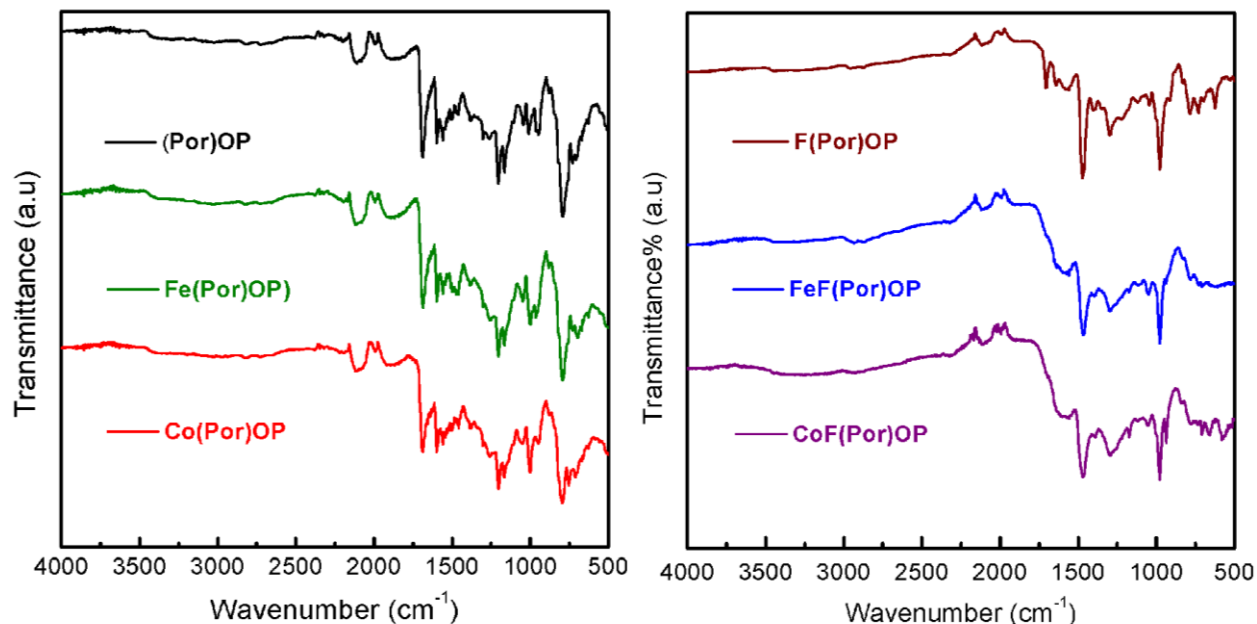


Figure 4.1. FT-IR spectra of (Por)OP, F(Por)OP, Co(Por)OP, CoF(Por)OP, Fe(Por)OP and FeF(Por)OP.

SEM micrographs of (Por)OP and F(Por)OP are shown in Figure 4.3a and Figure 4.3b, respectively, indicating that both materials present morphologies of uniform spherical particles with dimensions at the micrometer scale. After metallation, the morphologies of the polymers do not show any significant alterations, as the SEM images of all of the metalloporphyrin polymers

show that they are also spherical particles, which are presented in Figures 4.3c-f. These results are in agreement with previous studies.¹⁴⁸

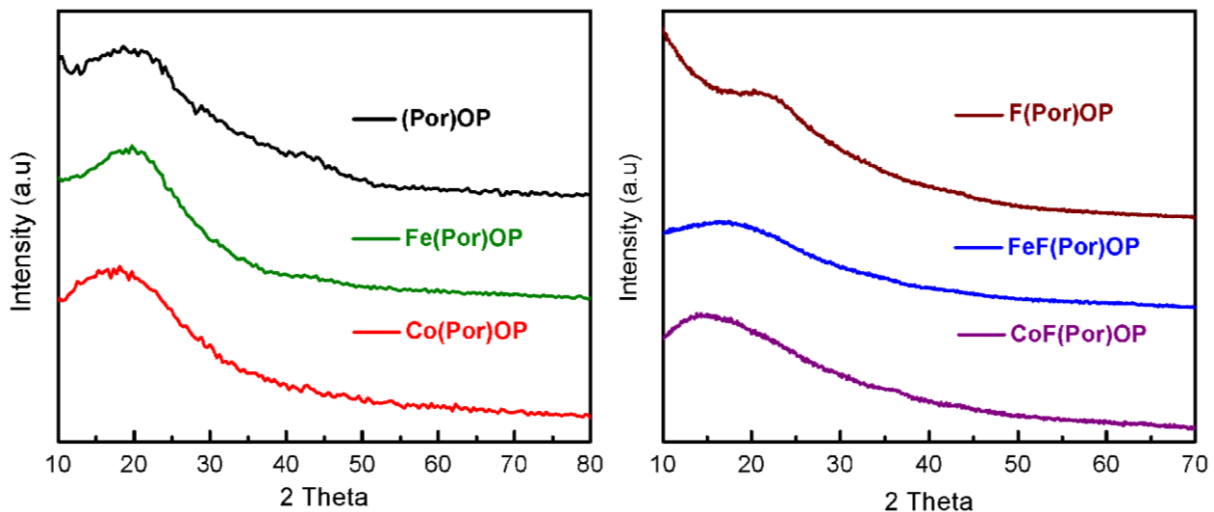


Figure 4.2. XRPD patterns of (Por)OP, F(Por)OP, Co(Por)OP, CoF(Por)OP, Fe(Por)OP and FeF(Por)OP.

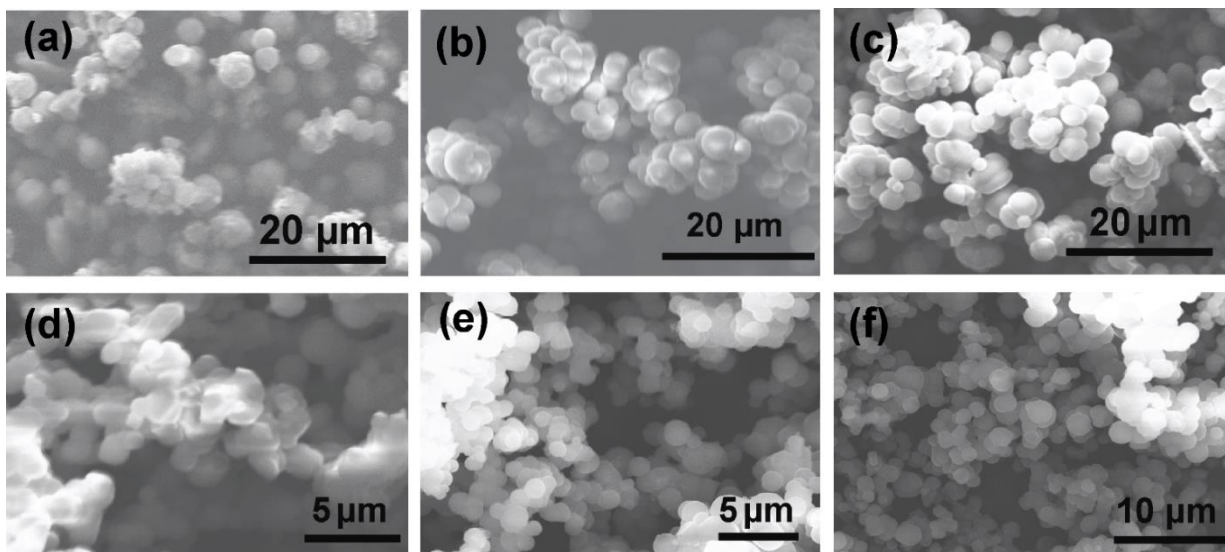


Figure 4.3. SEM images of (a) (Por)OP, (b) Co(Por)OP, (c) Fe(Por)OP, (d) F(Por)OP, (e) CoF(Por)OP and (f) FeF(Por)OP.

To corroborate the successful addition of cobalt in Co(Por)OP and CoF(Por)OP, and iron in Fe(Por)OP and FeF(Por)OP, energy dispersive x-ray (EDX) analysis was performed on all of the synthesized samples through SEM to analyze their elemental composition. The EDX spectra of (Por)OP and F(Por)OP are displayed in Figure 4.4a and Figure 4.4b respectively, showing the presence of carbon and oxygen in (Por)OP and carbon, oxygen and fluorine in F(Por)OP. Figure 4.4c and Figure 4.4d both confirm the presence of cobalt in samples Co(Por)OP and CoF(Por)OP in addition to the elements found in their respective unmetallated porphyrin polymers, while the EDX spectra of both Fe(Por)OP and FeF(Por)OP indicate the existence of iron (Figure 4.4e and Figure 4.4f). These EDX results show effective metallation in all of the metallated polymer samples. The metal content was determined by inductively coupled plasma mass spectrometry (ICP-MS). As a result, Co(Por)OP and CoF(Por)OP contains 17.13% and 54.12% cobalt, respectively, while Fe(Por)OP and FeF(Por)OP respectively show iron content of 4.19% and 34.64% .

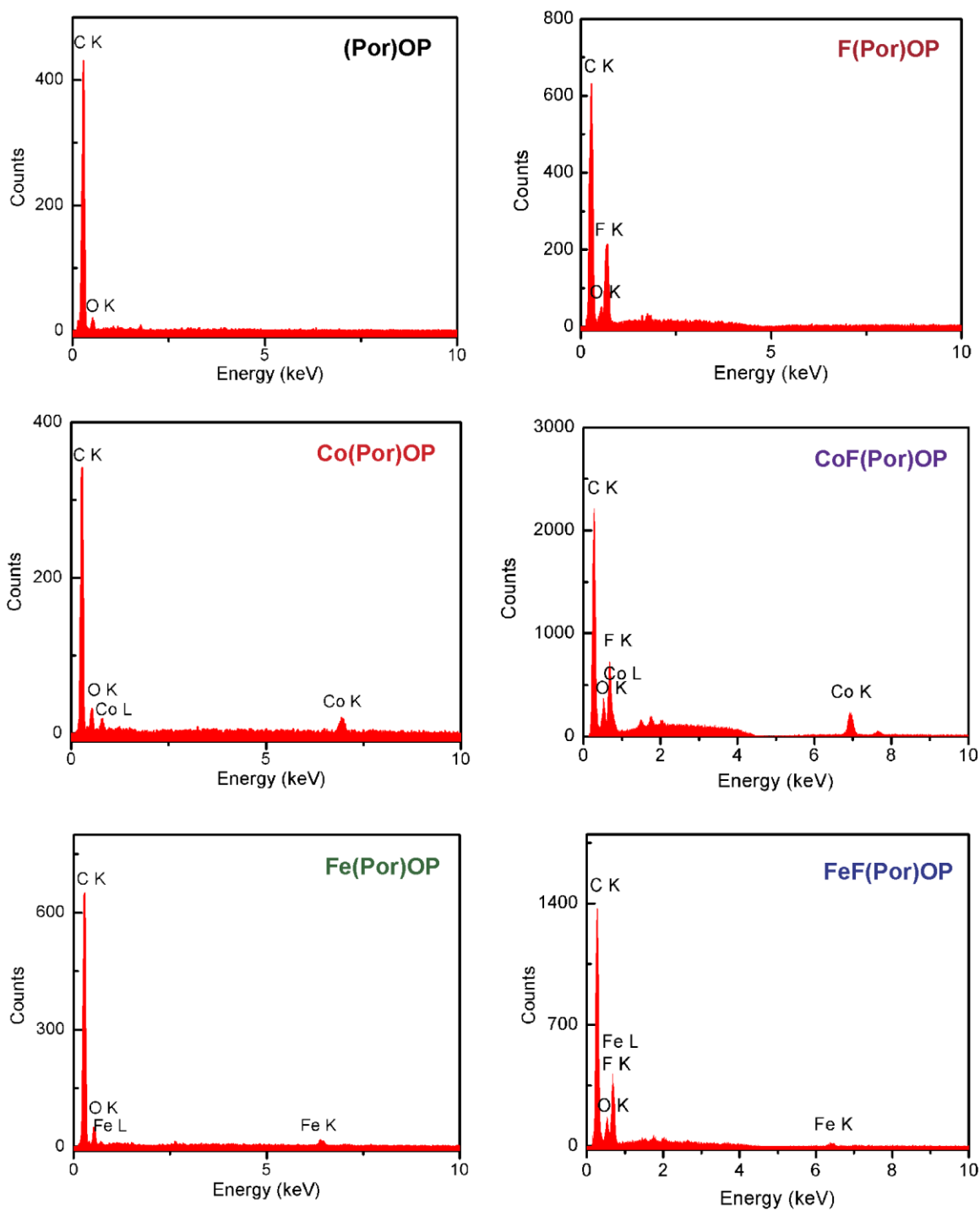


Figure 4.4. EDX spectra of (Por)OP, F(Por)OP, Co(Por)OP, CoF(Por)OP, Fe(Por)OP and FeF(Por)OP.

Figure 4.5 shows the polarization curves of all the synthesized polymers and pure carbon black, which was used in the preparation of catalysts on the working electrodes to enhance the conductivity. All of the metallated species show to be electrocatalytic active with modest overpotentials (η) for oxygen production. At the chosen current density (j) of 10 mA/cm², η is 0.38 and 0.43 V for CoF(Por)OP and Co(Por)OP, respectively, while η is 0.46 V for both Fe(Por)OP and FeF(Por)OP. These electrochemical results are comparable to other reported porphyrin polymeric OER electrocatalysts.⁹⁷ On the contrary, both of the metal-free polymers (Por)OP and F(Por)OP show no significant catalytic current increase, implying that the metal centers are the essential catalytic active sites. Additionally, the carbon black also shows no electrocatalytic activity.

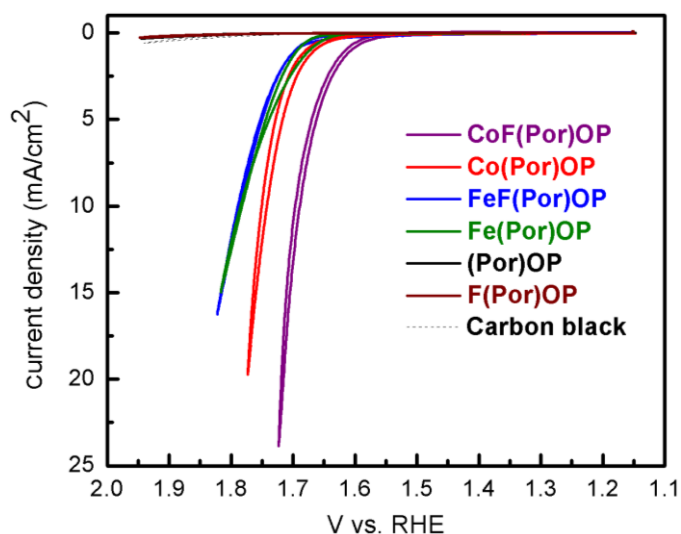


Figure 4.5. Cyclic voltammograms of (Por)OP, F(Por)OP, Co(Por)OP, CoF(Por)OP, Fe(Por)OP, FeF(Por)OP and carbon black with iR compensation in the presence of 0.1 M KOH electrolyte solutions saturated with oxygen gas; Scan rate: 10 mV/s.

To further study the OER kinetics, Tafel analysis of CoF(Por)OP, Co(Por)OP, FeF(Por)OP and Fe(Por)OP were obtained. Figure 4.6 shows the Tafel plots fitted to the Tafel equation ($\eta = b \log j + a$, where b is the Tafel slope and a is a constant) to obtain the Tafel slope. The Tafel slopes of CoF(Por)OP, Co(Por)OP, FeF(Por)OP and Fe(Por)OP are determined to be 84.2, 72.8, 89.8 and 91.7 mV/dec respectively, which are comparable to or better than previous reported similar

porphyrin polymer-based catalytic systems. These results further indicate that both metalloporphyrin polymeric materials are efficient and promising OER electrocatalysts.

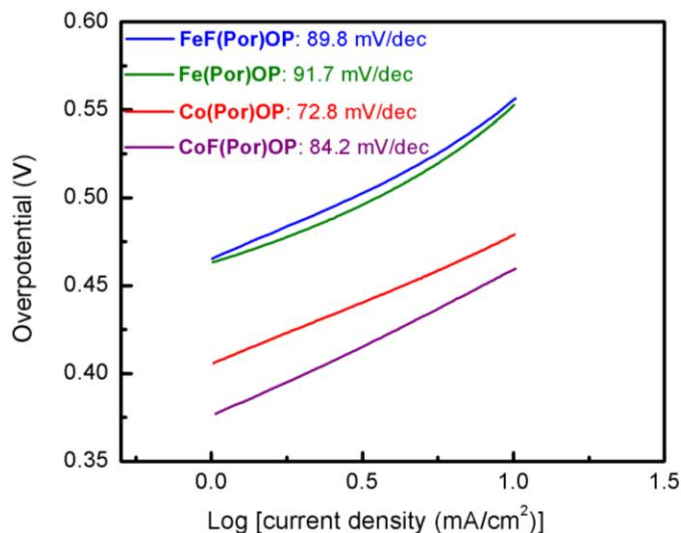


Figure 4.6. Tafel plots of Co(Por)OP, CoF(Por)OP, Fe(Por)OP and FeF(Por)OP in 0.1 M KOH.

4.4 CONCLUSIONS

In conclusion, we have successfully synthesized and characterized a porphyrin organic polymer and its fluorinated version, which were obtained from a facile one-step condensation reaction of pyrrole and the respective aldehyde in the presence of propionic acid. Both polymers were implemented as substrates for direct metallation using cobalt and iron to prepare four different metalloporphyrin organic polymers. These materials were used for oxygen evolution from alkaline aqueous media through electrochemical means. All of the metallated porphyrin polymers exhibit to be efficient OER electrocatalysts by requiring moderate overpotentials while the metal-free polymers are catalytically inert under the same conditions.

Chapter 5: Cobalt Porphyrins Intercalated Zirconium Phosphate Layers as Electrocatalysts for the Oxygen Evolution Reaction

5.1 INTRODUCTION

In this chapter we present another approach for the heterogenization of molecular OER electrocatalysts, which is the immobilization of catalytic active metalloporphyrin molecule using a layered structured supporting platform.

Zirconium phosphate (ZrP) is a type of inorganic crystalline layered nanomaterial.^{158,159} It can be classified into zirconium bis(monohydrogen orthophosphate) monohydrate [$\text{Zr}(\text{HPO}_4)_2 \cdot \text{H}_2\text{O}$, α -ZrP] and zirconium bis(monohydrogen orthophosphate) hexahydrate [$\text{Zr}(\text{HPO}_4)_2 \cdot 6\text{H}_2\text{O}$, θ -ZrP].^{160–162} Besides the difference in the number of water molecules per formula unit of these two phase of ZrP, α -ZrP and θ -ZrP respectively presents an interlayer distance of 7.6 Å and 10.4 Å.¹⁶¹ Due to its unique layered structure and the ability of performing intercalation and ion-exchange, as well as its inert chemical properties, ZrP is regarded as a promising supporting platform for encapsulating of both ionic metals, molecules, metal oxides and even polymers, which can then be used in a wide range of applications.^{158,163–166} While α -ZrP is suited for the intercalation of small cations (those smaller than 2.6 Å), θ -ZrP is preferred when larger cations and molecular complexes are being intercalated.^{161,167} A previous study has described the use of θ -ZrP as the host catalyst support for the intercalation of different late transition-metal cations (Fe^{3+} , Fe^{2+} , Co^{2+} and Ni^{2+}) through ion-exchange.¹⁶³ These cation-modified ZrP materials were assessed as electrocatalysts for water oxidation and show promising catalytic efficiencies.¹⁶³ In this work, molecular metalloporphyrins are being supported into θ -ZrP layers and used as OER heterogeneous electrocatalysts.

Herein we report the intercalation of CoTsPP [TsPP = the dianion of meso-tetra(4-sulfonatophenyl)porphyrin] and CoTcPP [TcPP = the dianion of meso-tetra(4-carboxyphenyl)porphyrin] into ZrP using direct reaction of the cobalt porphyrin molecules and θ -ZrP. Different spectroscopic techniques including Fourier-transform infrared (FT-IR) spectroscopy, powder x-ray diffraction (p-XRD), energy dispersive x-ray (EDX) analysis and x-

ray photoelectron spectroscopy (XPS) were used to characterize the successful formation of cobalt porphyrin-intercalated ZrP. We also present the evaluation of both intercalated and pristine ZrP as electrocatalysts for oxygen production through electrochemical measurements.

5.2 Experimental section

Materials. All materials used for synthesis were obtained from commercially available sources. Pyrrole (C_4H_5N), benzaldehyde (C_7H_6O), zirconium(IV) oxychloride octahydrate ($ZrOCl_2 \cdot 8H_2O$), p-chloranil ($C_6Cl_4O_2$) and boron trifluoride diethyl etherate ($C_4H_{10}BF_3O$) were purchased from Sigma Aldrich and cobalt acetate tetrahydrate ($Co(OAC)_2 \cdot 4H_2O$) was purchased from Strem Chemicals. Sulfuric acid (H_2SO_4), phosphoric acid (H_3PO_4), propionic acid ($C_3H_6O_2$), ethanol (C_2H_6O), methanol (CH_4O) and dimethylformamide (C_3H_7NO) were obtained from Fisher Scientific. Pyrrole was freshly distilled before being used and the other chemicals were used as received. Synthesis of θ -ZrP, CoTsPP, CoTcPP and their according porphyrin precursors were achieved by modifying the previously reported methods.

Physical Characterizations: 1H NMR spectra were obtained using a Bruker 400 MHz NMR spectrometer. UV-vis spectra were recorded on a SEC2000 spectra system equipped with a VISUAL SPECTRA 2.1 software. Fourier-transform infrared (FT-IR) spectroscopy was performed on an Agilent Cary 630 FT-IR spectrometer with an attenuated total reflectance (ATR) accessory. X-ray powder diffraction (XRPD) was recorded on a Bruker D8 Discovery x-ray diffractometer with Cu $K\alpha$ radiation source ($\lambda = 1.5406 \text{ \AA}$). Scanning electron microscopy (SEM), elemental mapping and energy dispersive x-ray (EDX) spectroscopy were analyzed on a Hitachi S-4800 instrument equipped with an EDX microanalysis system. X-ray photoelectron spectroscopy (XPS) analysis was carried out on a Physical Electronics PHI 5000 VersaProbe with an Al $K\alpha$ source, where all the spectra were calibrated to the carbon 1s peak at 284.8 eV and fitted using a Shirley background.

Synthesis of θ -Zirconium Phosphate (θ -ZrP) nanomaterial. The synthesis of θ -ZrP was performed following a previously described procedure.¹⁶⁸ A solution containing 100 mL 6.0 M

H₃PO₄ was heated at 94 °C. While stirring, 100 mL of 0.05 M ZrOCl₂·8H₂O in aqueous solution was added dropwise and the reaction mixture was allowed to stir at 94 °C for 2 days. Afterwards, the resultant suspension was centrifuged and the remaining precipitation was washed with deionized water. α-ZrP was obtained upon dehydration of θ-ZrP under vacuum.

Synthesis of meso-tetraphenylporphyrin (H₂TPP).⁸⁷ Benzaldehyde (2.96 g, 0.0275 mol) and pyrrole (1.87g, 0.0279 mol) were dissolved in 500 mL of chloroform. Afterwards, 0.500 mL of BF₃·Et₂O was added dropwise without exposing to air. The reaction mixture was stirred at room temperature when bubbling with N₂ for 2 h, followed by the addition of p-chloranil (6.76 g, 0.0275 mol) and further reacting for 30 minutes. The crude product was purified by column chromatography and recrystallization using methanol.

Synthesis of meso-tetra(4-sulfonatophenyl)porphyrin (TsPP).¹⁴³ H₂TPP (1 g) and sulfuric acid (25 mL) were mixed and stirred at room temperature for 12 h at 100 °C. After cooling down, the reaction mixture was filtered and extracted with deionized water. Then a solution of sodium hydroxide (0.1 M) was slowly added until the pH reached 9.0. The solution was then evaporated and extracted with methanol. The final product was obtained after column chromatography purification.

Synthesis of cobalt meso-tetra(4-carboxyphenyl)porphyrin (CoTsPP).¹⁴³ TsPP (0.250 g, 0.267 mmol) and Co(OAC)₂·4H₂O (0.400 g, 1.60 mmol) were dissolved in deionized water and reacted at 60 °C for 6 h. The metallation was monitor using Uv-vis spectroscopy. The reaction crude was purified through column chromatography. UV-vis (DMSO): λ max: 427, 550 nm.

Synthesis of meso-tetra(4-carboxyphenyl)porphyrin (H₂TcPP).¹⁵⁰ 4-carboxybenzaldehyde (5.00 g, 33.30 mmol) and pyrrole (2.23 g, 33.30 mmol) were refluxing in propionic acid (500 mL) for 2 h with constant stirring. Then to the reaction mixture was added 100 mL methanol and allowed to cool down and filtered using a medium coarse filter frit and washed with warm water. The final product was dried under vacuum. ¹H NMR (d₆-DMSO) δ: 13.28 ppm (s, 4H), 8.86 ppm (s, 8H), 8.36 ppm (m, 16H), -2.95 ppm (s, 2H); UV-vis (EtOH): λ max: 419, 519, 552, 592, 648 nm.

Synthesis of cobalt meso-tetra(4-carboxyphenyl)porphyrin (CoTcPP).¹⁵⁰ A mixture of H₂TcPP (0.100 g, 0.126 mmol) and Co(OAC)₂·4H₂O (0.0320 g, 0.126 mmol) in DMF (20 mL) was reacted under reflux for 1 h. Then the reaction was allowed to cool down and the crude was filtered and the filter cake was washed with deionized water and vacuum dried. UV-vis (EtOH): λ max: 429, 546 nm.

Synthesis of CoTcPP-modified ZrP material (CoTcPP/ZrP). A mixture of CoTcPP (0.0600g, 0.0702 mmol) and θ -ZrP (0.0270 g, 0.0702 mmol) in ethanol (500 mL) was prepared and stirred under room temperature for 5 days. The solution was then centrifuged and the precipitation was obtained and washed with ethanol.

Synthesis of CoTsPP-modified ZrP material (CoTsPP/ZrP). To a solution of CoTsPP (0.0700g, 0.0702 mmol) in deionized water (7 mL) was added θ -ZrP (0.0270 g, 0.0702 mmol), and the resulting suspension was stirred for 5 days under room temperature. The solution was centrifuged and the precipitation was collected and washed with ethanol.

Electrochemical Methods. All of the electrochemical measurements were carried out using a three-electrode electrochemical cell with a modified glassy carbon rotating disk electrode, an Ag/AgCl reference and a Pt wire counter electrode. All cyclic voltammetry studies were performed in 0.1 M KOH electrolyte solutions constantly bubbled with oxygen gas with a scan rate of 10 mV/s. The working electrode was maintained rotated at 1600 RPM. Ohmic correction was performed after each measurement and the resistance of the electrolyte solution was obtained at 100 kHz.

Working Electrode Modification. A mixture of 2.5 mg of carbon black and 5 mg of the catalyst material was dispersed in 1.02 mL isopropanol and 4.08 μ L Nafion solution. The resulting solution was sonicated for 30 minutes in order to form a homogeneous catalyst ink. Then 10 μ L of the as-prepared catalysts ink was dropcasted on top of a glassy carbon electrode with a geometric area of 0.196 cm², which was cleaned by sonication in acetone, isopropyl alcohol, and water prior to use. Afterwards, the glassy carbon disk was rotated at a speed of 600 RPM to dry. The resultant catalyst loading on the glassy carbon disk electrode was 0.25 mg/cm².

5.3 Results and discussion

FT-IR spectra of α -ZrP, CoTsPP, CoTcPP, CoTsPP/ZrP and CoTcPP/ZrP are presented in Figure 5.1. The pure α -ZrP sample shows the characteristic orthophosphate group vibrations at 962 and 1031 cm^{-1} , while the bands observed at 3514 and 3596 cm^{-1} can be attributed to the water molecules inside the ZrP layers and the bands at 1620 and 3145 cm^{-1} are assigned to the –OH groups. These observations are consistent with previously described studies.^{163,169} For the intercalated materials, their FT-IR spectra are dominant by the peaks of ZrP, presumably due to the fact that the molecules are embedded inside the layers and that the amount of molecules being intercalated is minimal compared to ZrP. However, significant shift of the bands are observed after intercalation with the metalloporphyrin molecules. The peaks for the orthophosphate groups in CoTcPP/ZrP and CoTsPP/ZrP are observed at 956-1026 cm^{-1} and 976-1039 cm^{-1} , respectively. The bending vibration for –OH group seen at 1620 cm^{-1} for ZrP exhibit hypochromic shift after intercalation reaction, showing at 1632 cm^{-1} for CoTsPP/ZrP and 1643 cm^{-1} for CoTcPP/ZrP.

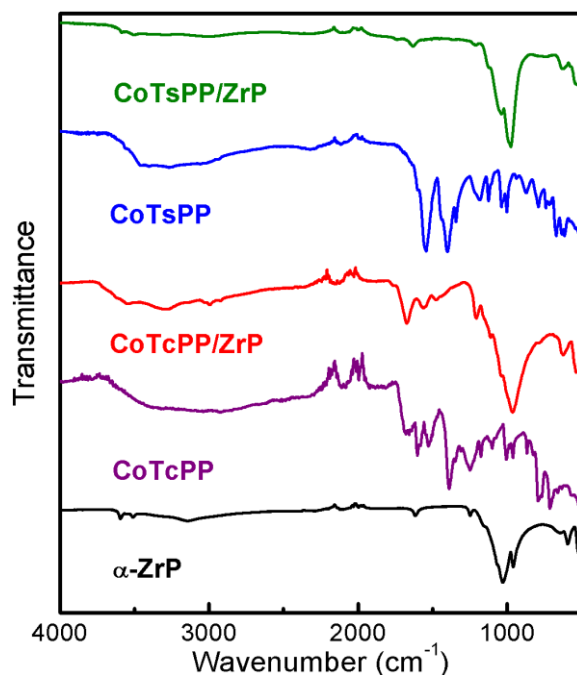


Figure 5.1. FT-IR spectra of (from top to bottom): CoTsPP/ZrP; CoTsPP; CoTcPP/ZrP; CoTcPP and α -ZrP.

The cobalt porphyrin molecules can either be surface bound to ZrP or inserted in the interlayers. While the surface-absorbed species are not supposed to change the layer distance, intercalation of molecules inside ZrP is expected to cause an expansion of the spacing distance between the interlayers, which can be analyzed by Powder x-ray diffraction (p-XRD) measurement. The first diffraction peak at $2\theta = 11.5^\circ$ of α -ZrP (Figure 5.2) is corresponding to the (002) plane, resulting in a layer distance of 7.6 Å. To compare, p-XRD patterns of CoTsPP/ZrP and CoTcPP/ZrP show lower 2θ values of the first diffraction peaks of 9.15° and 9.14° respectively (Figure 5.2), corresponding to interlayer distances of 9.65 Å in both materials. This indicates expanded intercalant species are generated, implying successful intercalation of cobalt porphyrin molecules into the ZrP interlayers. Additionally, the diffraction peaks for (020) and $(31\bar{2})$ reflections at $2\theta = 34^\circ$ remain unchanged before and after intercalation reactions, suggesting the layered structure of ZrP is intact in the intercalated materials.

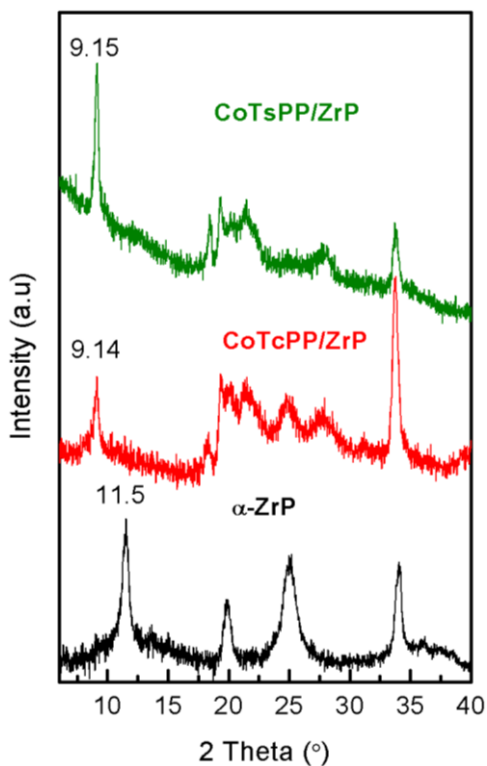


Figure 5.2. Powder x-ray diffraction patterns of CoTsPP/ZrP, CoTcPP/ZrP and α -ZrP (from top to bottom).

The elemental mapping studies and energy dispersive x-ray (EDX) were performed in order to access the elemental composition of α -ZrP, CoTsPP/ZrP and CoTcPP/ZrP, which are depicted in Figures 5.3-5.5. The elemental maps and EDX spectrum of α -ZrP confirm the presence of zirconium, phosphorus and oxygen. By contrast, CoTsPP/ZrP and CoTcPP/ZrP show the existence of cobalt and carbon, in addition to zirconium, phosphorus and oxygen, as can be confirmed by their EDX measurements. The elemental mapping images of all the synthesized materials were also obtained and presented in Figures 5.5-5.7, which are in agreement with their EDX spectra. These results further support that intercalation of CoTsPP and CoTcPP in ZrP has occurred.

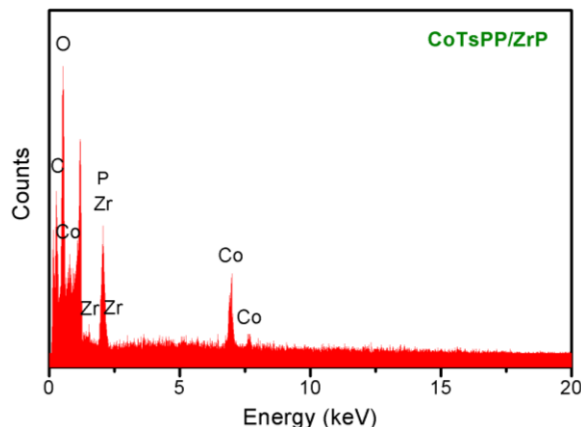


Figure 5.3. EDX spectrum of CoTsPP/ZrP.

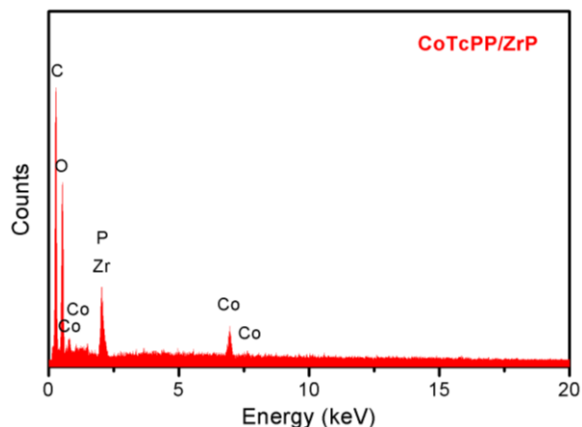


Figure 5.4. EDX spectrum of CoTcPP/ZrP.

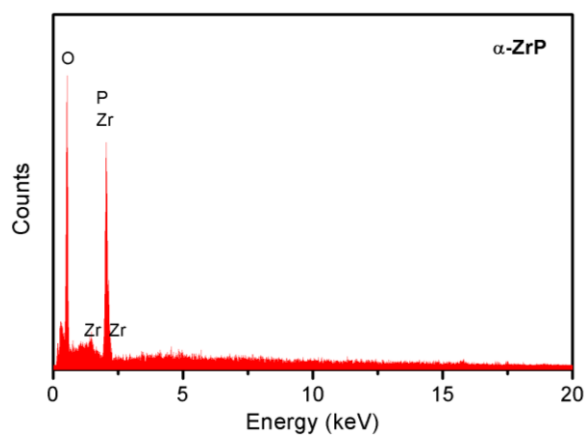


Figure 5.5. EDX spectrum of α -ZrP.

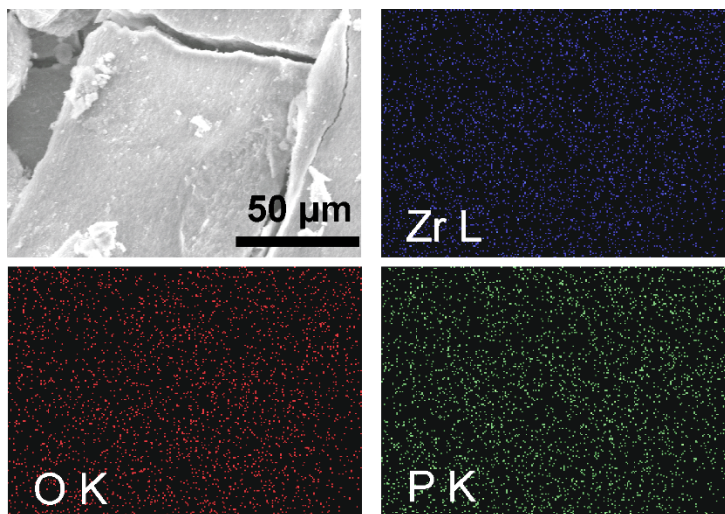


Figure 5.6. SEM image and the according elemental mapping graphs of pristine ZrP.

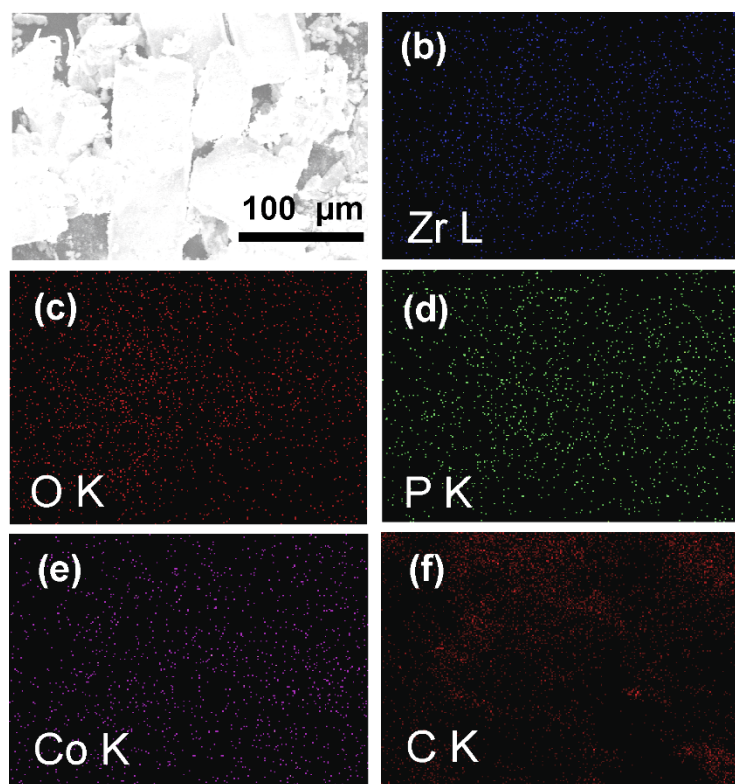


Figure 5.7. SEM image and the according elemental mapping graphs of CoTsPP/ZrP.

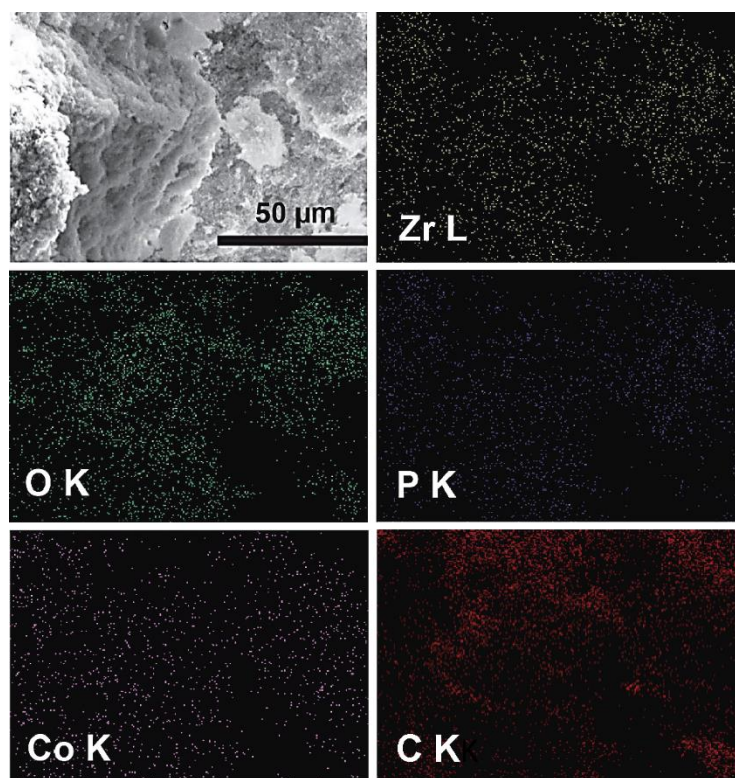


Figure 5.8. SEM image and the according elemental mapping graphs of CoTcPP/ZrP.

The x-ray photoelectron spectroscopy (XPS) survey of all the synthesized materials are displayed in Figure 5.7 in order to analyze the valence of the elements. The binding energies (BEs) of O 1s, Zr 3s, Zr 3p, Zr 3d and P 2p peaks are identical in α -ZrP, CoTsPP/ZrP and CoTcPP/ZrP, which show at 530, 432, 347, 333, and 133 eV, respectively. The existence of an intensive C 1s peak, N 1s and Co 2p peaks in CoTsPP/ZrP and CoTcPP/ZrP are indicative of cobalt porphyrin molecules in these materials. The Co 2p_{3/2} peaks are located at 780 eV for CoTsPP/ZrP and 785 eV for CoTcPP/ZrP, suggesting the presence of Co²⁺ in both samples.

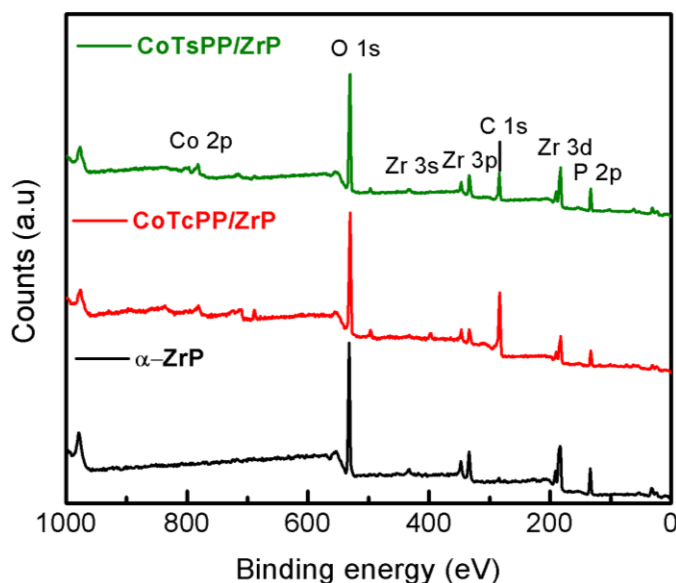


Figure 5.9. XPS survey of CoTsPP/ZrP, CoTcPP/ZrP and α -ZrP.

Cyclic voltammetry was conducted in 0.1 M KOH aqueous solution using the catalyst-modified rotating disk working electrode to evaluate the OER electrocatalytic performance of CoTsPP and CoTcPP intercalated ZrP and the pristine α -ZrP. Cyclic voltammograms of CoTsPP/ZrP and CoTcPP/ZrP (Figure 5.8) indicate both materials are electrocatalytically active by showing immediate increases of anodic catalytic current at relatively low overpotentials (η). To illustrate, in order to reach 10 mA/cm² current density (j), the required η for CoTsPP/ZrP and CoTcPP/ZrP is 0.462 and 0.467, respectively. It should be noted that these cobalt porphyrin intercalated ZrP materials exhibit enhanced efficiencies by acquiring significantly lower

overpotentials comparing to the previously reported transition metal cations (Fe^{2+} , Fe^{3+} , Ni^{2+} and Co^{2+}) modified ZrP OER electrocatalysts ($\eta = 0.490$ to 0.650 V at $j = 10$ mA/cm^2).¹⁶³ Furthermore, pure α -ZrP and carbon black show negligible current density increases.

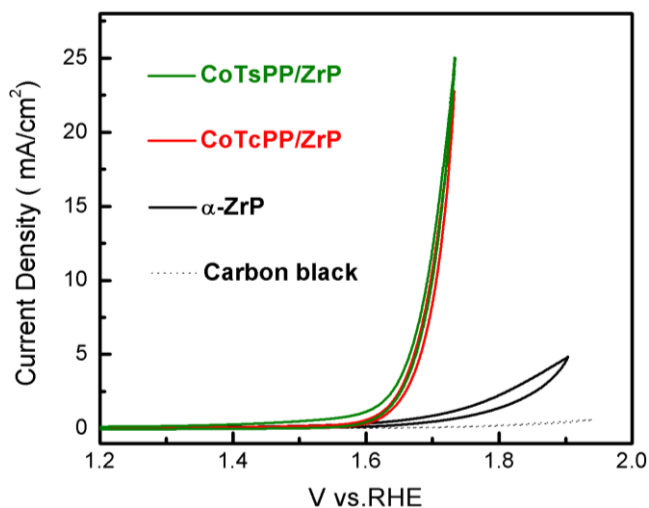


Figure 5.8. Cyclic voltammograms of CoTsPP/ZrP, CoTcPP/ZrP, α -ZrP and carbon black on a rotating disk electrode. Scan rate: 10 mV/s.

5.4 Conclusion

To conclude this chapter, we have shown in this study to use ZrP layered material as a catalyst support for two cobalt porphyrin molecules as OER electrocatalysts. Both molecules have shown to be able to be intercalated into ZrP layers and are active as heterogeneous electrocatalysts to produce oxygen gas from basic aqueous solution. Notably, these cobalt porphyrins-supported ZrP perform enhanced OER electrocatalytic efficiency to similar catalytic systems, in which different transition metal cations were used to be immobilized into ZrP.

Chapter 6: Electrocatalytic Production of Hydrogen Gas by a Cobalt Formamidinate Complex^v

6.1 INTRODUCTION

Current research on HERs mainly focus on transition metal (Fe, Co, Ni, Mn) and metal-free based electrocatalysts.^{31,37,61–63,170–172} Molecular HER electrocatalysts have received substantial interest due to their ease of rational tuning of chemical properties and redox potentials to control their catalytic performance and selectivity.^{73,134,173} In contrast to their bulk heterogeneous counterparts, homogeneous HER molecular catalysts allow for detailed mechanistic study of hydrogen generation by utilizing spectroscopic measurements, among other techniques.^{69,119} One of the most frequently studied groups of molecular electrocatalysts are cobalt-nitrogen coordinated complexes such as cobalt diglyoximes, cobalt porphyrins, cobalt salens, cobalt corroles and cobalt chlorins, etc.^{68,70,72,75,96,143,174} Most of the cobalt complexes studied for hydrogen evolution are supported by electron-withdrawing ligands that tune the redox profile of the metal center by bringing the reduction potential to more anodic ranges, or by redox non-innocent ligands that can participate as electron reservoirs.^{78,175} By contrast, cobalt-nitrogen coordinated complexes based HER electrocatalysts with electron-donating ligands are rare. Yet, the use of electron-donating ligands can potentially increase the electron-richness of the cobalt centers and, thus, enhance the reactivity at the catalytic center. Thus, further exploration of cobalt-nitrogen coordinated complexes bearing electron-donating ligands can provide new insight into the development of new ligand architectures that can improve the performance of homogeneous HER electrocatalysts.

Here in this chapter, we report the synthesis of a novel cobalt complex (**4**) where a single metal center is supported by two electron rich nitrogen-based DippF ligands (DippF = N,N'-bis[2,6-diisopropylphenyl]-formamidinate). We characterized **4** by spectroscopic means including UV-vis, nuclear magnetic resonance (NMR) spectroscopies and x-ray crystallography. Complex **4** was assessed as an electrocatalyst for hydrogen gas evolution by electrochemical measurements

^v This chapter has recently been accepted to be published in *Journal of the Mexican Chemical Society*.

in MeCN with three different organic acids, namely p-toluenesulfonic (tosic) acid, benzoic acid and phenol. HER kinetic studies were also performed by foot-of-the-wave analysis (FOWA) in order to provide insights of the relationship between rate constant and acid concentration.

6.2 EXPERIMENTAL SECTION

General considerations. Synthesis of **4** was accomplished using standard Schlenk techniques under N₂ atmosphere and a dry N₂-filled glovebox. All solvents used were dried using a Pure Process Technology solvent purification system.

Materials. All materials used were purchased from commercially available sources. Tetrabutylammonium hexafluorophosphate (TBAPF₆), p-toluenesulfonic (tosic) acid, benzoic acid, phenol and CoCl₂·6H₂O were dried under vacuum at 60 °C prior to use. All of the solvents used were purified and degassed through a solvent purification system from Pure Process Technology. The remaining chemicals were used as received. HDippF was synthesized according to a previously reported method.¹⁷⁶

Physical measurements. ¹H NMR spectroscopy was recorded on a Bruker 400 MHz NMR spectrometer, using deuterated benzene (C₆D₆) as the solvent. The residual protic signal of C₆D₆ was used as the internal standard (δ = 7.16 ppm). UV-vis spectra were obtained using a SEC2000 instrument with a VISUAL SPECTRA 2.1 software.

Information of x-ray crystal structure of **4**.

A specimen of **4** was used for the x-ray crystallographic analysis. The x-ray intensity data were measured on a Bruker SMART APEX CCD system equipped with a graphite monochromator and a MoK α fine-focus tube (λ = 0.71073 Å). The total exposure time was 4.00 h. The frames were integrated with the Bruker SAINT software package using a narrow-frame algorithm. The integration of the data using an orthorhombic unit cell yielded a total of 22716 reflections to a maximum θ angle of 26.00° (0.81 Å resolution), of which 4567 were independent (average redundancy 4.974, completeness = 100.0%, Rint = 3.81%, Rsig = 3.65%) and 4362 (95.51%) were greater than 2 σ (F₂). The final cell constants of a = 14.4164(7) Å, b = 20.1178(10) Å, c =

15.9876(8) Å, volume = 4636.8(4) Å³, are based upon the refinement of the XYZ-centroids of 9910 reflections above 20 $\sigma(I)$ with $4.784^\circ < 2\theta < 57.66^\circ$. Data were corrected for absorption effects using the multi-scan method (SADABS). The ratio of minimum to maximum apparent transmission was 0.889.

Table 6.1. Data collection and structure refinement for **4**.

Diffractometer	Bruker SMART APEX CCD
Radiation source	fine-focus tube, MoK α
Theta range for data collection	1.74 to 26.00°
Index ranges	-17 ≤ h ≤ 11, -24 ≤ k ≤ 24, -19 ≤ l ≤ 19
Reflections collected	22716
Independent reflections	4567 [R(int) = 0.0381]
Coverage of independent reflections	100.0%
Absorption correction	multi-scan
Structure solution technique	direct methods
Structure solution program	SHELXS-97(Sheldrick 2008)
Refinement method	Full-matrix least-squares on F ²
Refinement program	SHELXL-2014/6 (Sheldrick, 2014)
Function minimized	$\Sigma w(F_o^2 - F_c^2)^2$
Data / restraints / parameters	4567 / 43 / 278
Goodness-of-fit on F²	1.088
Final R indices	4362 data; R1 = 0.0546, wR2 = 0.1517 I > 2 $\sigma(I)$ all data R1 = 0.0566, wR2 = 0.1532
Weighting scheme	$w = 1/[\sigma^2(F_o^2) + (0.0881P)^2 + 7.7217P]$ where $P = (F_o^2 + 2F_c^2)/3$
Absolute structure parameter	0.0(0)
Largest diff. peak and hole	0.486 and -0.612 eÅ ⁻³
R.M.S. deviation from mean	0.079 eÅ ⁻³

The structure was solved and refined using the Bruker SHELXTL Software Package, using the space group C 2 2 21, with Z = 4 for the formula unit, C₅₀H₆₈CoN₄. The final anisotropic full-matrix least-squares refinement on F² with 278 variables converged at R1 = 5.46%, for the observed data and wR2 = 15.32% for all data. The goodness-of-fit was 1.088. The largest peak in

the final difference electron density synthesis was 0.486 e-/Å³ and the largest hole was -0.612 e-/Å³ with an RMS deviation of 0.079 e-/Å³. On the basis of the final model, the calculated density was 1.123 g/cm³ and F(000), 1692 e-.

Evans method.

The magnetic susceptibility was measured through ¹H NMR spectroscopy, which was carried out with a sealed capillary tube containing pure C₆D₆ placed inside a NMR tube already loaded with a solution of **4** (0.0160 g) in C₆D₆ (1.5 mL) in order to measure the chemical shift difference of the solvent caused by the different electronic environments. The number of unpaired electrons (n) was calculated as shown below:^{177,178}

$$\chi_{mass} = \frac{3\Delta f}{4\pi f m} + \chi_0 + \frac{\chi_0(d_0 - d_s)}{m} \quad (\text{Eq 6.1})$$

Where χ_{mass} is the mass susceptibility, Δf is the frequency separation, f is the NMR frequency being studied (400*10⁶ Hz), m is the mass concentration (g/cm³) of **4**, χ_0 is the mass susceptibility of the solvent (−8.8*10^{−9} m³/kg for benzene), d_0 is the density of the solvent and d_s is the density of the solution.

The molar susceptibility (χ_M) is given by:

$$\chi_M = M\chi_{mass} \quad (\text{Eq 6.2})$$

$$\chi_M = N_0\mu_0\xi + \chi_M^{para} \quad (\text{Eq 6.3})$$

$$\chi_M^{para} = \chi_M - N_0\mu_0\xi \quad (\text{Eq 6.4})$$

Where N_0 is the Avogadro's number, μ_0 is the vacuum permeability (4 π *10^{−7} NA^{−2}), ξ is magnetizability, $N_0\mu_0\xi$ is the diamagnetic contribution and χ_M^{para} is the paramagnetic contribution. The effective paramagnetic moment is expressed as:

$$\mu_{eff} = 797.8 \sqrt{T\chi_M^{para}} \text{ Bohr Magnetron} \quad (\text{Eq 6.5})$$

The number of unpaired electrons (n) can be finally calculated through:

$$\mu_{eff}(\text{spin only}) = \sqrt{n(n+2)} \quad (\text{Eq 6.6})$$

Synthesis of 4. Synthesis of **4** was performed in a dried N₂-filled glovebox. Anhydrous CoCl₂ (0.500 g, 3.85 mmol) was dissolved in 20 mL THF using a 50 mL round-bottom flask.

Then, HDippF (2.80 g, 7.70 mmol) was added to the solution. Subsequently, methyllithium (4.81 mL, 7.70 mmol) was added using a glass syringe. The solution changed from a sky blue to a dark aqua-green color. The resulting solution was allowed to vigorously stir under room temperature for 3 h. Afterwards, diethyl ether (Et₂O) was added to precipitate the LiCl byproduct. The resulting suspension was filtered using a medium coarse glass frit packed with Celite. The filtrate was dried under reduced pressure to obtain 1.058 g of the final green product. The product was crystallized using of a concentrated solution of Et₂O. Yield 35.05%. UV-vis: λ max: 564, 628, and 674 nm (Figure A.11).

Electrochemical measurements. Electrochemical measurements were recorded on a CHI760D potentiostat using a three-electrode electrochemical cell in a dry N₂-filled glovebox, with glassy carbon (4mm diameter) as the working electrode, platinum wire and Ag/Ag⁺ as the counter and reference electrode, respectively. Ferrocene (Fc) was added subsequently after each measurement as an internal reference and all potentials displayed are referred to ferrocene/ferrocenium (Fc/Fc⁺) redox couple.

Hydrogen gas detection. Hydrogen gas was confirmed and quantified using a Gas Chromatograph (GC) after performing bulk electrolysis. Bulk electrolysis was operated using a sealed custom-built three-electrode electrochemical cell with an H shape. The working electrode (1 cm² carbon rod), reference electrode (Ag/Ag⁺) were separated with the counter electrode (Pt mesh) through a glass frit. Solutions containing 50 mL of 1 mM of **4**, 0.1 M of TBAPF₆ and 10 mM of the respective acid studied (tosic acid, benzoic acid, phenol) in MeCN were used for bulk electrolysis at a constant potential of -2.0 V vs. Fc/Fc⁺ for 1 h. An aliquot of 300 μ L of the gas in the headspace in the side of the cell containing the working electrode was injected to the GC for analysis.

Calculation of structural geometry index τ_4 for a mononuclear 4-coordinate complex. To disambiguate whether **4** bears closer structural resemblance to a square planar or tetrahedral complex, the model proposed by Yang et al. (Eq 6.7) was used.¹⁷⁹ In this equation, where τ_4 is the structural index, β and α are the two largest valence angles in a 4-coordinate

molecule respectively, and θ is 109.5° . For a 4-coordinate species, a τ_4 of 1 represents a tetrahedral molecule while a τ_4 of 0 indicates a square planar molecule.

$$\tau_4 = \frac{360 - (\beta + \alpha)}{360 - 2\theta} \quad (\text{Eq 6.7})$$

6.3 RESULTS AND DISCUSSION

The solid-state structure of **4** was confirmed by x-ray crystallography (Figure 6.1) and the detailed crystallographic data are summarized in Table 6.2. The bond distances of Co(1)-N(1) and Co(1)-N(2) are 1.998(3) Å and 1.999(3) Å, respectively, which are longer than those of the reported Co diglyoxime complex (1.886(5) Å). The N2-Co1-N2, N1-Co1-N1, N2-Co1-N1 bond angles are found to be 155.0° (2), 151.0° (2), and 119.66° (14) respectively. Based on the bond angles, the calculated geometry index τ_4 is 0.38. Thus, **4** is assigned as a distorted square planar complex.

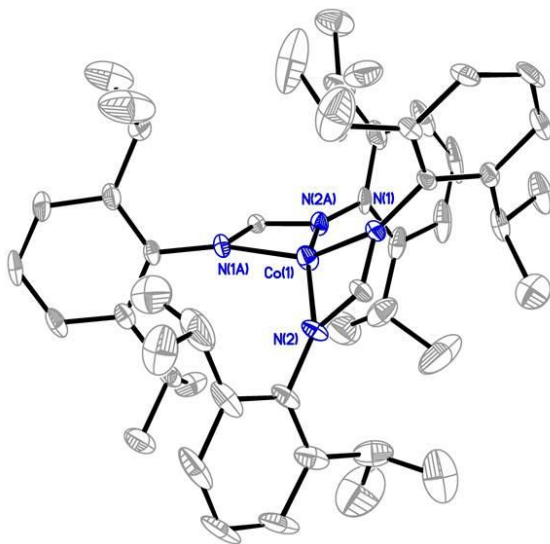


Figure 6.1. Solid-state crystal structure of **4** with thermal ellipsoid shown to be 50%. Hydrogen atoms were omitted for clarity. $R(\text{int}) = 8.58\%$, $R(\text{sigma}) = 2.95\%$.

Table 6.2. Sample and crystal data for **4**.

Identification code	Co(DippF) ₂		
Chemical formula	C ₅₀ H ₆₈ CoN ₄		
Formula weight	784.01 g/mol		
Temperature	100(2) K		
Wavelength	0.71073 Å		
Crystal system	orthorhombic		
Space group	C 2 2 21		
Unit cell dimensions	a = 14.4164(7) Å	α = 90°	
	b = 20.1178(10) Å	β = 90°	
	c = 15.9876(8) Å	γ = 90°	
Volume	4636.8(4) Å ³		
Z	4		
Density (calculated)	1.123 g/cm ³		
Absorption coefficient	0.406 mm ⁻¹		
F(000)	1692		

Table 6.3. Selected bond lengths (Å) for **4**.

Co1-N2	1.998(3)	Co1-N2	1.998(3)
Co1-N1	1.999(3)	Co1-N1	1.999(3)

Table 6.4. Selected bond angles (°) for **4**.

N2-Co1-N2	155.0(2)	N2-Co1-N1	67.28(14)
N2-Co1-N1	119.66(14)	N2-Co1-N1	119.66(14)
N2-Co1-N1	67.27(14)	N1-Co1-N1	151.0(2)

Characterization of **4** by ^1H NMR proved to be challenging due to the intense paramagnetic broadening of the observed signals, reflecting the paramagnetic nature of the complex, and consistent with previous reports of 4-coordinate d^7 Co(II) complexes.^{74,180} The magnetic susceptibility of **4** was probed through the Evans method. The ^1H NMR signal for benzene is shifted by +0.51 ppm in the presence of **4** (Figure 6.2), resulting in a μ_{eff} of 4.13 corresponding to three unpaired electrons (vide supra). This is consistent with other 4-coordinate cobalt complexes bearing nitrogen-donor ligands. The higher μ_{eff} value compared to the predicted spin-only μ_{eff} of 3.87 is attributed to the typical spin-orbit coupling experienced by cobalt.^{181,182}

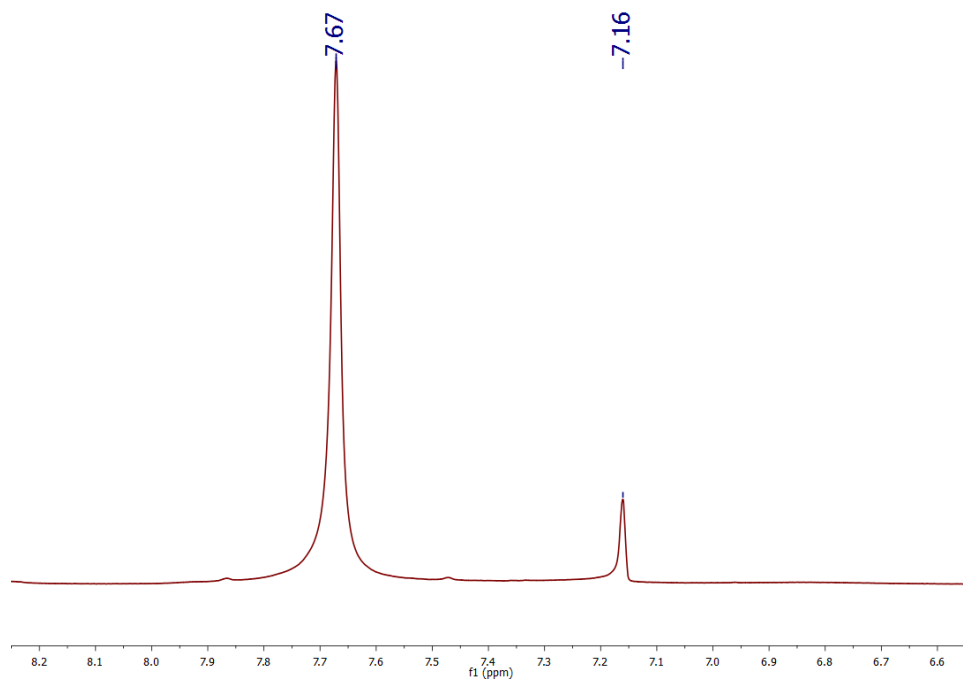


Figure 6.2. NMR spectrum of **4** from Evan's method experiment.

Cyclic voltammograms (CVs) of **4** are presented in Figures 6.3-6.5. Compound **4** shows one nonreversible one-electron reduction wave at $E_p = -1.59$ V vs. Fc/Fc^+ , resulting from the $\text{Co}^{\text{II}}/\text{Co}^{\text{I}}$ reduction couple. The nonreversibility of this event can be attributed to the electron-rich nature of **4**. Upon addition of tosic acid ($pK_a = 8.5$ in MeCN), a catalytic wave is observed with an onset potential of -1.2 V vs. Fc/Fc^+ , accompanying with another reduction wave at $E_p = -1.73$ V vs. Fc/Fc^+ . Another two significantly less acidic proton sources, namely benzoic acid ($pK_a = 21.51$ in MeCN) and phenol ($pK_a = 29.14$ in MeCN), were also introduced to evaluate the electrocatalytic activity of **4**. The CVs of **4** upon addition of both benzoic acid and phenol show considerable increase of cathodic catalytic current for proton reduction, with an onset potential of -1.45 V and -1.89 V vs. Fc/Fc^+ for benzoic acid and phenol, respectively (Figures 6.4-6.5). The ability of **4** to catalyze proton reduction in weak acidic media, which is noteworthy for this type of study, can be attributed to the enhanced electro-activity of the cobalt center due to the electron-donating formamidinate ligand.

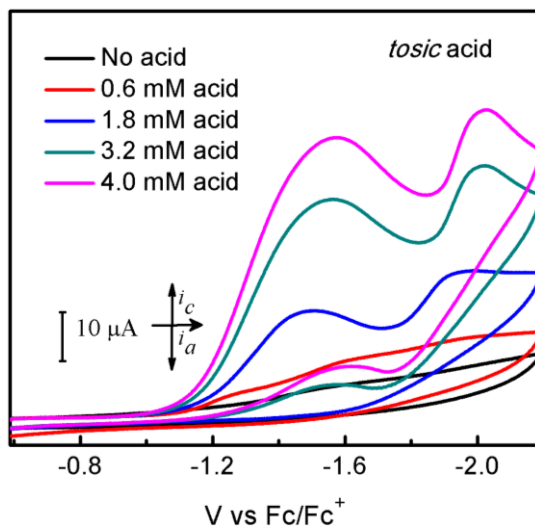


Figure 6.3. Cyclic voltammograms of 1 mM **4** without acid (black line) and with tosic acid (colored lines) in MeCN solution containing 0.1 M TBAPF₆. Scan rate: 100 mV/s; glassy carbon electrode (4 mm diameter).

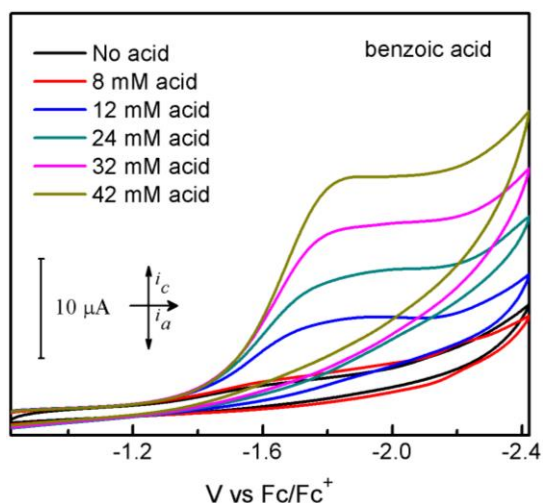


Figure 6.4. Cyclic voltammograms of 1 mM **4** without acid (black line) and with benzoic acid (colored lines) in MeCN solution containing 0.1 M TBAPF₆. Scan rate: 100 mV/s; glassy carbon electrode (4 mm diameter).

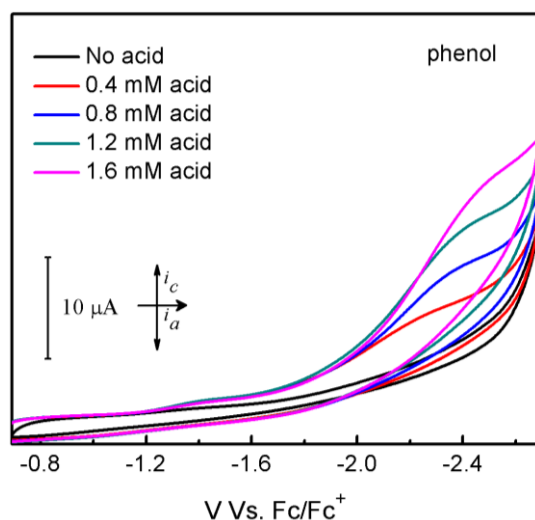


Figure 6.5. Cyclic voltammograms of 1 mM **4** without acid (black line) and with phenol (colored lines) in MeCN solution containing 0.1 M TBAPF₆. Scan rate: 100 mV/s; glassy carbon electrode (4 mm diameter).

Hydrogen gas detection and quantification were carried out after performing bulk electrolysis for 1 h at a constant potential of -2.0 V vs. Fc/Fc^+ using 1 mM of **4** and 10 mM of the chosen acids. The accumulated charge over time (Figure 6.6) shows 36.16, 14.26, 8.08 C of the passed charge for 1 h of electrolysis when using tosic acid, benzoic acid and phenol, respectively, corresponding to Faradaic efficiencies of 91.4%, 85.0% and 100% for hydrogen production.

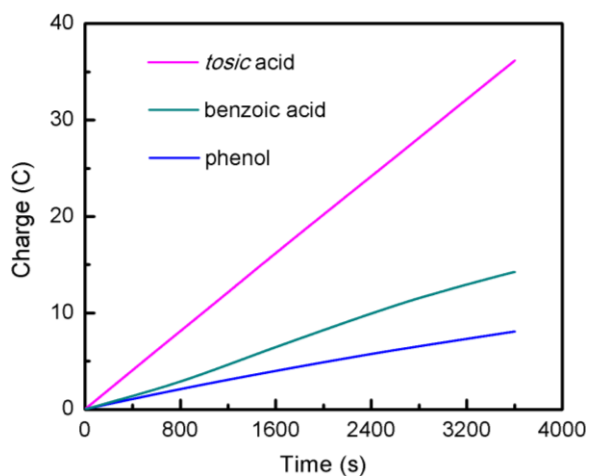


Figure 6.6. Bulk electrolysis experiments of 1 mM **4** containing 10 mM of *tosic* acid, benzoic acid and phenol, respectively. Applied potential: -2.0 V vs. Fc/Fc^+ .

The reaction kinetics of HER using **4** with *tosic* acid was studied through the use of foot-of-the-wave analysis (FOWA). The FOWA plot is presented in Figure 6.7a, which is derived from the linear sweep voltammograms shown in Figure 6.7b. The observed rate constants (k_{obs}) and catalytic rate constants (k_{cat}) at different concentrations of acid addition are summarized in Table 6.5 (see experimental section for detailed calculation). The relationship of k_{obs} with acid concentration is linear (Figure 6.8), suggesting there is a first order dependence on acid concentration.

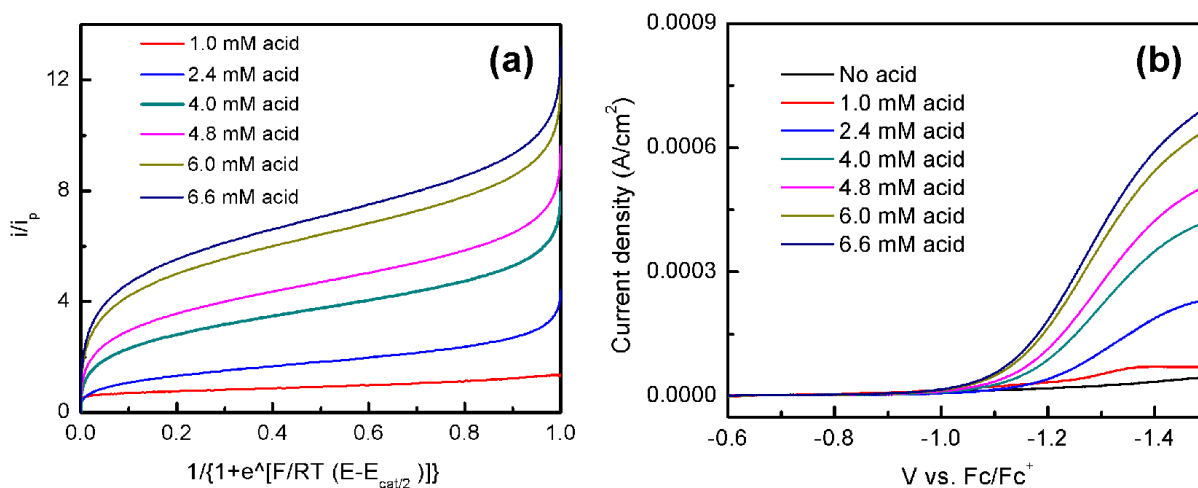


Figure 6.7. (a) FOWA plots of 1 mM of **4** at different concentration of *tosic* acid. Scan rate: 100 mV/s; (b) Linear sweep voltammograms of **4** in MeCN with 0.1 M TBAPF_6 titration with *tosic* acid.

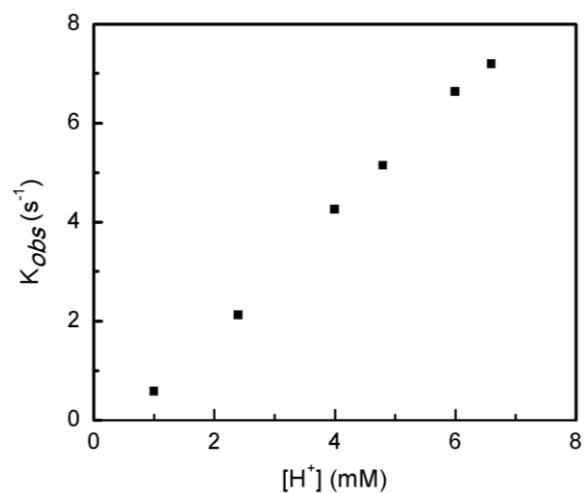


Figure 6.8. Plots of observed rate constant (k_{obs}) versus acid concentration ($[H^+]$).

Table 6.5. Summary of the results of FOWA slope (m), k_{obs} and k_{cat} at different acid concentration.

$[H^+]$ (mM)	m	k_{obs} (s ⁻¹)	k_{cat} (M ⁻¹ s ⁻¹)
1.0	0.58	0.0652	65.2
2.4	2.12	0.872	363
4.0	4.25	3.50	875
4.8	5.14	5.12	1066
6.0	6.63	8.52	1420
6.6	7.19	10.02	1518

6.4 CONCLUSION

In conclusion, we have successfully synthesized a cobalt complex anchored by formamidinate ligand. Structural analysis by x-ray crystallography shows that **4** has a distorted square planar chemical structure and magnetic susceptibility measurements show a μ_{eff} of 4.13 at room temperature, indicative of an electronic structure bearing 3 unpaired electrons. This molecule is found to be active for electrochemical hydrogen generation with both strong acid and weak acid substrates in MeCN. The electrochemical onset potentials for hydrogen generation range from –1.2 V to –1.89 V vs. Fc/Fc⁺. This work shows the potential of using electron rich ligand architectures for tuning the redox activity of cobalt HER electrocatalysts.

Chapter 7: Electrocatalytic Hydrogen Gas Generation by Cobalt Molybdenum Disulfide (CoMoS₂) Synthesized using Alkyl-containing Thiomolybdate Precursors^{vi}

7.1 INTRODUCTION

Transition metal sulfides (TMSs) have been extensively studied as catalysts for hydrodesulfurization (HDS) processes in the petroleum industry.^{183–186} Molybdenum disulfide (MoS₂), is one of the most widely used industrial catalyst for HDS, and has been suggested as a possible HER catalyst through experimental and computational studies.^{44,45,187–190} It is believed that the edge planes of MoS₂ are the active sites when the basal planes are inactive for HER.¹⁹¹ However, the efficiency of MoS₂ as HER electrocatalysts is hindered due to the limited number of exposed edge sites, which are important for catalytic activity.^{183,192} It has been well established that presence of Co to MoS₂ will act as a promoter to increase the reactivity of MoS₂ as a HDS catalyst.^{186,193,194} Co-Mo-S materials are also used in the process of hydrogen production.^{46,195,196}

Ammonium thiomolybdate (ATM) is commonly used as sulfide precursor to prepare Mo-based HDS catalysts such as MoS₂ and Co-promoted MoS₂.¹⁸³ It has been reported that ammonium thiomolybdate precursors containing alkyl groups yield MoS₂ based materials that have higher surface areas and higher reactivity during HDS processes.¹⁹⁷ Previous work has described the use of alkyl-containing thiosalt precursors that lead to superior HDS catalysts compared to the use of ATM.^{198,199} It is suggested that the alkyl groups cause a structural replacement of sulfur by carbon on the edge of the MoS₂ catalyst, which is possibly included in the active sites and then acts as carbon-promoter and leads to increased catalytic activity.^{197,200} Another explanation for the enhanced efficiency is that the decomposition of the alkyl-containing amines also cause the formation of unusual pore distributions to achieve bigger surface areas.²⁰¹ HDS catalysts are known to be viable alternative as HER catalysts.^{49,170} These catalytic processes share the reversible

^{vi} This chapter is excerpted with permission from a published article: Yanyu Wu, M. Zarei-Chaleshtori, Brenda Torres, Thamina Akter, Carlos Diaz-Moreno, Geoffrey B. Saupe, Jorge A Lopez, Russell R. Chianelli, Dino Villagrán; Electrocatalytic hydrogen gas generation by cobalt molybdenum disulfide (CoMoS₂) synthesized using alkyl-containing thiomolybdate precursors, *International Journal of Hydrogen Energy*, **2017**, 42, 20669-20676.

binding of H_2 .²⁰² Thus, this novel synthetic methodology of using amines-pretreated ATM precursors that result in highly efficient HDS catalysts can result in improved HER catalysts.

We present in this Chapter the synthesis and characterization of $CoMoS_2$ materials with different surface areas using different alkyl containing ammonium thiomolybdate precursors. These materials were evaluated as HER catalysts in 0.5 M H_2SO_4 aqueous solution. ATM was treated with three different amines and ammonium bromide salt accordingly, namely 1-dodecylamine (DDA), diethylenetriamine (DETA) and tetradecyltrimethylammonium (TDTA) bromide in aqueous solution to prepare the alkyl containing ammonium thiomolybdate precursors for $CoMoS_2$ catalysts. Electrochemical studies including linear scanning voltammetry, long-term chronoamperometric measurements and bulk electrolysis were carried out to indicate that the $CoMoS_2$ materials synthesized from alkyl-containing thiomolybdates are indeed more active HER electrocatalysts and exhibit high tolerance in strongly acidic media.

7.2 EXPERIMENTAL SECTION

7.2.1 Materials.

$CoCl_2$, diethylenetriamine, 1- dodecylamine, tetradecyltrimethylammonium bromide were purchased from Sigma Aldrich. Sulfuric acid (H_2SO_4) was purchased from Fisher Scientific. All chemicals were used without further purification. Ammonium tetrathiomolybdate was synthesized according to previous reports.²⁰³

7.2.2 Synthesis of $CoMoS_2$ using alkyl-containing thiomolybdates precursors (5-7).

Preparation of alkyl-containing ATM was followed by a simple synthetic technique in aqueous solution improved by Alonso et al.^{198,203} This method involves a one-step substitution of the NH_4^+ from ATM by the alkyl containing amine or ammonium salt. ATM (5.0g, 19.2mmol) was dissolved in 10 mL deionized water (DIW). A solution of 2 equivalents (38.4mmol) amine or ammonium bromide salt in 50 mL DIW was added to form black slurry. (The amines and ammonium bromide salt used are shown in Table 7.1) A solution of $CoCl_2$ (2.5 g, 19.2 mmol) in 10 mL DIW was added to the reaction mixture. The reactor vessel was then heated at 300 °C for

2 h. It should be noted that the amines were evaporated off during the reaction which built up the pressure. Thus pressure was held constant at 1300 Psi to prevent an explosion. After completion, the resultant products were filtered and washed with water and isopropyl alcohol and then dried under reduced pressure.

7.2.3 Synthesis of CoMoS₂ using ATM precursor (8):

This preparation followed the same synthetic procedure of **5-7** except the pretreatment of ATM with amines or ammonium salts was omitted.

7.2.4 Characterization.

All the CoMoS₂ samples were characterized by means of x-ray diffraction (XRD), scanning electron microscopy (SEM) and Brunauer-Emmett-Teller (BET) analyses. XRD data were obtained on a Bruker D8 Discover x-ray Diffractometer. SEM studies were performed using a SEM, Hitachi S-4800 instrument. Surface area analyses were obtained on a Micromeritics Accelerated Surface Area and Porosity System (ASAP 2020). The x-ray Photoelectron Spectroscopy (XPS) analyses were carried out with a PHI 5600 spectrometer with a hemispherical energy analyzer, using magnesium (MgK α) source of 1253.6 eV at 100 Watts. The samples for analysis were prepared using a kapton tape for ultrahigh vacuum system.

7.2.5 Preparation of CoMoS₂/FTO (fluorine-doped tin oxide) electrode.

Catalysts CoMoS₂/DDA, **(5)**; CoMoS₂/DETA, **(6)**; CoMoS₂/TDTA, **(7)**; and CoMoS₂/ATM, **(8)** were coated on FTO glass substrates with silver paste prior to the electrochemical measurements and employed as working electrodes in electrochemical studies. 2 mg CoMoS₂ was dispersed in 10 mL ethanol and ultrasonicated for 30 minutes to generate a homogenous suspension. FTO glass was cleaned with water and acetone before a thin layer of silver paste was coated on top of the active side of the FTO glass with an area of 0.25 cm² (0.5cm * 0.5cm). 10 μ L of the catalysts suspension was dropcasted on top of the silver paste. The CoMoS₂/FTO substrates were then allowed to dry prior to use.

Table 7.1. Summary of the parameters of the CoMoS₂ catalysts reported in this study.

Sample	Amine	Specific surface area (m ² /g)
5	1-Dodecylamine	69
6	Diethylenetriamine	43
7	Tetradecyltrimethylammonium bromide	63
8	None	35

7.2.6 Electrochemical measurements.

Electrochemical measurements were obtained using a CHI760D potentiostat. A platinum mesh was used as counter electrode and a saturated calomel electrode (SCE) as a reference electrode. The potentials displayed were referred to reversible hydrogen electrode (RHE). Aqueous H₂SO₄ solutions were purged with nitrogen gas to remove the dissolved oxygen. Electrical impedance spectroscopy (EIS) was obtained at an overpotential of 0.25 V from 100 KHz to 0.1 Hz with AC voltage of 5 mV. Bulk electrolysis and chronoamperometric measurements were performed in a custom-built two-compartment gas-tight electrochemical cell under argon atmosphere. One part of the cell contains: (i) CoMoS₂/FTO working electrode (1 cm²); (ii) SCE reference electrode; (iii) gas inlet and gas outlet. The other part of the cell contains a Pt mesh auxiliary counter electrode and gas outlet. The working and counter electrodes are separated through a fine glass frit. The electrolyte solution on the compartment containing the working electrodes was kept stirring to remove the in situ-generated H₂ bubbles.

7.2.7 Potential calibration.

All potentials obtained referenced to SCE were calibrated with respect to RHE. A 2 mm diameter platinum working electrode was used for cyclic voltammetry in 0.5 M H₂SO₄ solution at a scan rate of 50 mV/s. The potential at which the cathodic current increase was constantly observed to be -0.27 V vs. SCE. Thus the potentials obtained using a SCE reference electrode were added by +0.27 V in order to be referred to RHE.

7.2.8 Quantitative hydrogen gas measurement.

After performing bulk electrolysis, the evolved H_2 gas in the headspace was measured by using a gas chromatograph (GC) (series 350, Gow-Mac, PA, USA) equipped with a thermal conductivity detector (TCD). A sample lock syringe (gas tight-1750, Hamilton company, Nevada, USA) was used to withdraw gas samples from reactor cell for the quantification in the GC. The generated amount of hydrogen gas and charge were used to calculate the Faradaic efficiency based on Faraday's law.

7.2.9 H_2 calibration concentration:

Calibration of H_2 concentration was performed to determine the content of H_2 gas in the headspace. Using a 100 μL syringe, different volumes of gas were collected and injected into the injection port of GC. The H_2 concentration is directly proportional to its volume. Three separate volumes of 10, 20 and 30 μL of ultra-pure H_2 were analyzed to calibrate the instrument by calculating their respective peak areas. The linear regression coefficient was found in the range of 0.97-0.99 (See Figure 7.1).

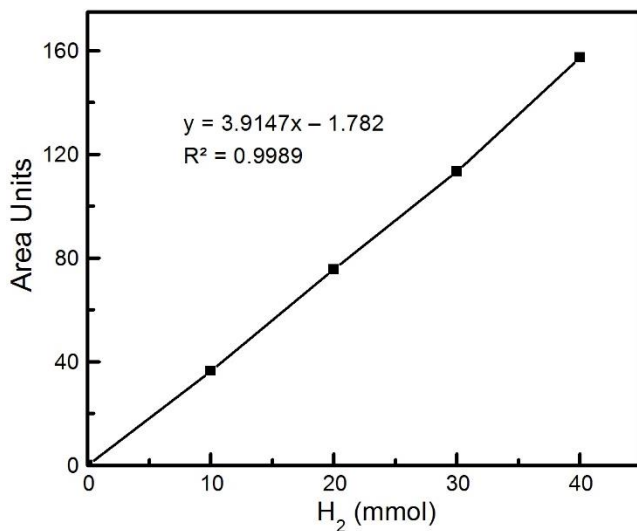


Figure 7.1. Calibration curve for evolved H_2 quantification.

7.2.10 Determination of Faradaic efficiency:

In order to determine the Faradaic efficiencies of the catalysts for hydrogen gas production, bulk electrolysis experiments were performed for 1 h at a constant applied potential of -0.5 V vs. RHE in 0.5 M H_2SO_4 . Quantifications of H_2 gas generated were determined as described previously using gas chromatography. Faradaic efficiency was calculated using the following equation:

$$\text{Faradaic efficiency (\%)} = [96485 * 2 * \text{mol H}_2 \text{ (GC)} * 100\%] / Q$$

7.3 RESULTS AND DISCUSSION

7.3.1 Characterization.

The surface areas of the synthesized CoMoS_2 samples pretreated with amines or ammonium salt range from $43 - 69 \text{ m}^2/\text{g}$ (Table 7.1). Sample **5** shows the highest surface area while **6** exhibits the lowest. Comparing to sample **8**, samples **5-7** all show an increase of their surface area. SEM experiments were performed to reveal the morphology of the CoMoS_2 using different alkyl containing and non-alkyl containing ATM precursors. Figures 7.2a-c, show the SEM images of **5-7**, respectively. These images show that the samples present irregular spherical particles on their surface. These materials present cavities and pores which can be attributed to the decomposition of amines at high temperature during synthesis. Catalyst **8**, which was synthesized directly from ATM without the addition of amines, shows a denser morphology and the lack of spherical particles when compared to **5-7**. SEM elemental mapping image of

5 is presented in Figure 1e and images of **6-8** are shown in Figures A.12-14. All of the images show the presence of Co, Mo and S, implying the successful addition of Co to MoS₂.

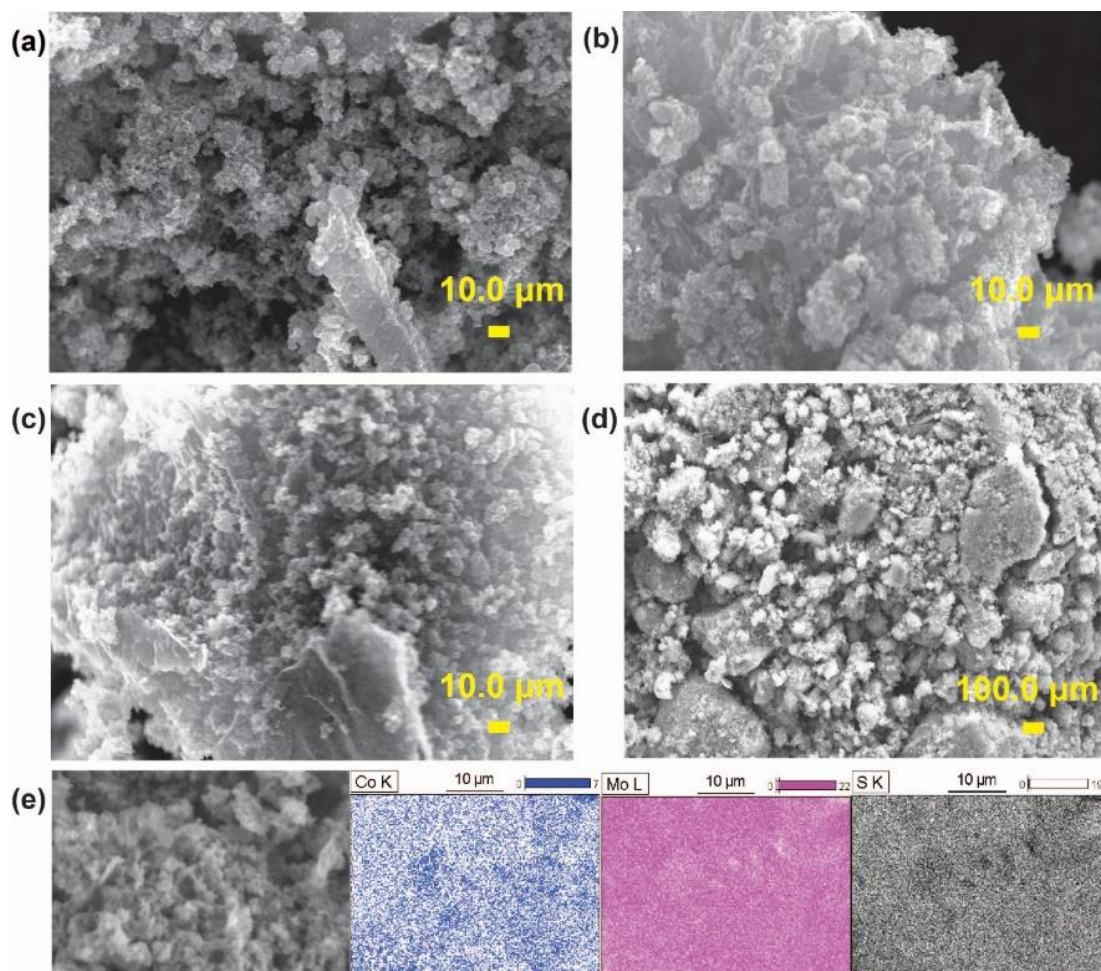


Figure 7.2. (a-d): Scanning electron micrographs of **5-8**, a-d respectively; e: SEM and the corresponding elemental mapping of **5**.

The XRPD pattern of **8** is in agreement with other reports of CoMoS₂ (Figure 7.3).²⁰⁴ As comparison, XRPD patterns for all CoMoS₂ catalysts (**5-7**) treated with amines exhibit weak and disperse diffraction peaks (Figure 7.3), indicating the poor crystalline characteristic of Co-promoted MoS₂. The diffraction peak at $2\theta = 14.4^\circ$ which is characteristic of the (0 0 2) basal planes of crystalline MoS₂, is broadened for **7** and absent in the case of **5** and **6**. This results from the carbon after decomposition of the amines, which is similar to the dispersion of carbon supported MoS₂ catalysts.²⁰⁵

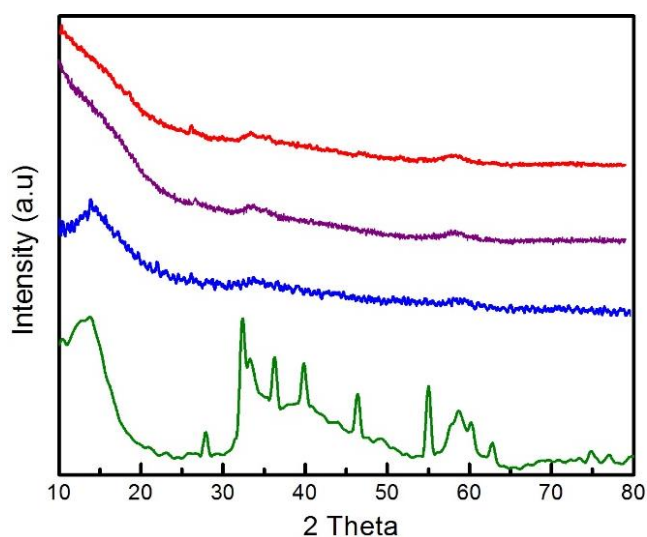


Figure 7.3. XRD patterns of CoMoS₂ catalysts: **5** (red); **6** (purple); **7** (blue); **8** (green).

The elemental composition and valence states of CoMoS₂ are determined by XPS studies. XPS data confirm the existence of Co, Mo and S for samples **5-8**, see Figure 7.4. The binding energy (BE) found at 100.9 eV is ascribed to Co 3s. The existence of S is demonstrated by the peak at 162.05 eV, which is related to S 2p_{1/2}. Another peak found at 168.4 eV is attributed to S 2p_{3/2} in the form of SO₂. The peaks at 228.6 and 232.82 eV are assigned to Mo⁴⁺ 3d_{5/2} and Mo⁴⁺ 3d_{3/2}. And the peaks found at 232.80 eV and 399.1 eV and are related to Mo⁶⁺ 3d_{5/2} and Mo⁶⁺ 3p_{3/2} respectively in the form of CoMoO₄. The BE at 531.1 eV arises from the adventitious oxygen forming traces of MoO₂, CoO and Co₃O₄. The presence of oxygen at the surface may be the result of air exposure as previously reported by others.²⁰⁶

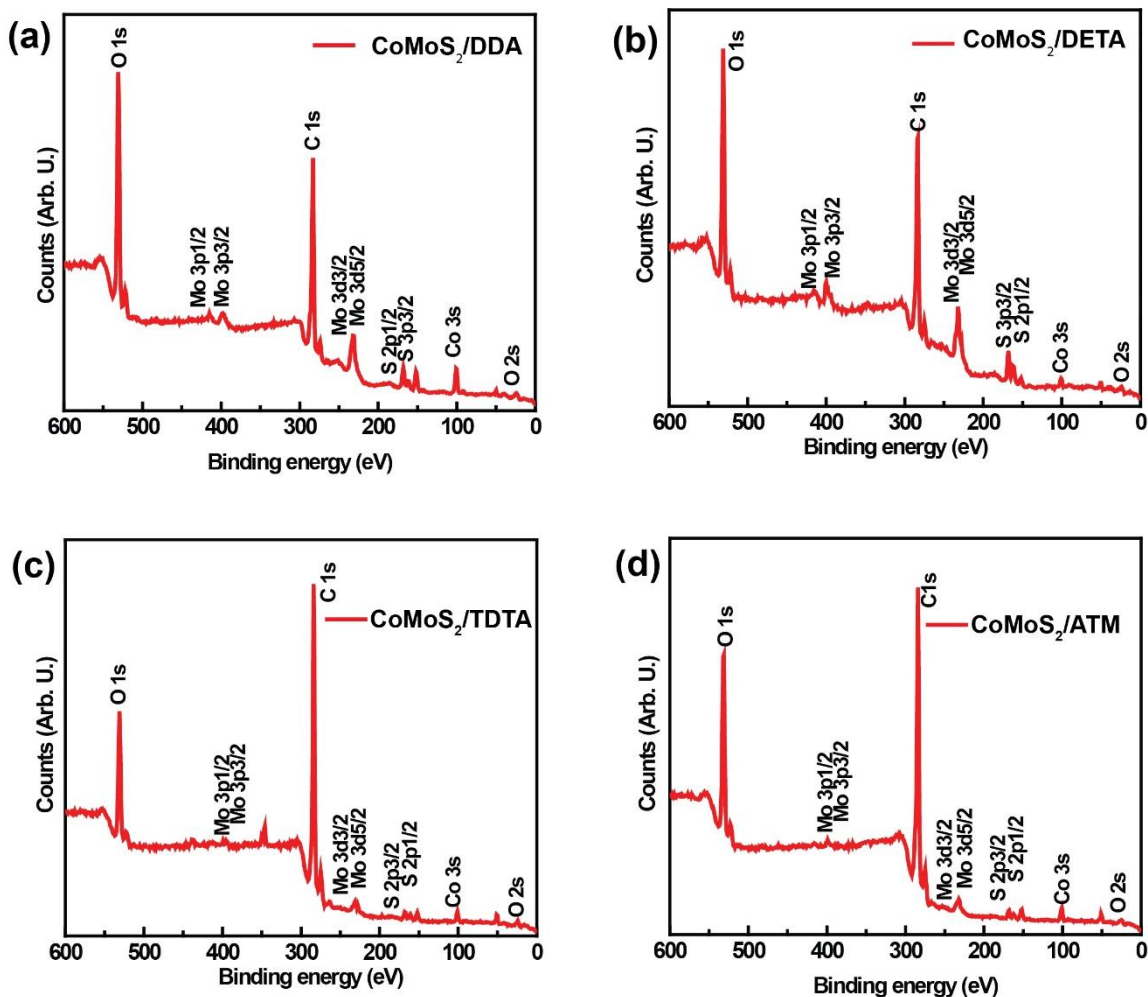


Figure 7.4. XPS survey of (a) **5**; (b) **6**; (c) **7**; (d) **8**.

7.3.2 Electrocatalytic HER activity

The electrocatalytic HER behaviors of the prepared CoMoS₂ samples were assayed in a 0.5 M H₂SO₄ aqueous solution. Figure 7.5a shows the HER polarization curves when using the prepared CoMoS₂/silver/FTO working electrodes with a linear scanning voltammetry until current densities reach 10 mA/cm². Two control working electrodes were evaluated under the same condition as comparison. One of the control working electrodes is platinum metal, which is a benchmark electrocatalyst for hydrogen generation. Platinum shows an immediate enhancement of catalytic current at 0 V vs. RHE.

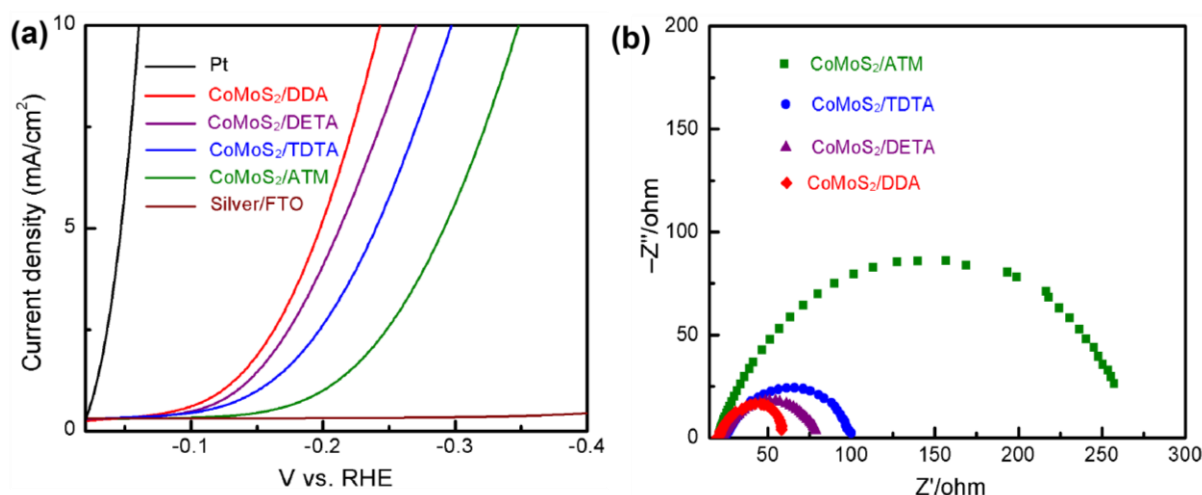


Figure 7.5. (a) Polarization data of Pt (black); **5** (red); **6** (purple); **7** (blue); **8** (green) and blank silver-coated FTO glass (burgundy) in 0.5 M H₂SO₄ aqueous solution. Scan rate: 2 mV/s; (b) Nyquist plots of the as-prepared catalyst-deposited FTO/silver

A blank FTO glass coated with silver paste, which is the substrate for preparing the CoMoS₂ electrode, was also tested, and it shows negligible current increase at potentials between 0 V to – 0.4 V vs RHE. Catalysts **5**, **6**, **7** and **8** exhibit the onset overpotential (η) at which the increases of cathodic catalytic current are observed, are 0.127 , 0.131, 0.144 and 0.173 V and η at 10 mA/cm² are 0.244, 0.261, 0.298, 0.349 V, respectively. Compared to catalyst **8**, catalysts **5-7** show considerably positive shift of η and faster kinetics at catalyzing HER. Nyquist plots of sample **5-8** at the same η of 0.25 V are obtained from EIS experiments and displayed in Figure 7.5b. Sample **5-7**, which are amines-pretreated, show significantly small diameters of semicircles compared to **8**, which correspond to better conductivity and faster charge transfer. These results show that pretreatment of ATM with amines to form alkyl-containing thiomolybdates provide a promising way to afford Mo-based HER catalysts with enhanced efficiency.

Figure 7.6 displays the Tafel plot data of **5-8** and of a platinum electrode as a control, which were fitted in the Tafel equation ($\eta = b \log j + a$, where j is the current density and b is the Tafel slope). The platinum control Tafel plot shows a slope of 30 mV/dec, which is in agreement with the known mechanism of Pt as HER electrocatalyst.⁴⁷ The linear region for the presented Tafel plot of catalysts **5-8** are plotted from where the current densities reach from 1 to 10 mA/cm². Catalyst **5** yields the lowest Tafel slope of 124 mV/dec, which shows 23 mV/dec less than **8** (147 mV/dec). In comparison, catalyst **6** and **7** exhibit very similar Tafel slope of 141 and 146 mV/dec respectively. These results show that catalyst **5** greatly improves the reaction kinetic by presenting a lower Tafel slope. According to previous studies, the catalyst follow a Volmer–Heyrovsky mechanism.²⁰⁷

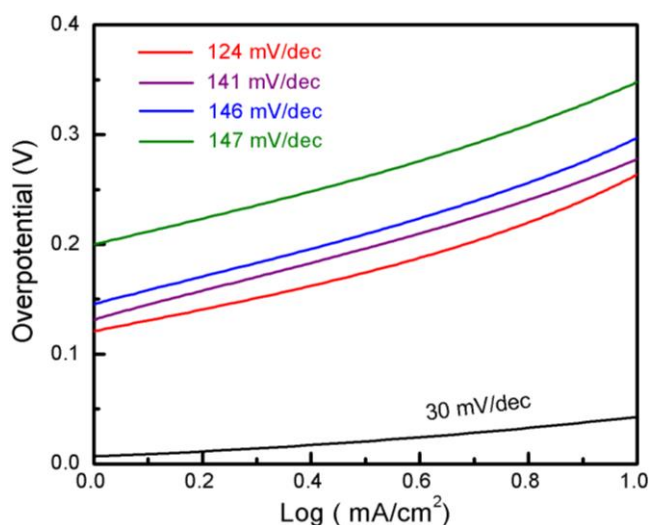


Figure 7.6. Tafel plot [overpotential vs log (current density)] for (from bottom to top): Pt (black); **5** (red); **6** (purple); **7** (blue); **8** (green) derived from Figure 7.5a.

To quantify the hydrogen gas generated, bulk electrolysis along with gas detection were performed. Bulk electrolysis of catalysts **5-8** were performed in 0.5 M H₂SO₄ aqueous solution at a constant potential of −0.5 V vs. RHE for 1 h prior to the gas analysis. Figure 7.7 shows the bulk electrolysis data obtained by maintain a constant voltage and measuring the total charge generated as a function of time. The amount of H₂ gas evolved represents a Faradaic yield between 98% and

100%, implying a quantitative faradaic yield for hydrogen generation. It should also be noted that the blank silver-coated FTO glass generates negligible charge and shows no H₂ generation at the same potential.

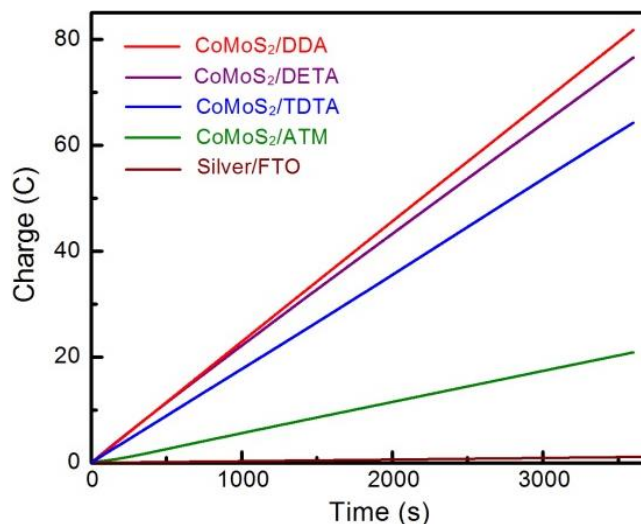


Figure 7.7. Bulk electrolysis experiments of (from top to bottom) **5-8** and blank silver-coated FTO glass in 0.5 M H₂SO₄ aqueous solution. Applied potential: -0.5 V vs. RHE.

These catalysts were evaluated to be stable through electrocatalysis in strong acidic condition by long-term chronoamperometric measurements using the prepared CoMoS₂/silver/FTO working electrodes in 0.5 M H₂SO₄ electrolyte at a constant potential of -0.2 V vs. RHE. As is presented in Figure 7.8a, all catalysts are still shown to be electrocatalytic active after 10 h' continuous operation, indicating the promising practical use of these catalysts in large hydrogen gas production technologies. The HER catalytic stabilities are also observed by linear scanning voltammetry of the catalysts after 500 scans. It can be seen that there are minimal changes in the polarization curves between the initial scans and the ones after 500 cycles (Figure 7.8b). The morphology and elemental composition of all the catalysts after 10 h' electrolysis in 0.5 M H₂SO₄ were also studied. Figures A.15-18 show the SEM images and the corresponding elemental mapping of **5-8** respective after electrolysis. There are no apparent changes in the SEM images of

5-8. Sample **5-7** still present small round particles and sample **8** retains its dense morphology. After long-term electrolysis, all materials still maintain the effective composition of Co, Mo, and S.

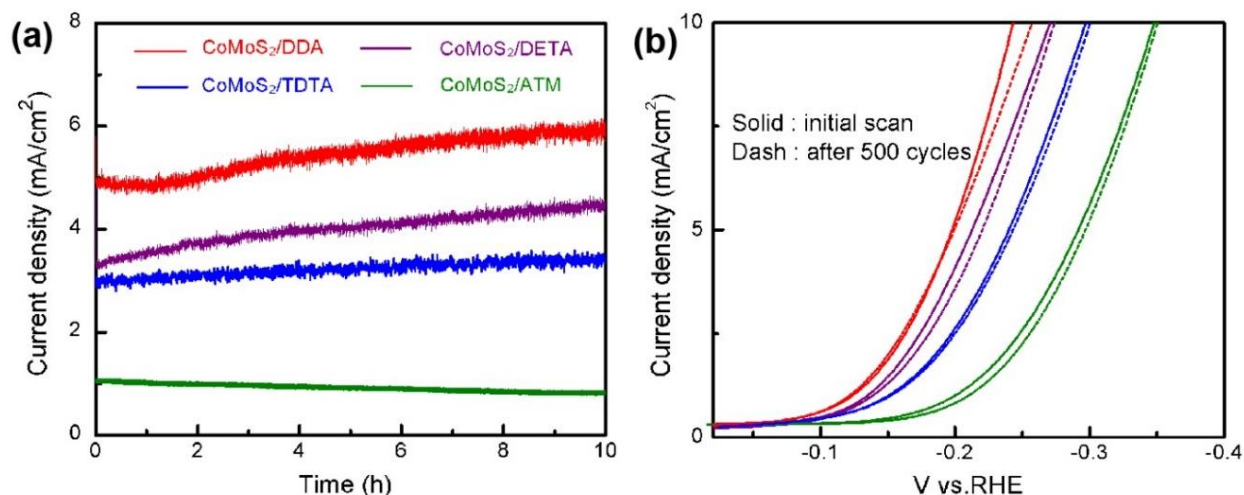


Figure 7.8. (a) Chronoamperometric responses ($j \sim t$) using **5-8**/silver/FTO working electrodes in 0.5 M H₂SO₄ for 10 h at -0.2 V vs. RHE. Sample **5** (red); **6** (purple); **7** (blue); **8** (green) and blank silver-coated FTO glass (burgundy); (b) Polarization data of **5-8** in 0.5 M H₂SO₄ aqueous solution before and after 500 cycles of scans. Scan rate: 2 mV/s.

7.4 CONCLUSION

We report a simple synthesis of CoMoS₂ catalysts using ATM treating with different amines and ammonium bromide salt including 1- dodecylamine, diethylenetriamine, and tetradecyltrimethylammonium bromide which form different alky containing ATM precursors. These materials are amorphous and with porous surfaces that show reasonable large surface area. Electrochemical studies along with hydrogen gas analysis in 0.5 M H₂SO₄ aqueous media indicate that these materials exhibit enhanced HER efficiencies compared to the CoMoS₂ catalyst synthesized using ATM precursor and present great stabilities. This study suggests the possibility of using simple one-step pre-treatment of ATM to afford more active Mo-based HER electrocatalysts.

Chapter 8: Conclusion

In this dissertation, we have demonstrated the use of a metal-free perfluorinated porphyrin to catalyze proton reduction in order to generate hydrogen gas homogeneously in organic media. UV-vis and UV-vis spectroelectrochemical measurements as well as DFT theoretical calculations were utilized in order to provide mechanistic insights of how this metal-free species is able to evolve hydrogen gas electrocatalytically. When two electron and two proton transfer processes are accounting for the release of one molecule of dihydrogen, we propose a mechanistic route of *E-P-E-P* (where *E* stands for electron transfer and *P* stands for proton transfer) when using *p*-toluenesulfonic acid as the proton source and THF as the solvent. These results show the potential use of organic complexes that display redox properties and present protonation sites in close proximity as electrocatalysts for catalytic hydrogen gas generation, where typically requires active metal cores. Further exploration of other metal-free porphyrins and similar organic macrocycles as HER and OER electrocatalysts is of immense interest as current and future studies in our laboratory.

While homogeneous electrocatalysts are important for the elucidation of reaction mechanisms due to the ease of implementation of spectroscopic measurements, heterogeneous catalysts are preferred in practical industrial processes because they are typically more efficient and robust. Thus, we explored two different methods to heterogenize molecular metalloporphyrin electrocatalysts for HER and OER. The first method is the construction of polymeric networks based on metalloporphyrin units. We present a cobalt porphyrin polymer synthesized by the combination of $\text{Co}(\text{NO}_3)_2$ and meso-tetra(4-carboxyphenyl)porphyrin at mild temperature of 60 °C for 3 days, which exhibits crystalline character and moderately high surface area of 441.71 m^2/g . This polymer shows clear evidence of improved HER efficiency when comparing to its discrete cobalt porphyrin molecule counterpart and shows remarkable robustness for long-term electrolysis even under strong acidic conditions. We also explored the synthesis of two porphyrin based organic polymers via an one-step condensation reaction of pyrrole and two different

aldehydes, namely terephthalaldehyde and tetrafluoroterephthalaldehyde respectively, using propionic acid as both the solvent and catalyst. Both polymers were treated as precursors to prepare metalloporphyrin polymers using cobalt and iron through direct metallation. While the metal-free organic polymers are not active for the electrocatalytic OER, all of the metallated polymers show to be active towards OER with moderate overpotentials that are comparable to other similar porphyrin-based extended network catalytic systems. Another approach for constructing porphyrin-based heterogeneous electrocatalysts involves the use of zirconium phosphate layered nanomaterial as a platform for the embedding of molecular cobalt porphyrin molecules. These metalloporphyrin intercalated ZrP materials are assessed to be active OER electrocatalysts that are superior to similar reported catalytic systems, in which different transition metal cations were used to be immobilized into ZrP through ion exchange.

In this dissertation, we also report a novel molecular cobalt complex $[\text{Co}(\text{DippF})_2]$ which was evaluated to be an active HER electrocatalyst. This molecule consists of a mono cobalt center coordinated to two formamidinate ligands showing a distorted square planar molecular structure. We probed the HER electrocatalytic activity of $\text{Co}(\text{DippF})_2$ using strong acid (p-toluenesulfonic acid) as well as weak acids (benzoic acid and phenol) and it displays electrocatalytic activity to generate hydrogen gas upon the addition of all of the three organic acids studied. We attribute its noteworthy HER catalytic performance in the presence of weak acids to the use of basic ligands that increases the electron-richness of the cobalt center, which presumably enhances the redox reactivity of the molecule.

Lastly, we describe an improved synthesis of cobalt-promoted MoS_2 (CoMoS_2) materials, where we pretreated the ammonium thiomolybdate precursor with different amines containing long alkyl chains prior to the reaction of CoCl_2 to obtain the desired CoMoS_2 . Upon decomposition of the alkyl-containing amines, pores were generated in the surfaces of the materials resulting in the generation of CoMoS_2 materials that are amorphous and show increased surface areas comparing to the one without amine-pretreatment, which is crystalline. Assessment of these CoMoS_2 samples as heterogeneous electrocatalysts for HER in strong acids show that all of the

amine-pretreated CoMoS₂ exhibit significantly improved catalytic activity by requiring less overpotential for hydrogen generation than the CoMoS₂ synthesized directly from ammonium thiomolybdate and CoCl₂. This synthetic method can be potentially further employed in the designing of other HER electrocatalysts such as transition-metal carbides, nitrides and phosphides.

References

- (1) Lewis, N. S.; Nocera, D. G. Powering the Planet: Chemical Challenges in Solar Energy Utilization. *Proc. Natl. Acad. Sci.* **2006**, *103* (43), 15729–15735.
- (2) Seh, Z. W.; Kibsgaard, J.; Dickens, C. F.; Chorkendorff, I.; Nørskov, J. K.; Jaramillo, T. F. Combining Theory and Experiment in Electrocatalysis: Insights into Materials Design. *Science* **2017**, *355* (6321).
- (3) Gray, H. B. Powering the Planet with Solar Fuel. *Nat. Chem.* **2009**, *1* (1), 7–7.
- (4) Hunter, B. M.; Gray, H. B.; Müller, A. M. Earth-Abundant Heterogeneous Water Oxidation Catalysts. *Chem. Rev.* **2016**, *116* (22), 14120–14136.
- (5) Hoffert, M. I.; Caldeira, K.; Jain, A. K.; Haites, E. F.; Harvey, L. D. D.; Potter, S. D.; Schlesinger, M. E.; Schneider, S. H.; Watts, R. G.; Wigley, T. M. L.; et al. Energy Implications of Future Stabilization of Atmospheric CO₂ Content. *Nature* **1998**, *395* (6705), 881–884.
- (6) Lewis, N. S.; Crabtree, G. *Basic Research Needs for Solar Energy Utilization: Report of the Basic Energy Sciences Workshop on Solar Energy Utilization, April 18-21, 2005*; Lewis, N. S., Crabtree, G., Nozik, A. J., Wasielewski, M. R., Alivisatos, P., Eds.; US Department of Energy, Office of Basic Energy Science: Washington, DC, 2005.
- (7) Ataeivarjovi, E.; Tang, Z.; Chen, J. Study on CO₂ Desorption Behavior of a PDMS–SiO₂ Hybrid Membrane Applied in a Novel CO₂ Capture Process. *ACS Appl. Mater. Interfaces* **2018**, *10* (34), 28992–29002.
- (8) Davis, S. J.; Caldeira, K.; Matthews, H. D. Future CO₂ Emissions and Climate Change from Existing Energy Infrastructure. *Science* **2010**, *329* (5997), 1330–1333.
- (9) Kapilashrami, M.; Zhang, Y.; Liu, Y.-S.; Hagfeldt, A.; Guo, J. Probing the Optical Property and Electronic Structure of TiO₂ Nanomaterials for Renewable Energy Applications. *Chem. Rev.* **2014**, *114* (19), 9662–9707.

- (10) Walter, M. G.; Warren, E. L.; McKone, J. R.; Boettcher, S. W.; Mi, Q.; Santori, E. A.; Lewis, N. S. Solar Water Splitting Cells. *Chem. Rev.* **2010**, *110* (11), 6446–6473.
- (11) Sivula, K.; Le Formal, F.; Grätzel, M. Solar Water Splitting: Progress Using Hematite (α -Fe(2) O(3)) Photoelectrodes. *ChemSusChem* **2011**, *4* (4), 432–449.
- (12) Dempsey, J. L.; Esswein, A. J.; Manke, D. R.; Rosenthal, J.; Soper, J. D.; Nocera, D. G. Molecular Chemistry of Consequence to Renewable Energy. *Inorg. Chem.* **2005**, *44* (20), 6879–6892.
- (13) Dresselhaus, M. S.; Thomas, I. L. Alternative Energy Technologies. *Nature* **2001**, *414* (6861), 332–337.
- (14) Balzani, V.; Credi, A.; Venturi, M. Photochemical Conversion of Solar Energy. *ChemSusChem* **2008**, *1* (1–2), 26–58.
- (15) Bloor, L. G.; Solarska, R.; Bienkowski, K.; Kulesza, P. J.; Augustynski, J.; Symes, M. D.; Cronin, L. Solar-Driven Water Oxidation and Decoupled Hydrogen Production Mediated by an Electron-Coupled-Proton Buffer. *J. Am. Chem. Soc.* **2016**, *138* (21), 6707–6710.
- (16) Cook, T. R.; Dogutan, D. K.; Reece, S. Y.; Surendranath, Y.; Teets, T. S.; Nocera, D. G. Solar Energy Supply and Storage for the Legacy and Nonlegacy Worlds. *Chem. Rev.* **2010**, *110* (11), 6474–6502.
- (17) Li, B.; Xu, Z. A Nonmetal Catalyst for Molecular Hydrogen Activation with Comparable Catalytic Hydrogenation Capability to Noble Metal Catalyst. *J. Am. Chem. Soc.* **2009**, *131* (45), 16380–16382.
- (18) Wesselbaum, S.; vom Stein, T.; Klankermayer, J.; Leitner, W. Hydrogenation of Carbon Dioxide to Methanol by Using a Homogeneous Ruthenium–Phosphine Catalyst. *Angew. Chem. Int. Ed.* **2012**, *51* (30), 7499–7502.
- (19) Schulz, H.; Beck, K.; Erich, E. Mechanism of the Fischer Tropsch Process. In *Studies in Surface Science and Catalysis*; Bibby, D. M., Chang, C. D., Howe, R. F., Yurchak, S., Eds.; Methane Conversion; Elsevier, 1988; Vol. 36, pp 457–471.
- (20) Turner, J. A. Sustainable Hydrogen Production. *Science* **2004**, *305* (5686), 972–974.

- (21) Gahleitner, G. Hydrogen from Renewable Electricity: An International Review of Power-to-Gas Pilot Plants for Stationary Applications. *Int. J. Hydrog. Energy* **2013**, *38* (5), 2039–2061.
- (22) Du, P.; Eisenberg, R. Catalysts Made of Earth-Abundant Elements (Co, Ni, Fe) for Water Splitting: Recent Progress and Future Challenges. *Energy Environ. Sci.* **2012**, *5* (3), 6012–6021.
- (23) Schiller, M. Hydrogen Energy Storage: The Holy Grail for Renewable Energy Grid Integration. *Fuel Cells Bull.* **2013**, *2013* (9), 12–15.
- (24) Kumari, S.; White, R. T.; Kumar, B.; Spurgeon, J. M. Solar Hydrogen Production from Seawater Vapor Electrolysis. *Energy Environ. Sci.* **2016**, *9* (5), 1725–1733.
- (25) Costentin, C.; Nocera, D. G. Self-Healing Catalysis in Water. *Proc. Natl. Acad. Sci.* **2017**, *114* (51), 13380–13384.
- (26) Merki, D.; Vrubel, H.; Rovelli, L.; Fierro, S.; Hu, X. Fe, Co, and Ni Ions Promote the Catalytic Activity of Amorphous Molybdenum Sulfide Films for Hydrogen Evolution. *Chem. Sci.* **2012**, *3* (8), 2515–2525.
- (27) Chen, H.; Sun, Z.; Liu, X.; Han, A.; Du, P. Cobalt–Salen Complexes as Catalyst Precursors for Electrocatalytic Water Oxidation at Low Overpotential. *J. Phys. Chem. C* **2015**, *119* (17), 8998–9004.
- (28) Zhong, D. K.; Gamelin, D. R. Photoelectrochemical Water Oxidation by Cobalt Catalyst (“Co–Pi”)/ α -Fe₂O₃ Composite Photoanodes: Oxygen Evolution and Resolution of a Kinetic Bottleneck. *J. Am. Chem. Soc.* **2010**, *132* (12), 4202–4207.
- (29) Siegbahn, P. E. M. Structures and Energetics for O₂ Formation in Photosystem II. *Acc. Chem. Res.* **2009**, *42* (12), 1871–1880.
- (30) Lu, Z.; Wang, H.; Kong, D.; Yan, K.; Hsu, P.-C.; Zheng, G.; Yao, H.; Liang, Z.; Sun, X.; Cui, Y. Electrochemical Tuning of Layered Lithium Transition Metal Oxides for Improvement of Oxygen Evolution Reaction. *Nat. Commun.* **2014**, *5*, 4345.

- (31) Wang, M.; Chen, L.; Sun, L. Recent Progress in Electrochemical Hydrogen Production with Earth-Abundant Metal Complexes as Catalysts. *Energy Environ. Sci.* **2012**, *5* (5), 6763–6778.
- (32) Yu, L.; Lin, J.; Zheng, M.; Chen, M.; Ding, Y. Homogeneous Electrocatalytic Water Oxidation at Neutral pH by a Robust Trinuclear Copper(II)-Substituted Polyoxometalate. *Chem. Commun.* **2018**, *54* (4), 354–357.
- (33) Faber, M. S.; Lukowski, M. A.; Ding, Q.; Kaiser, N. S.; Jin, S. Earth-Abundant Metal Pyrites (FeS₂, CoS₂, NiS₂, and Their Alloys) for Highly Efficient Hydrogen Evolution and Polysulfide Reduction Electrocatalysis. *J. Phys. Chem. C* **2014**, *118* (37), 21347–21356.
- (34) Vannucci, A. K.; Alibabaei, L.; Losego, M. D.; Concepcion, J. J.; Kalanyan, B.; Parsons, G. N.; Meyer, T. J. Crossing the Divide between Homogeneous and Heterogeneous Catalysis in Water Oxidation. *Proc. Natl. Acad. Sci. U. S. A.* **2013**, *110* (52), 20918–20922.
- (35) Fukuzumi, S.; Hong, D. Homogeneous versus Heterogeneous Catalysts in Water Oxidation. *Eur. J. Inorg. Chem.* **2014**, *2014* (4), 645–659.
- (36) Costentin, C.; Passard, G.; Savéant, J.-M. Benchmarking of Homogeneous Electrocatalysts: Overpotential, Turnover Frequency, Limiting Turnover Number. *J. Am. Chem. Soc.* **2015**, *137* (16), 5461–5467.
- (37) Bediako, D. K.; Solis, B. H.; Dogutan, D. K.; Roubelakis, M. M.; Maher, A. G.; Lee, C. H.; Chambers, M. B.; Hammes-Schiffer, S.; Nocera, D. G. Role of Pendant Proton Relays and Proton-Coupled Electron Transfer on the Hydrogen Evolution Reaction by Nickel Hangman Porphyrins. *Proc. Natl. Acad. Sci.* **2014**, *111* (42), 15001–15006.
- (38) Solis, B. H.; Hammes-Schiffer, S. Theoretical Analysis of Mechanistic Pathways for Hydrogen Evolution Catalyzed by Cobaloximes. *Inorg. Chem.* **2011**, *50* (21), 11252–11262.
- (39) Lee, Y.; Suntivich, J.; May, K. J.; Perry, E. E.; Shao-Horn, Y. Synthesis and Activities of Rutile IrO₂ and RuO₂ Nanoparticles for Oxygen Evolution in Acid and Alkaline Solutions. *J. Phys. Chem. Lett.* **2012**, *3* (3), 399–404.

- (40) Burke, L. D.; Murphy, O. J.; O'Neill, J. F.; Venkatesan, S. The Oxygen Electrode. Part 8.—Oxygen Evolution at Ruthenium Dioxide Anodes. *J. Chem. Soc. Faraday Trans. 1 Phys. Chem. Condens. Phases* **1977**, *73* (0), 1659–1671.
- (41) Thomsen, J. M.; Huang, D. L.; Crabtree, R. H.; Brudvig, G. W. Iridium-Based Complexes for Water Oxidation. *Dalton Trans.* **2015**, *44* (28), 12452–12472.
- (42) McKone, J. R.; Sadtler, B. F.; Werlang, C. A.; Lewis, N. S.; Gray, H. B. Ni–Mo Nanopowders for Efficient Electrochemical Hydrogen Evolution. *ACS Catal.* **2013**, *3* (2), 166–169.
- (43) Shen, Y.; Zhou, Y.; Wang, D.; Wu, X.; Li, J.; Xi, J. Nickel–Copper Alloy Encapsulated in Graphitic Carbon Shells as Electrocatalysts for Hydrogen Evolution Reaction. *Adv. Energy Mater.* **2018**, *8* (2), 1701759.
- (44) Hinnemann, B.; Moses, P. G.; Bonde, J.; Jørgensen, K. P.; Nielsen, J. H.; Horch, S.; Chorkendorff, I.; Nørskov, J. K. Biomimetic Hydrogen Evolution: MoS₂ Nanoparticles as Catalyst for Hydrogen Evolution. *J. Am. Chem. Soc.* **2005**, *127* (15), 5308–5309.
- (45) Jaramillo, T. F.; Jørgensen, K. P.; Bonde, J.; Nielsen, J. H.; Horch, S.; Chorkendorff, I. Identification of Active Edge Sites for Electrochemical H₂ Evolution from MoS₂ Nanocatalysts. *Science* **2007**, *317* (5834), 100–102.
- (46) Merki, D.; Hu, X. Recent Developments of Molybdenum and Tungsten Sulfides as Hydrogen Evolution Catalysts. *Energy Environ. Sci.* **2011**, *4* (10), 3878–3888.
- (47) Nolan, H.; McEvoy, N.; O'Brien, M.; C. Berner, N.; Yim, C.; Hallam, T.; R. McDonald, A.; S. Duesberg, G. Molybdenum Disulfide/Pyrolytic Carbon Hybrid Electrodes for Scalable Hydrogen Evolution. *Nanoscale* **2014**, *6* (14), 8185–8191.
- (48) Yang, Y.; Zhang, K.; Lin, H.; Li, X.; Chan, H. C.; Yang, L.; Gao, Q. MoS₂–Ni₃S₂ Heteronanorods as Efficient and Stable Bifunctional Electrocatalysts for Overall Water Splitting. *ACS Catal.* **2017**, *7* (4), 2357–2366.

- (49) Callejas, J. F.; Read, C. G.; Roske, C. W.; Lewis, N. S.; Schaak, R. E. Synthesis, Characterization, and Properties of Metal Phosphide Catalysts for the Hydrogen-Evolution Reaction. *Chem. Mater.* **2016**, *28* (17), 6017–6044.
- (50) Popczun, E. J.; McKone, J. R.; Read, C. G.; Biacchi, A. J.; Wilttrout, A. M.; Lewis, N. S.; Schaak, R. E. Nanostructured Nickel Phosphide as an Electrocatalyst for the Hydrogen Evolution Reaction. *J. Am. Chem. Soc.* **2013**, *135* (25), 9267–9270.
- (51) Wang, S.; Zhang, L.; Li, X.; Li, C.; Zhang, R.; Zhang, Y.; Zhu, H. Sponge-like Nickel Phosphide–Carbon Nanotube Hybrid Electrodes for Efficient Hydrogen Evolution over a Wide PH Range. *Nano Res.* **2016**, 1–11.
- (52) Callejas, J. F.; Read, C. G.; Popczun, E. J.; McEnaney, J. M.; Schaak, R. E. Nanostructured Co₂P Electrocatalyst for the Hydrogen Evolution Reaction and Direct Comparison with Morphologically Equivalent CoP. *Chem. Mater.* **2015**, *27* (10), 3769–3774.
- (53) Feng, L.; Vrabel, H.; Bensimon, M.; Hu, X. Easily-Prepared Dinickel Phosphide (Ni₂P) Nanoparticles as an Efficient and Robust Electrocatalyst for Hydrogen Evolution. *Phys. Chem. Chem. Phys.* **2014**, *16* (13), 5917–5921.
- (54) Song, F.; Bai, L.; Moysiadou, A.; Lee, S.; Hu, C.; Liardet, L.; Hu, X. Transition Metal Oxides as Electrocatalysts for the Oxygen Evolution Reaction in Alkaline Solutions: An Application-Inspired Renaissance. *J. Am. Chem. Soc.* **2018**, *140* (25), 7748–7759.
- (55) Nayak, A. K.; Verma, M.; Sohn, Y.; Deshpande, P. A.; Pradhan, D. Highly Active Tungsten Oxide Nanoplate Electrocatalysts for the Hydrogen Evolution Reaction in Acidic and Near Neutral Electrolytes. *ACS Omega* **2017**, *2* (10), 7039–7047.
- (56) Datta, R. S.; Haque, F.; Mohiuddin, M.; Carey, B. J.; Syed, N.; Zavabeti, A.; Zhang, B.; Khan, H.; Berean, K. J.; Ou, J. Z.; et al. Highly Active Two Dimensional α -MoO_{3-x} for the Electrocatalytic Hydrogen Evolution Reaction. *J. Mater. Chem. A* **2017**, *5* (46), 24223–24231.

- (57) Chen, Z.; Cummins, D.; Reinecke, B. N.; Clark, E.; Sunkara, M. K.; Jaramillo, T. F. Core–Shell MoO₃–MoS₂ Nanowires for Hydrogen Evolution: A Functional Design for Electrocatalytic Materials. *Nano Lett.* **2011**, *11* (10), 4168–4175.
- (58) Wang, S.; Wang, J.; Zhu, M.; Bao, X.; Xiao, B.; Su, D.; Li, H.; Wang, Y. Molybdenum-Carbide-Modified Nitrogen-Doped Carbon Vesicle Encapsulating Nickel Nanoparticles: A Highly Efficient, Low-Cost Catalyst for Hydrogen Evolution Reaction. *J. Am. Chem. Soc.* **2015**, *137* (50), 15753–15759.
- (59) Lu, F.; Zhou, M.; Zhou, Y.; Zeng, X. First-Row Transition Metal Based Catalysts for the Oxygen Evolution Reaction under Alkaline Conditions: Basic Principles and Recent Advances. *Small* **2017**, *13* (45), 1701931.
- (60) Amiin, I. S.; Pu, Z.; Liu, X.; Owusu, K. A.; Monestel, H. G. R.; Boakye, F. O.; Zhang, H.; Mu, S. Multifunctional Mo–N/C@MoS₂ Electrocatalysts for HER, OER, ORR, and Zn–Air Batteries. *Adv. Funct. Mater.* **2017**, *27* (44), 1702300.
- (61) Patra, B. C.; Khilari, S.; Manna, R. N.; Mondal, S.; Pradhan, D.; Pradhan, A.; Bhaumik, A. A Metal-Free Covalent Organic Polymer for Electrocatalytic Hydrogen Evolution. *ACS Catal.* **2017**, *7* (9), 6120–6127.
- (62) Yap, C. P.; Poh, H. T.; Fan, W. Y. Metal-Free Catalytic Hydrogen Production from a Polymethylhydrosilane–Water Mixture. *RSC Adv.* **2016**, *6* (7), 5903–5906.
- (63) Zheng, Y.; Jiao, Y.; Zhu, Y.; Li, L. H.; Han, Y.; Chen, Y.; Du, A.; Jaroniec, M.; Qiao, S. Z. Hydrogen Evolution by a Metal-Free Electrocatalyst. *Nat. Commun.* **2014**, *5*, ncomms4783.
- (64) Kong, X.-K.; Chen, C.-L.; Chen, Q.-W. Doped Graphene for Metal-Free Catalysis. *Chem. Soc. Rev.* **2014**, *43* (8), 2841–2857.
- (65) Shateesh, B.; Markad, G. B.; Haram, S. K. Nitrogen Doped Graphene Oxides as an Efficient Electrocatalyst for the Hydrogen Evolution Reaction; Composition Based Electrode Investigation. *Electrochimica Acta* **2016**, *200*, 53–58.

- (66) Sathe, B. R.; Zou, X.; Asefa, T. Metal-Free B-Doped Graphene with Efficient Electrocatalytic Activity for Hydrogen Evolution Reaction. *Catal. Sci. Technol.* **2014**, *4* (7), 2023–2030.
- (67) Li, T.; Tang, D.; Wang, M.; Song, Q.; Li, C. M. Ionic Liquid Originated Synthesis of N,P-Doped Graphene for Hydrogen Evolution Reaction. *ChemistrySelect* **2018**, *3* (24), 6814–6820.
- (68) Lee, C. H.; Dogutan, D. K.; Nocera, D. G. Hydrogen Generation by Hangman Metalloporphyrins. *J. Am. Chem. Soc.* **2011**, *133* (23), 8775–8777.
- (69) Solis, B. H.; Maher, A. G.; Dogutan, D. K.; Nocera, D. G.; Hammes-Schiffer, S. Nickel Phlorin Intermediate Formed by Proton-Coupled Electron Transfer in Hydrogen Evolution Mechanism. *Proc. Natl. Acad. Sci.* **2016**, *113* (3), 485–492.
- (70) Mondal, B.; Sengupta, K.; Rana, A.; Mahammed, A.; Botoshansky, M.; Dey, S. G.; Gross, Z.; Dey, A. Cobalt Corrole Catalyst for Efficient Hydrogen Evolution Reaction from H₂O under Ambient Conditions: Reactivity, Spectroscopy, and Density Functional Theory Calculations. *Inorg. Chem.* **2013**, *52* (6), 3381–3387.
- (71) Zhang, W.; Lai, W.; Cao, R. Energy-Related Small Molecule Activation Reactions: Oxygen Reduction and Hydrogen and Oxygen Evolution Reactions Catalyzed by Porphyrin- and Corrole-Based Systems. *Chem. Rev.* **2017**, *117* (4), 3717–3797.
- (72) Hu, X.; Brunschwig, B. S.; Peters, J. C. Electrocatalytic Hydrogen Evolution at Low Overpotentials by Cobalt Macrocyclic Glyoxime and Tetraimine Complexes. *J. Am. Chem. Soc.* **2007**, *129* (29), 8988–8998.
- (73) McCrory, C. C. L.; Uyeda, C.; Peters, J. C. Electrocatalytic Hydrogen Evolution in Acidic Water with Molecular Cobalt Tetraazamacrocycles. *J. Am. Chem. Soc.* **2012**, *134* (6), 3164–3170.
- (74) Maher, A. G.; Passard, G.; Dogutan, D. K.; Halbach, R. L.; Anderson, B. L.; Gagliardi, C. J.; Taniguchi, M.; Lindsey, J. S.; Nocera, D. G. Hydrogen Evolution Catalysis by a Sparsely Substituted Cobalt Chlorin. *ACS Catal.* **2017**, *7* (5), 3597–3606.

- (75) Fihri, A.; Artero, V.; Razavet, M.; Baffert, C.; Leibl, W.; Fontecave, M. Cobaloxime-Based Photocatalytic Devices for Hydrogen Production. *Angew. Chem. Int. Ed Engl.* **2008**, *47* (3), 564–567.
- (76) Valdez, C. N.; Dempsey, J. L.; Brunschwig, B. S.; Winkler, J. R.; Gray, H. B. Catalytic Hydrogen Evolution from a Covalently Linked Dicobaloxime. *Proc. Natl. Acad. Sci.* **2012**, *109* (39), 15589–15593.
- (77) Hu, X.; M. Cossairt, B.; S. Brunschwig, B.; S. Lewis, N.; C. Peters, J. Electrocatalytic Hydrogen Evolution by Cobalt Difluoroboryl-Diglyoximate Complexes. *Chem. Commun.* **2005**, *0* (37), 4723–4725.
- (78) Jurss, J. W.; Khnayzer, R. S.; Panetier, J. A.; Roz, K. A. E.; Nichols, E. M.; Head-Gordon, M.; Long, J. R.; Castellano, F. N.; Chang, C. J. Bioinspired Design of Redox-Active Ligands for Multielectron Catalysis: Effects of Positioning Pyrazine Reservoirs on Cobalt for Electro- and Photocatalytic Generation of Hydrogen from Water. *Chem. Sci.* **2015**, *6* (8), 4954–4972.
- (79) Canaguier, S.; Fontecave, M.; Artero, V. Cp*—Ruthenium–Nickel-Based H₂-Evolving Electrocatalysts as Bio-Inspired Models of NiFe Hydrogenases. *Eur. J. Inorg. Chem.* **2011**, *2011* (7), 1094–1099.
- (80) Sherman, B. D.; Sheridan, M. V.; Wee, K.-R.; Song, N.; Dares, C. J.; Fang, Z.; Tamaki, Y.; Nayak, A.; Meyer, T. J. Analysis of Homogeneous Water Oxidation Catalysis with Collector–Generator Cells. *Inorg. Chem.* **2016**, *55* (2), 512–517.
- (81) Lash, T. D. Origin of Aromatic Character in Porphyrinoid Systems. *J. Porphyr. Phthalocyanines* **2011**, *15* (11n12), 1093–1115.
- (82) Berg, H. J. E. FALK, Porphyrins and Metalloporphyrins. Their General, Physical and Coordination Chemistry and Laboratory Methods. 1. Aufl. 266 S., 21 Abb., 36 Tab. Amsterdam 1964: Elsevier Publ. Comp. DM 42.—. *Z. Für Allg. Mikrobiol.* **1964**, *4* (5), 398–398.

- (83) Aronoff, S. The Absorption Spectra of Chlorophyll and Related Compounds. *Chem. Rev.* **1950**, *47* (2), 175–195.
- (84) Muniyappan, R. Porphyrins in Petroleum. *J. Chem. Educ.* **1955**, *32* (5), 277.
- (85) Miralamov, G. F. Preparation of Vanadyl Porphyrin Complexes from a Metal-Porphyrin Petroleum Concentrate and Study of Their Catalytic Activity. *Pet. Chem.* **2006**, *46* (6), 447–449.
- (86) Shelnutt, J. A.; Rousseau, D. L.; Dethmers, J. K.; Margolias, E. Protein Influences on Porphyrin Structure in Cytochrome c: Evidence from Raman Difference Spectroscopy. *Biochemistry* **1981**, *20* (22), 6485–6497.
- (87) Lindsey, J. S.; Hsu, H. C.; Schreiman, I. C. Synthesis of Tetraphenylporphyrins under Very Mild Conditions. *Tetrahedron Lett.* **1986**, *27* (41), 4969–4970.
- (88) Rothmund, P. A New Porphyrin Synthesis. The Synthesis of Porphin1. *J. Am. Chem. Soc.* **1936**, *58* (4), 625–627.
- (89) Shy, H.; Mackin, P.; Orvieto, A. S.; Gharbharan, D.; Peterson, G. R.; Bampos, N.; Hamilton, T. D. Two-Step Mechanochemical Synthesis of Porphyrins. *Faraday Discuss.* **2014**, *170*, 59–69.
- (90) Rogers, J. E.; Nguyen, K. A.; Hufnagle, D. C.; McLean, D. G.; Su, W.; Gossett, K. M.; Burke, A. R.; Vinogradov, S. A.; Pachter, R.; Fleitz, P. A. Observation and Interpretation of Annulated Porphyrins: Studies on the Photophysical Properties of Meso-Tetraphenylmetalloporphyrins. *J. Phys. Chem. A* **2003**, *107* (51), 11331–11339.
- (91) Minaev, B.; Ågren, H. Theoretical DFT Study of Phosphorescence from Porphyrins. *Chem. Phys.* **2005**, *315* (3), 215–239.
- (92) Ding, Y.; Zhu, W.-H.; Xie, Y. Development of Ion Chemosensors Based on Porphyrin Analogues. *Chem. Rev.* **2017**, *117* (4), 2203–2256.
- (93) Abe, T.; Taguchi, F.; Imaya, H.; Zhao, F.; Zhang, J.; Kaneko, M. Highly Active Electrocatalysis by Cobalt Tetraphenylporphyrin Incorporated in a Nafion Membrane for Proton Reduction. *Polym. Adv. Technol.* **1998**, *9* (9), 559–562.

- (94) Margarit, C. G.; Schnedermann, C.; Asimow, N. G.; Nocera, D. G. Carbon Dioxide Reduction by Iron Hexamethine Porphyrins. *Organometallics* **2018**.
- (95) Ma, W.; Yu, P.; Ohsaka, T.; Mao, L. An Efficient Electrocatalyst for Oxygen Reduction Reaction Derived from a Co-Porphyrin-Based Covalent Organic Framework. *Electrochem. Commun.* **2015**, *52*, 53–57.
- (96) Bhugun, I.; Lexa, D.; Savéant, J.-M. Homogeneous Catalysis of Electrochemical Hydrogen Evolution by Iron(0) Porphyrins. *J. Am. Chem. Soc.* **1996**, *118* (16), 3982–3983.
- (97) Jia, H.; Yao, Y.; Gao, Y.; Lu, D.; Du, P. Pyrolyzed Cobalt Porphyrin-Based Conjugated Mesoporous Polymers as Bifunctional Catalysts for Hydrogen Production and Oxygen Evolution in Water. *Chem. Commun.* **2016**, *52* (92), 13483–13486.
- (98) Cui, S.; Qian, M.; Liu, X.; Sun, Z.; Du, P. A Copper Porphyrin-Based Conjugated Mesoporous Polymer-Derived Bifunctional Electrocatalyst for Hydrogen and Oxygen Evolution. *ChemSusChem* **2016**, *9* (17), 2365–2373.
- (99) Blanchard, R.; Martin, V.; Mantoux, A.; Chatenet, M. Cobalt Porphyrin and Salcomine as Novel Redox Shuttle Species to Enhance the Oxygen Evolution Reaction in LiO₂ Batteries. *Electrochimica Acta* **2018**, *261*, 384–393.
- (100) Han, Y.; Wu, Y.; Lai, W.; Cao, R. Electrocatalytic Water Oxidation by a Water-Soluble Nickel Porphyrin Complex at Neutral pH with Low Overpotential. *Inorg. Chem.* **2015**, *54* (11), 5604–5613.
- (101) Cao, R. Hydrogen and Oxygen Evolution Reactions Catalyzed By Single Site Metal Porphyrins and Corroles. *Meet. Abstr.* **2018**, *MA2018-01* (12), 967–967.
- (102) Yamazaki, S. Metalloporphyrins and Related Metallomacrocycles as Electrocatalysts for Use in Polymer Electrolyte Fuel Cells and Water Electrolyzers. *Coord. Chem. Rev.* **2018**, *373*, 148–166.
- (103) Roubelakis, M. M.; Bediako, D. K.; Dogutan, D. K.; Nocera, D. G. Proton-Coupled Electron Transfer Kinetics for the Hydrogen Evolution Reaction of Hexamethine Porphyrins. *Energy Environ. Sci.* **2012**, *5* (7), 7737–7740.

- (104) Manton, J. C.; Hidalgo, D.; Frayne, L.; Brandon, M. P.; Vos, J. G.; Pryce, M. T. Electrocatalytic Hydrogen Evolution Using Metal-Free Porphyrins. *Int. J. Hydrog. Energy* **2018**.
- (105) Bullock, R. M.; Das, A. K.; Appel, A. M. Surface Immobilization of Molecular Electrocatalysts for Energy Conversion. *Chem. – Eur. J.* **2017**, *23* (32), 7626–7641.
- (106) Kent, C. A.; Concepcion, J. J.; Dares, C. J.; Torelli, D. A.; Rieth, A. J.; Miller, A. S.; Hoertz, P. G.; Meyer, T. J. Water Oxidation and Oxygen Monitoring by Cobalt-Modified Fluorine-Doped Tin Oxide Electrodes. *J. Am. Chem. Soc.* **2013**, *135* (23), 8432–8435.
- (107) Liu, H.; Wang, A.; Sun, Q.; Wang, T.; Zeng, H.; Liu, H.; Wang, A.; Sun, Q.; Wang, T.; Zeng, H. Cu Nanoparticles/Fluorine-Doped Tin Oxide (FTO) Nanocomposites for Photocatalytic H₂ Evolution under Visible Light Irradiation. *Catalysts* **2017**, *7* (12), 385.
- (108) Ma, T. Y.; Dai, S.; Qiao, S. Z. Self-Supported Electrocatalysts for Advanced Energy Conversion Processes. *Mater. Today* **2016**, *19* (5), 265–273.
- (109) Tang, H.; Yin, H.; Wang, J.; Yang, N.; Wang, D.; Tang, Z. Molecular Architecture of Cobalt Porphyrin Multilayers on Reduced Graphene Oxide Sheets for High-Performance Oxygen Reduction Reaction. *Angew. Chem. Int. Ed.* **2013**, *52* (21), 5585–5589.
- (110) Kumar, A.; Xu, Q. Two-Dimensional Layered Materials as Catalyst Supports. *ChemNanoMat* **2018**, *4* (1), 28–40.
- (111) Mansor, N.; Miller, T. S.; Dedigama, I.; Jorge, A. B.; Jia, J.; Brázdová, V.; Mattevi, C.; Gibbs, C.; Hodgson, D.; Shearing, P. R.; et al. Graphitic Carbon Nitride as a Catalyst Support in Fuel Cells and Electrolyzers. *Electrochimica Acta* **2016**, *222*, 44–57.
- (112) Yang, J.; Fujigaya, T.; Nakashima, N. Decorating Unoxidized-Carbon Nanotubes with Homogeneous Ni-Co Spinel Nanocrystals Show Superior Performance for Oxygen Evolution/Reduction Reactions. *Sci. Rep.* **2017**, *7*.
- (113) Johnson, B. A.; Bhunia, A.; Ott, S. Electrocatalytic Water Oxidation by a Molecular Catalyst Incorporated into a Metal–Organic Framework Thin Film. *Dalton Trans.* **2017**, *46* (5), 1382–1388.

- (114) Downes, C. A.; Marinescu, S. C. Understanding Variability in the Hydrogen Evolution Activity of a Cobalt Anthracenetetrathiolate Coordination Polymer. *ACS Catal.* **2017**, *7* (12), 8605–8612.
- (115) Mukherjee, G.; Thote, J.; Aiyappa, H. B.; Kandambeth, S.; Banerjee, S.; Vanka, K.; Banerjee, R. A Porous Porphyrin Organic Polymer (PPOP) for Visible Light Triggered Hydrogen Production. *Chem. Commun.* **2017**, *53* (32), 4461–4464.
- (116) Grass, V.; Lexa, D.; Savéant, J.-M. Electrochemical Generation of Rhodium Porphyrin Hydrides. Catalysis of Hydrogen Evolution. *J. Am. Chem. Soc.* **1997**, *119* (32), 7526–7532.
- (117) Solis, B. H.; Hammes-Schiffer, S. Proton-Coupled Electron Transfer in Molecular Electrocatalysis: Theoretical Methods and Design Principles. *Inorg. Chem.* **2014**, *53* (13), 6427–6443.
- (118) Collman, J. P.; Wagenknecht, P. S.; Lewis, N. S. Hydride Transfer and Dihydrogen Elimination from Osmium and Ruthenium Metalloporphyrin Hydrides: Model Processes for Hydrogenase Enzymes and the Hydrogen Electrode Reaction. *J. Am. Chem. Soc.* **1992**, *114* (14), 5665–5673.
- (119) Marinescu, S. C.; Winkler, J. R.; Gray, H. B. Molecular Mechanisms of Cobalt-Catalyzed Hydrogen Evolution. *Proc. Natl. Acad. Sci.* **2012**, *109* (38), 15127–15131.
- (120) Fonda, H. N.; Gilbert, J. V.; Cormier, R. A.; Sprague, J. R.; Kamioka, K.; Connolly, J. S. Spectroscopic, Photophysical, and Redox Properties of Some Meso-Substituted Free-Base Porphyrins. *J. Phys. Chem.* **1993**, *97* (27), 7024–7033.
- (121) Handbook of Porphyrin Science (Volumes 31 – 35)
<http://www.worldscientific.com/worldscibooks/10.1142/8560> (accessed Jan 24, 2017).
- (122) Aronoff, S. Perchloric Acid Titrations of Porphyrins in Nitrobenzene. *J. Phys. Chem.* **1958**, *62* (4), 428–431.
- (123) Hibbert, F.; Hunte, K. P. P. Kinetic and Equilibrium Studies of the Protonation of Meso-Tetraphenylporphyrin in Dimethyl Sulphoxide–Water. *J. Chem. Soc. Perkin Trans. 2* **1977**, *0* (12), 1624–1628.

- (124) Rountree, E. S.; McCarthy, B. D.; Eisenhart, T. T.; Dempsey, J. L. Evaluation of Homogeneous Electrocatalysts by Cyclic Voltammetry. *Inorg. Chem.* **2014**, *53* (19), 9983–10002.
- (125) Elgrishi, N.; Chambers, M. B.; Fontecave, M. Turning It off! Disfavouring Hydrogen Evolution to Enhance Selectivity for CO Production during Homogeneous CO₂ Reduction by Cobalt–Terpyridine Complexes †Electronic Supplementary Information (ESI) Available. See DOI: 10.1039/C4sc03766a Click Here for Additional Data File. *Chem. Sci.* **2015**, *6* (4), 2522–2531.
- (126) Becke, A. D. Density-functional Thermochemistry. III. The Role of Exact Exchange. *J. Chem. Phys.* **1993**, *98* (7), 5648–5652.
- (127) Lee, C.; Yang, W.; Parr, R. G. Development of the Colle-Salvetti Correlation-Energy Formula into a Functional of the Electron Density. *Phys. Rev. B* **1988**, *37* (2), 785–789.
- (128) Frisch, M. J.; Pople, J. A.; Binkley, J. S. Self-consistent Molecular Orbital Methods 25. Supplementary Functions for Gaussian Basis Sets. *J. Chem. Phys.* **1984**, *80* (7), 3265–3269.
- (129) Hariharan, P. C.; Pople, J. A. The Influence of Polarization Functions on Molecular Orbital Hydrogenation Energies. *Theor. Chim. Acta* **1973**, *28* (3), 213–222.
- (130) Frisch, M. J.; Trucks, G. W.; Schlegel, H. B.; Scuseria, G. E.; Robb, M. A.; Cheeseman, J. R.; Scalmani, G.; Barone, V.; Mennucci, B.; Petersson, G. A.; Nakatsuji, H.; Caricato, M.; Li, X.; Hratchian, H. P.; Izmaylov, A. F.; Bloino, J.; Zheng, G.; Sonnenberg, J. L.; Hada, M.; Ehara, M.; Toyota, K.; Fukuda, R.; Hasegawa, J.; Ishida, M.; Nakajima, T.; Honda, Y.; Kitao, O.; Nakai, H.; Vreven, T.; Montgomery, J. A., Jr.; Peralta, J. E.; Ogliaro, F.; Bearpark, M.; Heyd, J. J.; Brothers, E.; Kudin, K. N.; Staroverov, V. N.; Kobayashi, R.; Normand, J.; Raghavachari, K.; Rendell, A.; Burant, J. C.; Iyengar, S. S.; Tomasi, J.; Cossi, M.; Rega, N.; Millam, J. M.; Klene, M.; Knox, J. E.; Cross, J. B.; Bakken, V.; Adamo, C.; Jaramillo, J.; Gomperts, R.; Stratmann, R. E.; Yazyev, O.; Austin, A. J.; Cammi, R.; Pomelli, C.; Ochterski, J. W.; Martin, R. L.; Morokuma, K.; Zakrzewski, V. G.; Voth, G. A.; Salvador, P.; Dannenberg, J. J.; Dapprich, S.; Daniels, A. D.; Farkas, Ö.; Foresman, J.

- B.; Ortiz, J. V.; Cioslowski, J.; Fox, D. J. Gaussian 09, Revision C.01, Gaussian, Inc., Wallingford CT, 2010.
- (131) Cammi, R.; Mennucci, B.; Tomasi, J. An Attempt To Bridge the Gap between Computation and Experiment for Nonlinear Optical Properties: Macroscopic Susceptibilities in Solution. *J. Phys. Chem. A* **2000**, *104* (20), 4690–4698.
- (132) Cammi, R.; Mennucci, B.; Tomasi, J. On the Calculation of Local Field Factors for Microscopic Static Hyperpolarizabilities of Molecules in Solution with the Aid of Quantum-Mechanical Methods. *J. Phys. Chem. A* **1998**, *102* (5), 870–875.
- (133) Marenich, A. V.; Cramer, C. J.; Truhlar, D. G. Universal Solvation Model Based on Solute Electron Density and on a Continuum Model of the Solvent Defined by the Bulk Dielectric Constant and Atomic Surface Tensions. *J. Phys. Chem. B* **2009**, *113* (18), 6378–6396.
- (134) Solis, B. H.; Hammes-Schiffer, S. Substituent Effects on Cobalt Diglyoxime Catalysts for Hydrogen Evolution. *J. Am. Chem. Soc.* **2011**, *133* (47), 19036–19039.
- (135) Solis, B. H.; Maher, A. G.; Honda, T.; Powers, D. C.; Nocera, D. G.; Hammes-Schiffer, S. Theoretical Analysis of Cobalt Hangman Porphyrins: Ligand Dearomatization and Mechanistic Implications for Hydrogen Evolution. *ACS Catal.* **2014**, *4* (12), 4516–4526.
- (136) Tang, H.; Hall, M. B. Biomimetics of [NiFe]-Hydrogenase: Nickel- or Iron-Centered Proton Reduction Catalysis? *J. Am. Chem. Soc.* **2017**, *139* (49), 18065–18070.
- (137) Aidas, K.; Lanevskij, K.; Kubilius, R.; Juška, L.; Petkevičius, D.; Japertas, P. Aqueous Acidities of Primary Benzenesulfonamides: Quantum Chemical Predictions Based on Density Functional Theory and SMD. *J. Comput. Chem.* **2015**, *36* (29), 2158–2167.
- (138) Fernandez, L. E.; Horvath, S.; Hammes-Schiffer, S. Theoretical Analysis of the Sequential Proton-Coupled Electron Transfer Mechanisms for H₂ Oxidation and Production Pathways Catalyzed by Nickel Molecular Electrocatalysts. *J. Phys. Chem. C* **2012**, *116* (4), 3171–3180.

- (139) Ho, J.; Coote, M. L. A Universal Approach for Continuum Solvent PKa Calculations: Are We There Yet? *Theor. Chem. Acc.* **2009**, *125* (1), 3.
- (140) Hansch, C.; Leo, A.; Taft, R. W. A Survey of Hammett Substituent Constants and Resonance and Field Parameters. *Chem. Rev.* **1991**, *91* (2), 165–195.
- (141) Roberts, J. A. S.; Bullock, R. M. Direct Determination of Equilibrium Potentials for Hydrogen Oxidation/Production by Open Circuit Potential Measurements in Acetonitrile. *Inorg. Chem.* **2013**, *52* (7), 3823–3835.
- (142) Appel, A. M.; Helm, M. L. Determining the Overpotential for a Molecular Electrocatalyst. *ACS Catal.* **2014**, *4* (2), 630–633.
- (143) Beyene, B. B.; Mane, S. B.; Hung, C.-H. Highly Efficient Electrocatalytic Hydrogen Evolution from Neutral Aqueous Solution by a Water-Soluble Anionic Cobalt(II) Porphyrin. *Chem. Commun.* **2015**, *51* (81), 15067–15070.
- (144) Hod, I.; Sampson, M. D.; Deria, P.; Kubiak, C. P.; Farha, O. K.; Hupp, J. T. Fe-Porphyrin-Based Metal–Organic Framework Films as High-Surface Concentration, Heterogeneous Catalysts for Electrochemical Reduction of CO₂. *ACS Catal.* **2015**, *5* (11), 6302–6309.
- (145) Wu, Z.-S.; Chen, L.; Liu, J.; Parvez, K.; Liang, H.; Shu, J.; Sachdev, H.; Graf, R.; Feng, X.; Müllen, K. High-Performance Electrocatalysts for Oxygen Reduction Derived from Cobalt Porphyrin-Based Conjugated Mesoporous Polymers. *Adv. Mater.* **2014**, *26* (9), 1450–1455.
- (146) Brüller, S.; Liang, H.-W.; Kramm, U. I.; Krumpfer, J. W.; Feng, X.; Müllen, K. Bimetallic Porous Porphyrin Polymer-Derived Non-Precious Metal Electrocatalysts for Oxygen Reduction Reactions. *J. Mater. Chem. A* **2015**, *3* (47), 23799–23808.
- (147) Chen, L.; Yang, Y.; Jiang, D. CMPs as Scaffolds for Constructing Porous Catalytic Frameworks: A Built-in Heterogeneous Catalyst with High Activity and Selectivity Based on Nanoporous Metalloporphyrin Polymers. *J. Am. Chem. Soc.* **2010**, *132* (26), 9138–9143.

- (148) Chen, A.; Zhang, Y.; Chen, J.; Chen, L.; Yu, Y. Metalloporphyrin-Based Organic Polymers for Carbon Dioxide Fixation to Cyclic Carbonate. *J. Mater. Chem. A* **2015**, *3* (18), 9807–9816.
- (149) Oveisi, A. R.; Zhang, K.; Khorramabadi-zad, A.; Farha, O. K.; Hupp, J. T. Stable and Catalytically Active Iron Porphyrin-Based Porous Organic Polymer: Activity as Both a Redox and Lewis Acid Catalyst. *Sci. Rep.* **2015**, *5*.
- (150) Shahroosvand, H.; Zakavi, S.; Sousaraei, A.; Mohajerani, E.; Mahmoudi, M. Unusual Near-White Electroluminescence of Light Emitting Diodes Based on Saddle-Shaped Porphyrins. *Dalton Trans.* **2015**, *44* (18), 8364–8368.
- (151) Kleingardner, J. G.; Kandemir, B.; Bren, K. L. Hydrogen Evolution from Neutral Water under Aerobic Conditions Catalyzed by Cobalt Microperoxidase-11. *J. Am. Chem. Soc.* **2014**, *136* (1), 4–7.
- (152) La, D. D.; Thi, H. P. N.; Kim, Y. S.; Rananaware, A.; Bhosale, S. V. Facile Fabrication of Cu(II)-Porphyrin MOF Thin Films from Tetrakis(4-Carboxyphenyl)Porphyrin and Cu(OH)₂ Nanoneedle Array. *Appl. Surf. Sci.* **2017**, *424*, 145–150.
- (153) Park, J.; Jiang, Q.; Feng, D.; Mao, L.; Zhou, H.-C. Size-Controlled Synthesis of Porphyrinic Metal–Organic Framework and Functionalization for Targeted Photodynamic Therapy. *J. Am. Chem. Soc.* **2016**, *138* (10), 3518–3525.
- (154) Liu, G.; Wang, Y.; Shen, C.; Ju, Z.; Yuan, D. A Facile Synthesis of Microporous Organic Polymers for Efficient Gas Storage and Separation. *J. Mater. Chem. A* **2015**, *3* (6), 3051–3058.
- (155) Yao, S.; Yang, X.; Yu, M.; Zhang, Y.; Jiang, J.-X. High Surface Area Hypercrosslinked Microporous Organic Polymer Networks Based on Tetraphenylethylene for CO₂ Capture. *J. Mater. Chem. A* **2014**, *2* (21), 8054–8059.
- (156) Liu, Y.; Wu, S.; Wang, G.; Yu, G.; Guan, J.; Pan, C.; Wang, Z. Control of Porosity of Novel Carbazole-Modified Polytriazine Frameworks for Highly Selective Separation of CO₂–N₂. *J. Mater. Chem. A* **2014**, *2* (21), 7795–7801.

- (157) Chen, L.; Yang, Y.; Guo, Z.; Jiang, D. Highly Efficient Activation of Molecular Oxygen with Nanoporous Metalloporphyrin Frameworks in Heterogeneous Systems. *Adv. Mater.* **2011**, *23* (28), 3149–3154.
- (158) Bellezza, F.; Cipiciani, A.; Costantino, U.; Negozio, M. E. Zirconium Phosphate and Modified Zirconium Phosphates as Supports of Lipase. Preparation of the Composites and Activity of the Supported Enzyme. *Langmuir* **2002**, *18* (23), 8737–8742.
- (159) Alberti, G. Syntheses, Crystalline Structure, and Ion-Exchange Properties of Insoluble Acid Salts of Tetravalent Metals and Their Salt Forms. *Acc. Chem. Res.* **1978**, *11* (4), 163–170.
- (160) Troup, J. M.; Clearfield, A. Mechanism of Ion Exchange in Zirconium Phosphates. 20. Refinement of the Crystal Structure of α -Zirconium Phosphate. *Inorg. Chem.* **1977**, *16* (12), 3311–3314.
- (161) Martí, A. A.; Colón, J. L. Direct Ion Exchange of Tris(2,2'-Bipyridine)Ruthenium(II) into an α -Zirconium Phosphate Framework. *Inorg. Chem.* **2003**, *42* (9), 2830–2832.
- (162) Alberti, G.; Costantino, U.; Gill, J. S. Crystalline Insoluble Acid Salts of Tetravalent Metals—XXIII: Preparation and Main Ion Exchange Properties of Highly Hydrated Zirconium Bis Monohydrogen Orthophosphates. *J. Inorg. Nucl. Chem.* **1976**, *38* (9), 1733–1738.
- (163) Sanchez, J.; Ramos-Garcés, M. V.; Narkeviciute, I.; Colón, J. L.; Jaramillo, T. F. Transition Metal-Modified Zirconium Phosphate Electrocatalysts for the Oxygen Evolution Reaction. *Catalysts* **2017**, *7* (5), 132.
- (164) Rao, K. N.; Sridhar, A.; Lee, A. F.; Tavener, S. J.; Young, N. A.; Wilson, K. Zirconium Phosphate Supported Tungsten Oxide Solid Acid Catalysts for the Esterification of Palmitic Acid. *Green Chem.* **2006**, *8* (9), 790–797.
- (165) Tang, M.; Yang, T.; Zhang, Y. A Brief Review on α -Zirconium Phosphate Intercalation Compounds and Nano-Composites. *Sci. China Technol. Sci.* **2016**, *59* (3), 436–441.

- (166) Díaz, A.; González, M. L.; Pérez, R. J.; David, A.; Mukherjee, A.; Báez, A.; Clearfield, A.; Colón, J. L. Direct Intercalation of Cisplatin into Zirconium Phosphate Nanoplatelets for Potential Cancer Nanotherapy. *Nanoscale* **2013**, 5 (23), 11456–11463.
- (167) Santiago, M. B.; Declet-Flores, C.; Díaz, A.; Vélez, M. M.; Bosques, M. Z.; Sanakis, Y.; Colón, J. L. Layered Inorganic Materials as Redox Agents: Ferrocenium-Intercalated Zirconium Phosphate. *Langmuir* **2007**, 23 (14), 7810–7817.
- (168) Kijima, T. Direct Preparation of θ -Zirconium Phosphate. *Bull. Chem. Soc. Jpn.* **1982**, 55 (9), 3031–3032.
- (169) Zhou, Y.; Huang, R.; Ding, F.; Brittain, A. D.; Liu, J.; Zhang, M.; Xiao, M.; Meng, Y.; Sun, L. Sulfonic Acid-Functionalized α -Zirconium Phosphate Single-Layer Nanosheets as a Strong Solid Acid for Heterogeneous Catalysis Applications. *ACS Appl. Mater. Interfaces* **2014**, 6 (10), 7417–7425.
- (170) Chen, X.; Wang, D.; Wang, Z.; Zhou, P.; Wu, Z.; Jiang, F. Molybdenum Phosphide: A New Highly Efficient Catalyst for the Electrochemical Hydrogen Evolution Reaction. *Chem. Commun.* **2014**, 50 (79), 11683–11685.
- (171) Bayati, M. Secondary Impact of Manganese on Catalytic Property of N-Doped Graphene in the Hydrogen Evolution Reaction. *Chemcatchem* **2017**, 9.
- (172) Wu, Y.; Zarei-Chaleshtori, M.; Torres, B.; Akter, T.; Diaz-Moreno, C.; Saupe, G. B.; Lopez, J. A.; Chianelli, R. R.; Villagrán, D. Electrocatalytic Hydrogen Gas Generation by Cobalt Molybdenum Disulfide (CoMoS₂) Synthesized Using Alkyl-Containing Thiomolybdate Precursors. *Int. J. Hydrog. Energy* **2017**, 42 (32), 20669–20676.
- (173) Matson, B. D.; Peters, J. C. Fe-Mediated HER vs N₂RR: Exploring Factors That Contribute to Selectivity in P₃Fe(N₂) (E = B, Si, C) Catalyst Model Systems. *ACS Catal.* **2018**, 8 (2), 1448–1455.
- (174) Kaeffer, N.; Chavarot-Kerlidou, M.; Artero, V. Hydrogen Evolution Catalyzed by Cobalt Diimine–Dioxime Complexes. *Acc. Chem. Res.* **2015**, 48 (5), 1286–1295.

- (175) Chen, L.; Khadivi, A.; Singh, M.; Jurss, J. W. Synthesis of a Pentadentate, Polypyrazine Ligand and Its Application in Cobalt-Catalyzed Hydrogen Production. *Inorg. Chem. Front.* **2017**, *4* (10), 1649–1653.
- (176) Elkin, T.; Kulkarni, N. V.; Tumanskii, B.; Botoshansky, M.; Shimon, L. J. W.; Eisen, M. S. Synthesis and Structure of Group 4 Symmetric Amidinate Complexes and Their Reactivity in the Polymerization of α -Olefins. *Organometallics* **2013**, *32* (21), 6337–6352.
- (177) Evans, D. F. 400. The Determination of the Paramagnetic Susceptibility of Substances in Solution by Nuclear Magnetic Resonance. *J. Chem. Soc. Resumed* **1959**, *0* (0), 2003–2005.
- (178) Ostfeld, D.; Cohen, I. A. A Cautionary Note on the Use of the Evans Method for Magnetic Moments. *J. Chem. Educ.* **1972**, *49* (12), 829.
- (179) Yang, L.; Powell, D. R.; Houser, R. P. Structural Variation in Copper(I) Complexes with Pyridylmethylamide Ligands: Structural Analysis with a New Four-Coordinate Geometry Index, Tau4. *Dalton Trans. Camb. Engl. 2003* **2007**, No. 9, 955–964.
- (180) Fryzuk, M. D.; Leznoff, D. B.; Thompson, R. C.; Rettig, S. J. One-Electron Transformations of Paramagnetic Cobalt Complexes. Synthesis and Structure of Cobalt(II) Amidodiphosphine Halide and Alkyl Complexes and Their Reaction with Alkyl Halides. *J. Am. Chem. Soc.* **1998**, *120* (39), 10126–10135.
- (181) Fink, K.; Wang, C.; Staemmler, V. Superexchange and Spin–Orbit Coupling in Chlorine-Bridged Binuclear Cobalt(II) Complexes. *Inorg. Chem.* **1999**, *38* (17), 3847–3856.
- (182) Gerloch, M.; Quested, P. N. Magnetic Properties of Cobalt(II) Complexes. Part I. Trigonal Distorted Octahedral Geometries. *J. Chem. Soc. Inorg. Phys. Theor.* **1971**, *0* (0), 3729–3741.
- (183) Staszak-Jirkovský, J.; Malliakas, C. D.; Lopes, P. P.; Danilovic, N.; Kota, S. S.; Chang, K.-C.; Genorio, B.; Strmcnik, D.; Stamenkovic, V. R.; Kanatzidis, M. G.; et al. Design of Active and Stable Co-Mo-Sx Chalcogels as PH-Universal Catalysts for the Hydrogen Evolution Reaction. *Nat. Mater.* **2016**, *15* (2), 197–203.

- (184) Füchtbauer, H. G.; Tuxen, A. K.; Li, Z.; Topsøe, H.; Lauritsen, J. V.; Besenbacher, F. Morphology and Atomic-Scale Structure of MoS₂ Nanoclusters Synthesized with Different Sulfiding Agents. *Top. Catal.* **2014**, *57* (1), 207–214.
- (185) Bag, S.; Gaudette, A. F.; Bussell, M. E.; Kanatzidis, M. G. Spongy Chalcogels of Non-Platinum Metals Act as Effective Hydrodesulfurization Catalysts. *Nat. Chem.* **2009**, *1* (3), 217–224.
- (186) Prins, R.; Beer, V. H. J. D.; Somorjai, G. A. Structure and Function of the Catalyst and the Promoter in Co—Mo Hydrodesulfurization Catalysts. *Catal. Rev.* **1989**, *31* (1–2), 1–41.
- (187) Karunadasa, H. I.; Montalvo, E.; Sun, Y.; Majda, M.; Long, J. R.; Chang, C. J. A Molecular MoS₂ Edge Site Mimic for Catalytic Hydrogen Generation. *Science* **2012**, *335* (6069), 698–702.
- (188) Laursen, A. B.; Kegnæs, S.; Dahl, S.; Chorkendorff, I. Molybdenum Sulfides—Efficient and Viable Materials for Electro - and Photoelectrocatalytic Hydrogen Evolution. *Energy Environ. Sci.* **2012**, *5* (2), 5577–5591.
- (189) Hu, W.-H.; Shang, X.; Xue, J.; Dong, B.; Chi, J.-Q.; Han, G.-Q.; Liu, Y.-R.; Li, X.; Yan, K.-L.; Chai, Y.-M.; et al. Activating MoS₂/CNs by Tuning (001) Plane as Efficient Electrocatalysts for Hydrogen Evolution Reaction. *Int. J. Hydrog. Energy* **2017**, *42* (4), 2088–2095.
- (190) Shang, X.; Hu, W.-H.; Li, X.; Dong, B.; Liu, Y.-R.; Han, G.-Q.; Chai, Y.-M.; Liu, C.-G. Oriented Stacking along Vertical (002) Planes of MoS₂: A Novel Assembling Style to Enhance Activity for Hydrogen Evolution. *Electrochimica Acta* **2017**, *224*, 25–31.
- (191) Tran, P. D.; Tran, T. V.; Orio, M.; Torelli, S.; Truong, Q. D.; Nayuki, K.; Sasaki, Y.; Chiam, S. Y.; Yi, R.; Honma, I.; et al. Coordination Polymer Structure and Revisited Hydrogen Evolution Catalytic Mechanism for Amorphous Molybdenum Sulfide. *Nat. Mater.* **2016**, *15* (6), 640–646.

- (192) Lukowski, M. A.; Daniel, A. S.; Meng, F.; Forticaux, A.; Li, L.; Jin, S. Enhanced Hydrogen Evolution Catalysis from Chemically Exfoliated Metallic MoS₂ Nanosheets. *J. Am. Chem. Soc.* **2013**, *135* (28), 10274–10277.
- (193) Popczun Eric J.; Read Carlos G.; Roske Christopher W.; Lewis Nathan S.; Schaak Raymond E. Highly Active Electrocatalysis of the Hydrogen Evolution Reaction by Cobalt Phosphide Nanoparticles. *Angew. Chem. Int. Ed.* **2014**, *53* (21), 5427–5430.
- (194) Nava, H.; Ornelas, C.; Aguilar, A.; Berhault, G.; Fuentes, S.; Alonso, G. Cobalt-Molybdenum Sulfide Catalysts Prepared by In Situ Activation of Bimetallic (Co-Mo) Alkylthiomolybdates. *Catal. Lett.* **2003**, *86* (4), 257–265.
- (195) Liu, Y.-R.; Shang, X.; Gao, W.-K.; Dong, B.; Li, X.; Li, X.-H.; Zhao, J.-C.; Chai, Y.-M.; Liu, Y.-Q.; Liu, C.-G. In Situ Sulfurized CoMoS/CoMoO₄ Shell–Core Nanorods Supported on N-Doped Reduced Graphene Oxide (NRGO) as Efficient Electrocatalyst for Hydrogen Evolution Reaction. *J. Mater. Chem. A* **2017**, *5* (6), 2885–2896.
- (196) Dai, X.; Du, K.; Li, Z.; Liu, M.; Ma, Y.; Sun, H.; Zhang, X.; Yang, Y. Co-Doped MoS₂ Nanosheets with the Dominant CoMoS Phase Coated on Carbon as an Excellent Electrocatalyst for Hydrogen Evolution. *ACS Appl. Mater. Interfaces* **2015**, *7* (49), 27242–27253.
- (197) Alvarez, L.; Espino, J.; Ornelas, C.; Rico, J. L.; Cortez, M. T.; Berhault, G.; Alonso, G. Comparative Study of MoS₂ and Co/MoS₂ Catalysts Prepared by Ex Situ/in Situ Activation of Ammonium and Tetraalkylammonium Thiomolybdates. *J. Mol. Catal. Chem.* **2004**, *210* (1), 105–117.
- (198) Alonso, G.; Del Valle, M.; Cruz, J.; Petranovskii, V.; Licea-Claverie, A.; Fuentes, S. Preparation of MoS₂ Catalysts by in Situ Decomposition of Tetraalkylammonium Thiomolybdates. *Catal. Today* **1998**, *43* (1), 117–122.
- (199) Chianelli, R. R.; Berhault, G. Symmetrical Synergism and the Role of Carbon in Transition Metal Sulfide Catalytic Materials. *Catal. Today* **1999**, *53* (3), 357–366.

- (200) Alonso, G.; Petranovskii, V.; Del Valle, M.; Cruz-Reyes, J.; Licea-Claverie, A.; Fuentes, S. Preparation of WS₂ Catalysts by in Situ Decomposition of Tetraalkylammonium Thiotungstates. *Appl. Catal. Gen.* **2000**, *197* (1), 87–97.
- (201) Alonso, G.; Berhault, G.; Aguilar, A.; Collins, V.; Ornelas, C.; Fuentes, S.; Chianelli, R. R. Characterization and HDS Activity of Mesoporous MoS₂ Catalysts Prepared by in Situ Activation of Tetraalkylammonium Thiomolybdates. *J. Catal.* **2002**, *208* (2), 359–369.
- (202) McEnaney, J. M.; Crompton, J. C.; Callejas, J. F.; Popczun, E. J.; Read, C. G.; Lewis, N. S.; Schaak, R. E. Electrocatalytic Hydrogen Evolution Using Amorphous Tungsten Phosphide Nanoparticles. *Chem. Commun. Camb. Engl.* **2014**, *50* (75), 11026–11028.
- (203) Alonso, G.; Yang, J.; Siadati, M. H.; Chianelli, R. R. Synthesis of Tetraalkylammonium Thiometallates in Aqueous Solution. *Inorganica Chim. Acta* **2001**, *325* (1), 193–197.
- (204) Ramos, M.; Berhault, G.; Ferrer, D. A.; Torres, B.; Chianelli, R. R. HRTEM and Molecular Modeling of the MoS₂–Co₉S₈ Interface: Understanding the Promotion Effect in Bulk HDS Catalysts. *Catal. Sci. Technol.* **2011**, *2* (1), 164–178.
- (205) Romero-Rivera, R.; Del Valle, M.; Alonso, G.; Flores, E.; Castellón, F.; Fuentes, S.; Cruz-Reyes, J. Cyclohexene Hydrogenation with Molybdenum Disulfide Catalysts Prepared by Ex Situ Decomposition of Ammonium Thiomolybdate-Cetyltrimethylammonium Thiomolybdate Mixtures. *Catal. Today* **2008**, *130* (2), 354–360.
- (206) Iranmahboob, J.; Hill, D. O.; Toghiani, H. Characterization of K₂CO₃/Co-MoS₂ Catalyst by XRD, XPS, SEM, and EDS. *Appl. Surf. Sci.* **2001**, *185* (1–2), 72–78.
- (207) Conway, B. E.; Tilak, B. V. Interfacial Processes Involving Electrocatalytic Evolution and Oxidation of H₂, and the Role of Chemisorbed H. *Electrochimica Acta* **2002**, *47* (22), 3571–3594.

Appendix

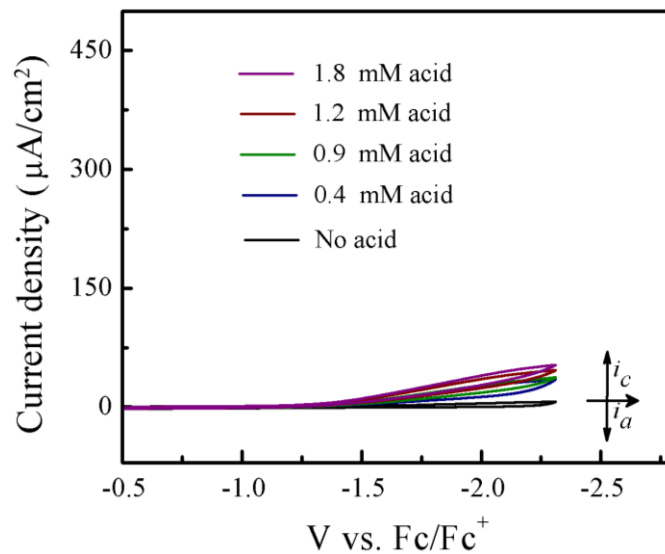


Figure A.1. Cyclic voltammograms of tosic acid in THF (no catalyst added); Scan rate: 100 mV/s; glassy carbon working electrode.

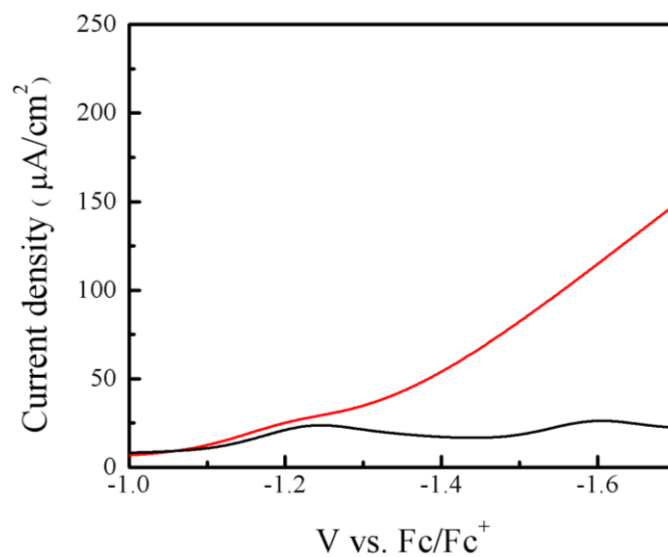


Figure A.2. Linear sweep voltammograms of 0.1 mM **1** (black) and **1** with 12 equivalent deuterated tosic acid (red).

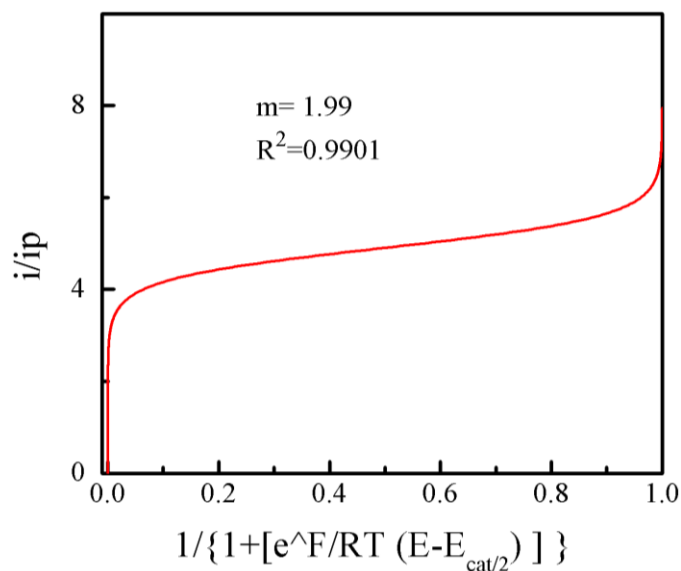


Figure A.3. FOWA linear fit of **1** for hydrogen generation using 1.2 mM deuterated *tosic* acid.

Kinetic isotope effect (KIE) was analyzed using deuterated *tosic* acid ($\text{C}_7\text{H}_7\text{SO}_3\text{D}$). The calculated k_{cat} using $\text{C}_7\text{H}_7\text{SO}_3\text{H}$ is $742.5 \text{ M}^{-1}\text{s}^{-1}$ while k_{cat} using $\text{C}_7\text{H}_7\text{SO}_3\text{D}$ is $640.0 \text{ M}^{-1}\text{s}^{-1}$, resulting in $\text{KIE} = k_{\text{cat}, \text{C}_7\text{H}_7\text{SO}_3\text{H}}/k_{\text{cat}, \text{C}_7\text{H}_7\text{SO}_3\text{D}} = 1.16$.

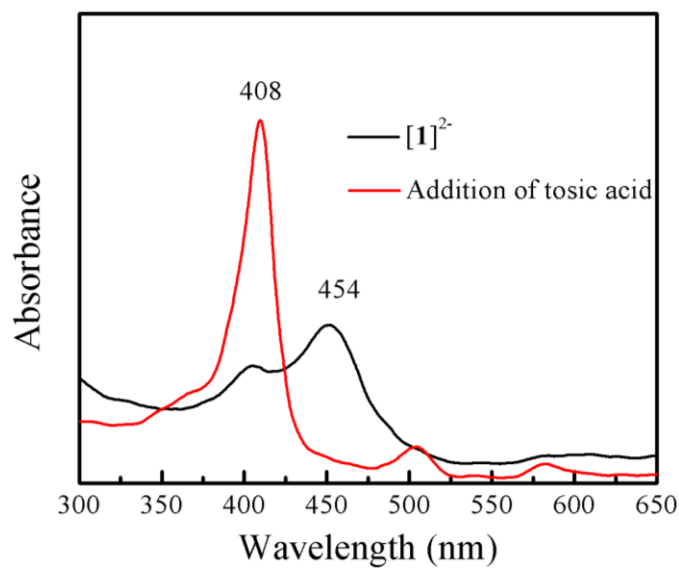


Figure A.4. UV-vis spectrum of $[\mathbf{1}]^{2-}$ (black) and the spectrum recorded upon addition of *tosic* acid to $[\mathbf{1}]^{2-}$ (red).

Uv-vis spectroelectrochemical study was performed using **1** at a potential of -1.7 V vs. Fc/Fc^+ to obtain the dianion species, $[\mathbf{1}]^{2-}$ (black line in Figure A.4). Subsequently, tosic acid was added to the solution and **1** was spontaneously obtained according to the spectrum (red line in Figure A.4). This implies catalysis occurred upon addition of acid and **1** was regenerated. It should be noted that *E-E-P-P* pathway is also feasible for the generation of hydrogen gas.

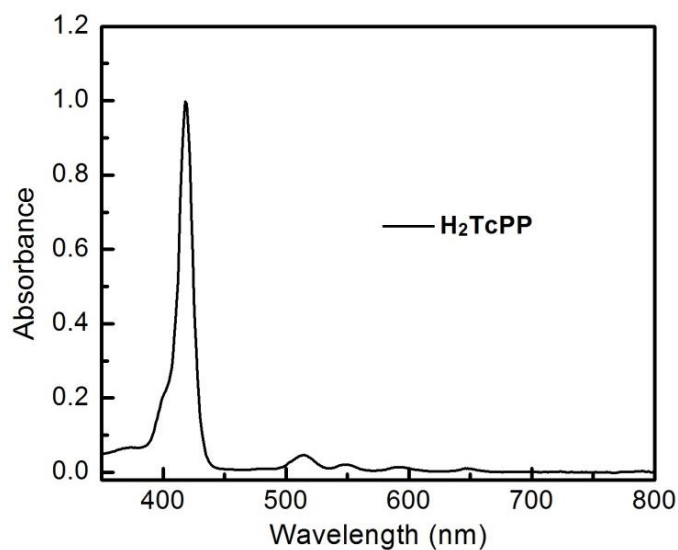


Figure A.5. UV-vis spectrum of H₂TcPP in EtOH.

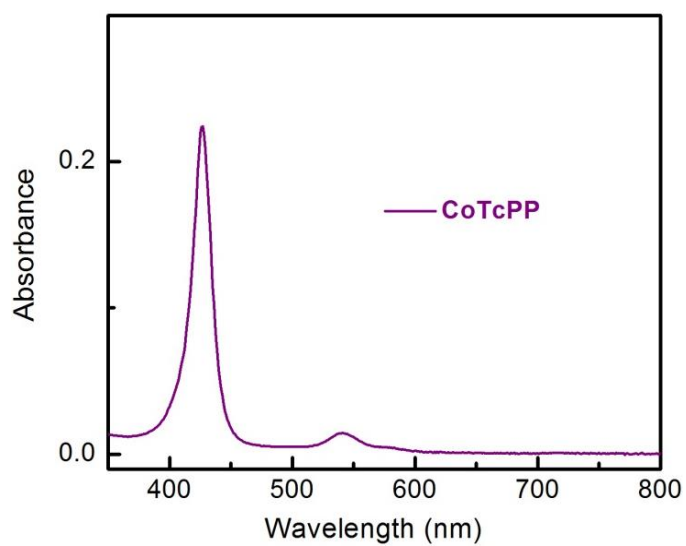


Figure A.6. UV-vis spectrum of **3** in EtOH.

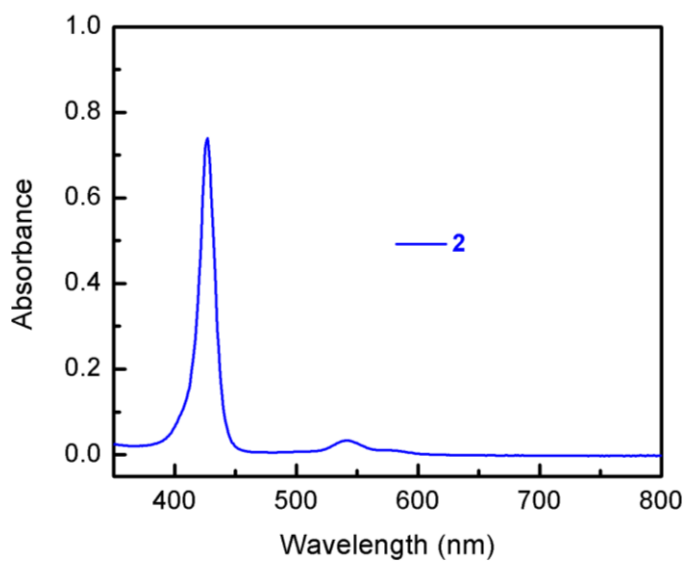


Figure A.7. UV-vis spectrum of **2** dissolved in pH = 8 phosphate buffer solution.

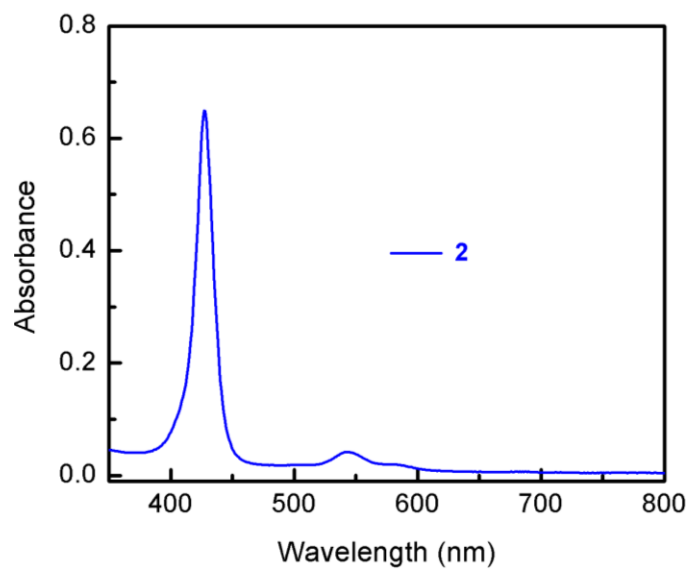


Figure A.8. UV-vis spectrum of **2** dissolved in pH = 14 KOH aqueous solution. Precipitation of $\text{Co}(\text{OH})_2$ was observed.

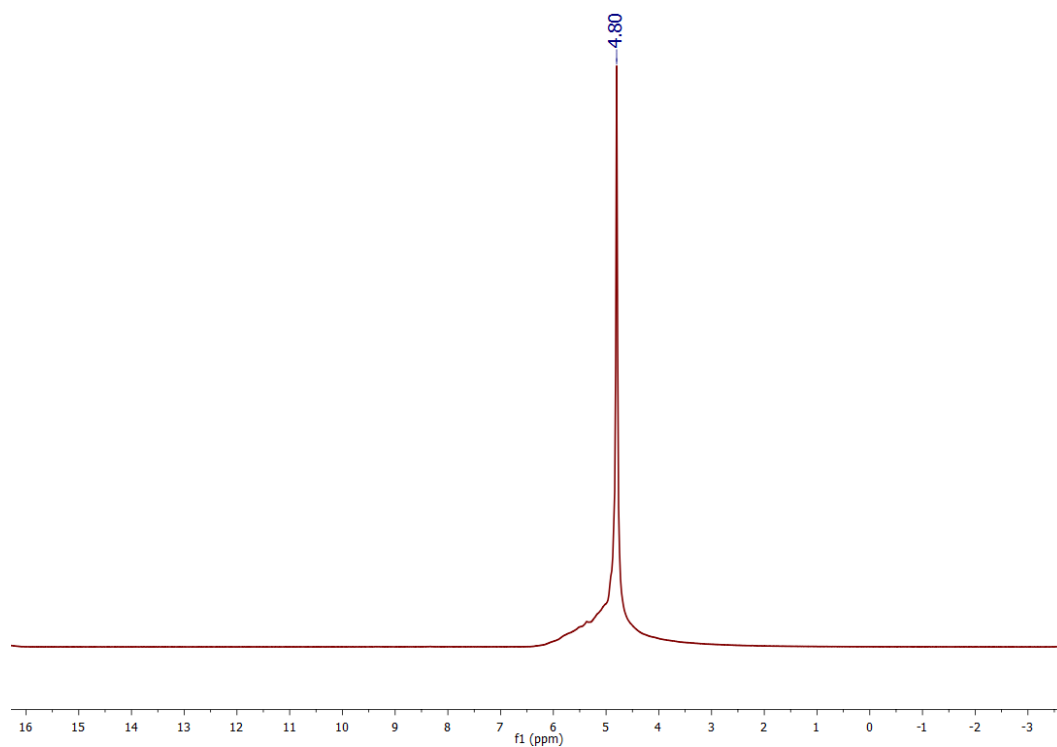


Figure A.9. ^1H NMR spectrum of **2** dissolved in pH = 8 phosphate buffer deuterium oxide solution. The spectrum shows broad signals besides the solvent peak, resulting from the $\text{d}^7 \text{Co}^{2+}$ center.

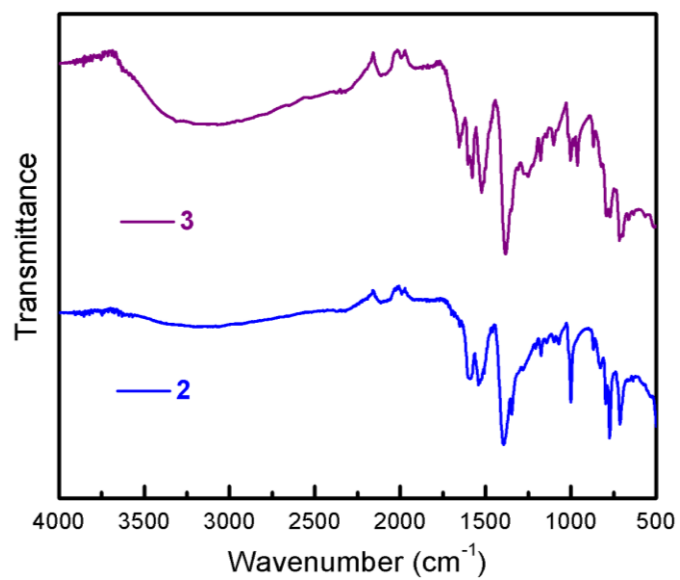


Figure A.10. Infrared spectra of **2** and **3**.

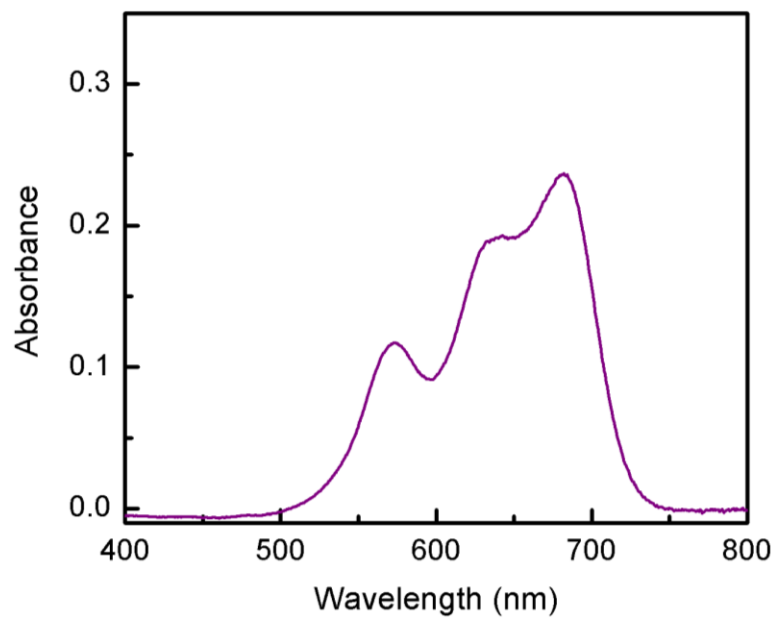


Figure A.11. Uv-vis spectrum of **4**.

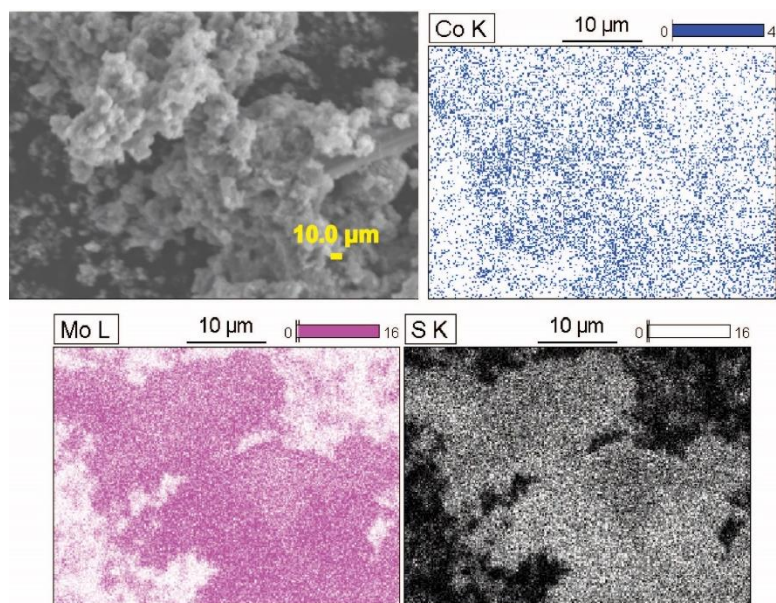


Figure A.12. SEM and the corresponding elemental mapping images of 6.

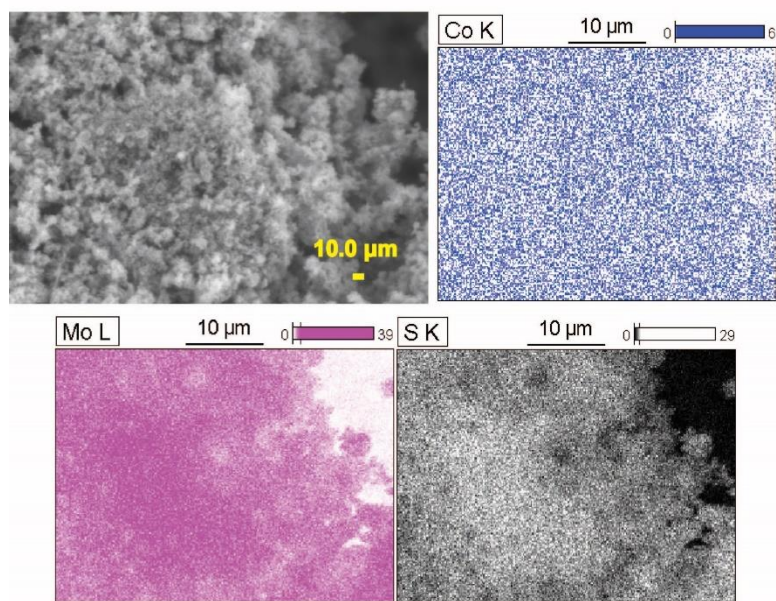


Figure A.13. SEM and the corresponding elemental mapping images of 7.

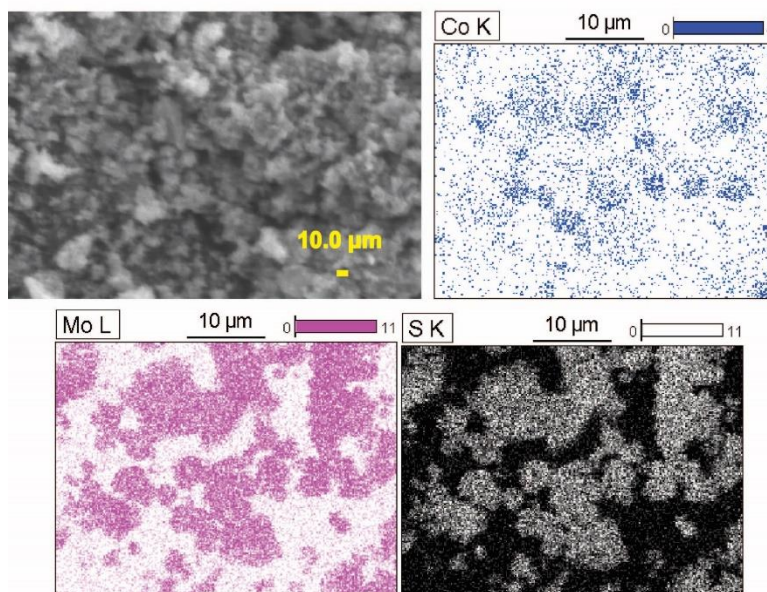


Figure A.14. SEM and the corresponding elemental mapping images of **8**.

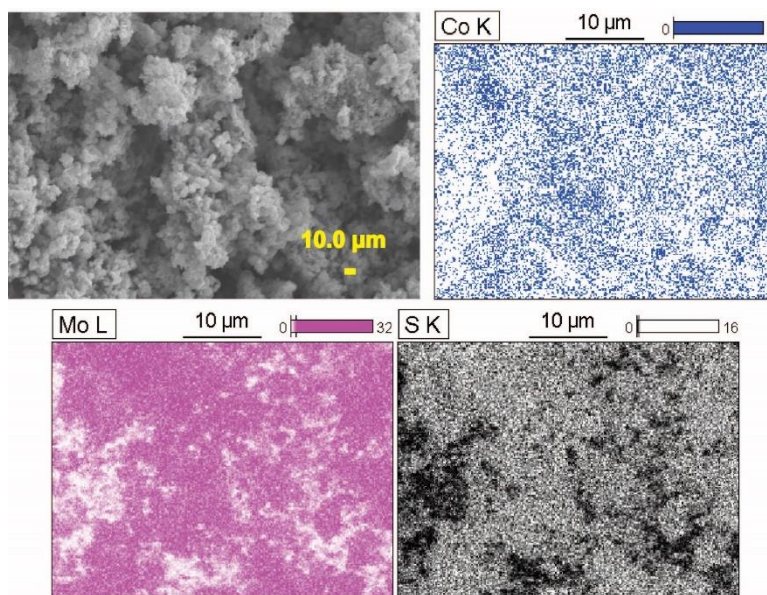


Figure A.15. SEM and the corresponding elemental mapping images of **5** after 10 h's electrocatalysis in 0.5 M H₂SO₄ at -0.2 V vs. RHE.

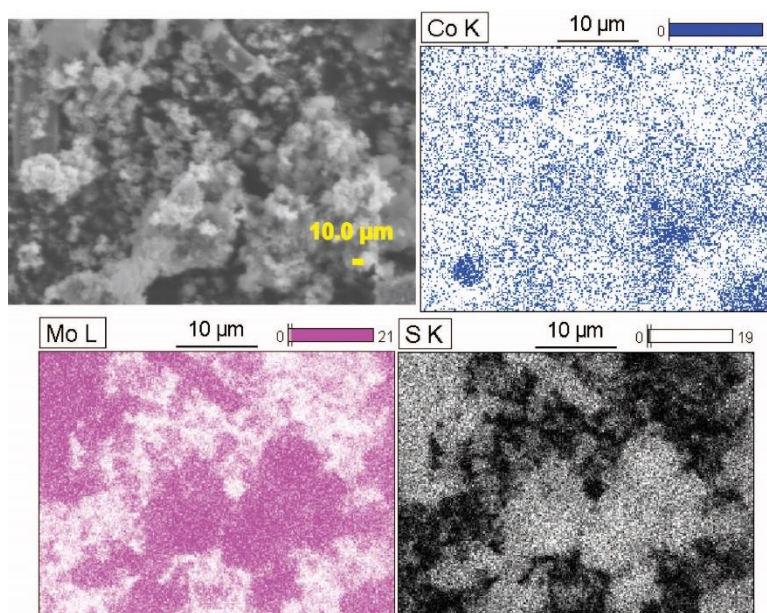


Figure A.16. SEM and the corresponding elemental mapping images of **6** after 10 h' electrocatalysis in 0.5 M H₂SO₄ at –0.2 V vs. RHE.

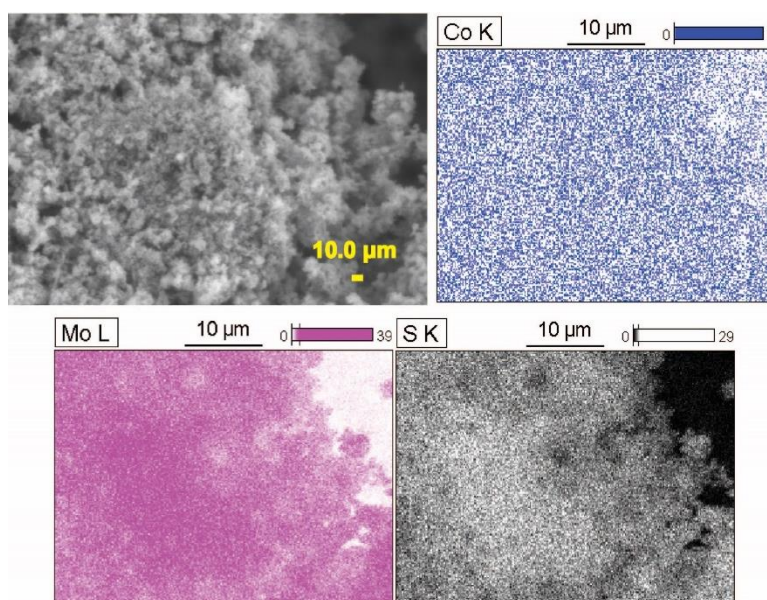


Figure A.17. SEM and the corresponding elemental mapping images of **7** after 10 h' electrocatalysis in 0.5 M H₂SO₄ at –0.2 V vs. RHE.

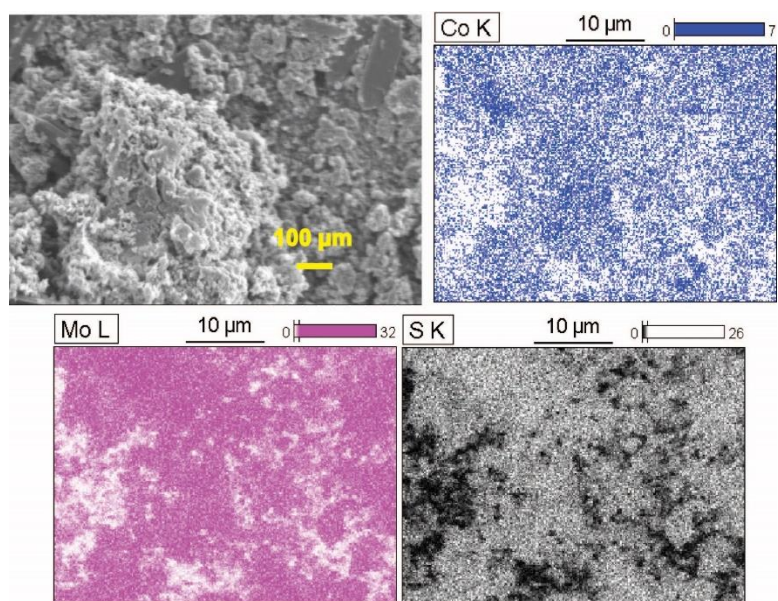


Figure A.18. SEM and the corresponding elemental mapping images of **8** after 10 h' electrocatalysis in 0.5 M H₂SO₄ at -0.2 V vs. RHE.

Vita

Yanyu Wu was born and raised in Zhaoqing, a city of Guangdong province in China. She went to Shantou University to pursue her bachelor degree with a major in Applied Chemistry in 2009 and obtained her degree in 2013. In 2012, Yanyu was offered the opportunity to visit the University of Texas at El Paso (UTEP) for an undergraduate summer research program, where she spent two months studied and researched bulk heterojunction organic solar cells. In September, 2013, Yanyu came back to UTEP to pursue her doctoral degree with a major in Chemistry.

Permanent address: 2800 Wooden Tower st
Pflugerville, TX, 78660

This dissertation was typed by Yanyu Wu.